

COVALENT AND NON-COVALENT FUNCTIONALIZATION OF GRAPHENE
FOR APPLICATION IN CATALYSIS AND DEVICE TECHNOLOGY: A FIRST
PRINCIPLES COMPUTATIONAL STUDY

A THESIS SUBMITTED TO
THE GRADUATE SCHOOL OF NATURAL AND APPLIED SCIENCES
OF
MIDDLE EAST TECHNICAL UNIVERSITY

TUĞÇE İRFAN AKAY

IN PARTIAL FULFILLMENT OF THE REQUIREMENTS
FOR
THE DEGREE OF DOCTOR OF PHILOSOPHY
IN
MICRO AND NANOTECHNOLOGY

JUNE 2017

Approval of the thesis:

**COVALENT AND NON-COVALENT FUNCTIONALIZATION OF GRAPHENE
FOR APPLICATION IN CATALYSIS AND DEVICE TECHNOLOGY: A FIRST
PRINCIPLES COMPUTATIONAL STUDY**

submitted by **TUĞÇE İRFAN AKAY** in partial fulfillment of the requirements for
the degree of **Doctor of Philosophy in Micro and Nanotechnology Department,**
Middle East Technical University by,

Prof. Dr. Gülbin DURAL ÜNVER _____
Dean, Graduate School of **Natural and Applied Sciences**

Assoc. Prof. Dr. Burcu AKATA KURÇ _____
Head of Department, **Micro and Nanotechnology**

Assoc. Prof. Dr. Hande TOFFOLI _____
Supervisor, **Physics Department, METU**

Assoc. Prof. Dr. Burcu AKATA KURÇ _____
Co-supervisor, **Micro and Nanotechnology Department,**
METU

Examining Committee Members:

Prof. Dr. Oğuz GÜLSEREN _____
Physics Department, İhsan Doğramacı Bilkent University

Assoc. Prof. Dr. Hande TOFFOLI _____
Physics Department, METU

Prof. Dr. Gürkan KARAKAŞ _____
Chemical Engineering Department, METU

Prof. Dr. Mehmet PARLAK _____
Physics Department, METU

Prof. Dr. Mehmet ÇAKMAK _____
Physics Department, Gazi University

Date: _____

I hereby declare that all information in this document has been obtained and presented in accordance with academic rules and ethical conduct. I also declare that, as required by these rules and conduct, I have fully cited and referenced all material and results that are not original to this work.

Name, Last Name: TUĞÇE İRFAN AKAY

Signature :

ABSTRACT

COVALENT AND NON-COVALENT FUNCTIONALIZATION OF GRAPHENE FOR APPLICATION IN CATALYSIS AND DEVICE TECHNOLOGY: A FIRST PRINCIPLES COMPUTATIONAL STUDY

AKAY, TUĞÇE İRFAN

Ph.D., Department of Micro and Nanotechnology

Supervisor : Assoc. Prof. Dr. Hande TOFFOLI

Co-Supervisor : Assoc. Prof. Dr. Burcu AKATA KURÇ

June 2017, 135 pages

In the past few decades, nanomaterials have received increasing attention in various applications such as drug delivery, sensors, hydrogen storage and solar cells. This thesis focuses on the theoretical exploration of pristine and defective graphene in order to highlight the functionalization potential with the use of a wide variety of molecules such as benzene (C_6H_6), toluene (C_7H_8), fluorobenzene (C_6H_5F), benzonitrile (C_7H_5N), benzoic acid ($C_7H_6O_2$), and boron (B) atom. The structures as well as electronic properties of these graphene based nano structures are investigated in detail using first-principle calculations using planewave pseudopotential method based on density functional theory (DFT).

In order to understand the effect of different van der Waals (vdW) dispersion forces on structural and electronic properties, the adsorption of C_6H_6 and C_7H_8 on pristine and defective graphene are investigated with three different exchange-correlation functionals namely vdW-DF, vdW-DF2-C09 and Grimme-D2. This study reveals that

the vdW-DF2-C09 exchange-correlation protocol for the vdW interactions produces the closest agreement with literature. Furthermore, the adsorption of C_6H_6 and C_7H_8 is investigated on bilayer graphene to understand the effects of number of layers on adsorption characteristics. This study reveals that the presence of the second layer increases the adsorption energy by approximately 70 meV for both molecules.

Following the exploration of the interaction of pristine graphene and its derivatives with C_6H_6 and C_7H_8 , boron (B) is introduced in the graphene network with mono and divacancy defect to controllably engineer the electronic properties of graphene. A systematic study for the magnetization characteristics is demonstrated where the resulting magnetization of B-doped vacancy-defected graphene (BVG) is $0.9 \mu_B$ per cell while it is $0 \mu_B$ per cell for B-doped divacancy-defected graphene (BDG). For the electronic properties, we show the role of B concentration and position on charge transfer and band structure. The band gap opening increases with the increased concentration of B while graphene sheet becomes p-doped with B as a dopant.

Finally, we focus on organic adsorbates for additional control of the electronic properties of BVG. C_6H_6 , C_7H_8 , C_6H_5F , C_7H_5N , and $C_7H_6O_2$ are studied with different adsorption geometries. C_6H_5F and $C_7H_6O_2$ are found to adsorb through weak vdW interactions, C_7H_5N molecules are observed to form strong covalent bonds with the atoms surrounding the defect, and in particular the B atoms. Different bond formation characteristics are observed resulting in phenyl (C_6H_5) and benzaldehyde (C_7H_6O) formation. The charge transfer analysis indicate the fact that organic adsorbates donate electron resulting in positively charged species at the end of calculations.

Keywords: Graphene, Density Functional Theory, Benzene, Toluene, Boron, Fluorobenzene, Benzonitrile, Benzoic Acid

ÖZ

KATALİZ VE CİHAZ TEKNOLOJİSİ UYGULAMALARI İÇİN GRAFENİN KOVALENT VE KOVALENT OLMAYAN ŞEKİLDE İŞLEVSELLEŞTİRİLMESİ: İLK-İLKELER HESAPLAMA ÇALIŞMASI

AKAY, TUĞÇE İRFAN

Doktora, Mikro ve Nanoteknoloji Bölümü

Tez Yöneticisi : Doç. Dr. Hande TOFFOLI

Ortak Tez Yöneticisi : Doç. Dr. Burcu AKATA KURÇ

Haziran 2017 , 135 sayfa

Son birkaç on yılda, nanomalzemeler ilaç salınımı, sensörler, hidrojen depolama ve güneş pilleri gibi çeşitli uygulamalarda artan bir ilgi görmektedir. Bu tez, benzen (C_6H_6), toluen (C_7H_8), florobenzen (C_6H_5F), benzonitril (C_7H_5N), benzoik asit ($C_7H_6O_2$), ve boron (B) atomu gibi çok çeşitli moleküllerin kullanımı ile işlevselleştirme potansiyelini vurgulamak için bozulmamış ve kusurlu grafenin teorik araştırılması üzerine odaklanmaktadır. Grafene dayalı nano yapıların yapıları ve elektronik özellikleri, yoğunluk fonksiyonel teorisine (YFT) dayalı düzlem dalga sanki potansiyel metodu kullanılarak ilk-ilkeler hesaplamaları kullanılarak detaylı olarak incelenmiştir.

Farklı van der Waals (vdW) dağılma kuvvetlerinin yapısal ve elektronik özelliklere etkisini anlamak için, C_6H_6 ve C_7H_8 'in bozulmamış ve kusurlu grafene adsorpsiyonu vdW-DF, vdW-DF2-C09 ve Grimme-D2 olmak üzere üç farklı değişim-korelasyon

fonksiyonu ile araştırılmıştır. Bu çalışma, vdW etkileşimleri için vdW-DF2-C09 deęişim-korelasyon protokolünün literatür ile en yakın sonucu ürettiğini ortaya koymaktadır. Ayrıca, tabaka sayılarının adsorpsiyon karakteristiğine etkilerini anlamak için iki katmanlı grafen üzerinde C_6H_6 ve C_7H_8 'lerin adsorpsiyonu araştırılmıştır. Bu çalışma, ikinci katmanın varlığının, adsorpsiyon enerjisini her iki molekül için de yaklaşık olarak 70 meV arttırdığını ortaya koymaktadır.

Bozulmamış grafen ve türevlerinin, C_6H_6 ve C_7H_8 ile etkileşiminin araştırılmasını takiben, grafenin elektronik özelliklerini kontrol edebilmek için grafen ağına, tek ve çift boşluk kusuru ile birlikte boron (B) verilir. B-katkılı ve tek boşluk kusurlu grafenin (BVG) sonuçlanan manyetizasyonunun hücre başına $0.9 \mu_B$ iken B-katkılı çift boşluk kusurlu grafen (BDG) için bu deęerin hücre başına $0 \mu_B$ olarak hesaplandığı manyetizasyon özellikleri için sistematik bir çalışma gösterilmiştir. Elektronik özellikler için, B konsantrasyonunun ve konumunun yük aktarımı ve bant yapısı üzerindeki etkilerini gösteriyoruz. Bant aralığı, artmış B konsantrasyonuyla birlikte artarken, grafen p-katkılı hale gelir.

Son olarak, BVG'nin elektronik özelliklerinin daha ileri kontrolü için organik adsorbantlara odaklanılmıştır. C_6H_6 , C_7H_8 , C_6H_5F , C_7H_5N , ve $C_7H_6O_2$ farklı adsorpsiyon geometrileri ile incelenmiştir. C_6H_5F ve $C_7H_6O_2$ 'lerin zayıf vdW etkileşimleri vasıtasıyla adsorbe edildiği, C_7H_5N moleküllerinin ise kusuru çevreleyen atomlar ve özellikle B atomları ile kuvvetli kovalent bağlar oluşturduğu gözlenmiştir. Fenil (C_6H_5) ve benzaldehit (C_7H_6O) oluşumuna neden olan farklı bağ oluşum özellikleri gözlemlenmiştir. Yük transferi analizi, hesaplamaların sonunda pozitif yüklü türler oluşturan organik adsorbatların elektron baęışısı yaptığını göstermektedir.

Anahtar Kelimeler: Grafen, Yoęunluk Fonksiyoneli Teorisi, Benzen, Toluen, Boron, Florobenzen, Benzonitril, Benzoik Asit

To my family

ACKNOWLEDGMENTS

First and foremost, I would like to take this opportunity to express my sincerest gratitude and appreciation to my main supervisor Assoc. Prof. Hande Toffoli for her invaluable guidance, supervision, and advice for my Ph.D. study. Besides, I would like to express my sincere appreciation to my former supervisor Assoc. Prof. Daniele Toffoli. I appreciated their guidance, encouragement and the helpful discussions we had. The work presented here would certainly not have been accomplished without their influence and support.

I would like to thank my co-supervisor Assoc. Prof. Burcu Akata Kurç for her guidance throughout the study.

I would like to extend my gratitudes to thesis examining committee members, Prof. Oğuz Gülseren and Prof. Gürkan Karakaş for their very helpful comments and precious suggestions to improve my dissertation in various ways.

I would like to thank Mustafa Ay, my supervisor at TUBITAK-KAMAG Unit, who gave me opportunity to continue my academic career while still working and always supported me in this long path.

I wish to thank our group members at Physics Department in addition to my colleagues. It would have been not possible for me to finish my doctoral dissertation without the help and support of the people around me and the excellent research environment provided by Middle East Technical University.

Last but certainly not least, I would like to express my deepest gratitude to my family for their love, support, encouragement and patience throughout my life.

TABLE OF CONTENTS

ABSTRACT	v
ÖZ	vii
ACKNOWLEDGMENTS	x
TABLE OF CONTENTS	xi
LIST OF TABLES	xiv
LIST OF FIGURES	xvi
LIST OF ABBREVIATIONS	xxv
CHAPTERS	
1 INTRODUCTION	1
1.1 Graphene	2
1.2 Applications Involving Graphene-Based Materials	4
1.3 Research Objective and Scope	9
1.4 Organization of This Dissertation	10
2 THEORETICAL BACKGROUND	13
2.1 Density Functional Theory	14
2.1.1 The Schrödinger Equation	14

2.1.2	Hohenberg-Kohn Theorem	15
2.1.3	The Kohn-Sham Method	16
2.1.4	Exchange-Correlation Functionals	18
2.1.5	Van der Waals Interactions	19
2.1.6	Pseudopotentials	22
2.2	Mechanism of a Density Functional Theory Calculation . . .	24
2.2.1	Self-Consistency Cycle	24
2.2.2	Structure Optimization	25
2.2.3	Computational Details	25
2.3	Preliminary Calculations	27
2.3.1	Lattice Constant Optimization Calculations	27
2.3.2	Pristine and Defective Graphene Calculations . . .	28
3	ORGANIC MOLECULES ON PRISTINE AND DEFECTIVE GRAPHENE	31
3.1	Previous Work	31
3.2	Organic Molecules on Single Layer Graphene	33
3.2.1	Organic Molecules on Pristine Graphene	35
3.2.1.1	Unoccupied States in PDOS Plots	41
3.2.2	Organic Molecules on Vacancy-Defected Graphene	42
3.2.3	Organic Molecules on Divacancy-Defected Graphene	48
3.3	Organic Molecules on Bilayer Graphene	54
4	BORON DOPING TO DEFECTIVE GRAPHENE	67

4.1	Previous Work	67
4.2	Magnetization of Boron Doped Defective Graphene	69
4.2.1	Magnetization of Boron Doped Vacancy-Defected Graphene	69
4.2.2	Magnetization of Boron Doped Divacancy-Defected Graphene	70
4.3	Electronic Properties of Boron Doped Defective Graphene	72
4.3.1	Boron Doped Vacancy-Defected Graphene	73
4.3.2	Boron Doped Divacancy-Defected Graphene	76
5	GRAPHENE FUNCTIONALIZATION WITH BENZENE DERIVATIVES	83
5.1	Previous Work	83
5.2	Molecules	84
5.3	Molecular Doping to B Doped Defective Graphene	85
5.3.1	Fluorine Containing Benzene Derivative	90
5.3.2	Nitrogen Containing Benzene Derivative	94
5.3.3	Oxygen Containing Benzene Derivative	97
6	CONCLUSION	105
	REFERENCES	109
	CURRICULUM VITAE	133

LIST OF TABLES

TABLES

Table 2.1	The lattice constant optimization for graphene.	27
Table 3.1	The adsorption energies and distances of C ₆ H ₆ and C ₇ H ₈ on PG at different sites.	38
Table 3.2	The adsorption energies of C ₆ H ₆ and C ₇ H ₈ on VG at different sites.	45
Table 3.3	The adsorption energies of C ₆ H ₆ and C ₇ H ₈ on DG at different sites.	51
Table 3.4	The adsorption energies for C ₆ H ₆ C ₇ H ₈ on single layer and bilayer graphene.	65
Table 3.5	The adsorption distances, energies and charge transfer values of C ₆ H ₆ and C ₇ H ₈ on single layer and bilayer graphene. (vdW-DF2-C09 employed calculations are displayed).	66
Table 4.1	The displacement of B atoms and total magnetization (μ_B per cell) of optimized BVG. The configurations of BVG are displayed in Figure 4.5 and 4.6.	75
Table 4.2	The displacement of B atoms and total magnetization (μ_B per cell) of optimized BDG. The configurations of BDG are displayed in Figure 4.9 and 4.10.	79
Table 5.1	Isotropic polarizabilities (α), and dipole moments (μ) of the gas phase molecules.	85

Table 5.2 Adsorption distances, energies, magnetization (μ_B per cell) and charge transfer values of C_6H_5F on BVG.	92
Table 5.3 Adsorption distances, energies and magnetization (μ_B per cell) of C_7H_5N on BVG.	96
Table 5.4 Adsorption distances, energies, magnetization (μ_B per cell) and charge transfer values of $C_7H_6O_2$ on BVG.	100

LIST OF FIGURES

FIGURES

Figure 1.1	The unit cell and the BZ of graphene.	3
Figure 1.2	The electron dispersion relation of graphene (a) when the Fermi level is above the Dirac point, (b) when the Fermi level is below the Dirac point.	4
Figure 1.3	The organization of thesis.	11
Figure 2.1	Classification of functionals as “stairway to heaven”.	20
Figure 2.2	The real and pseudo potentials and wave functions.	23
Figure 2.3	Kohn-Sham self-consistency cycle.	24
Figure 2.4	Optimized structures, band structures, DOS and charge density plots of pristine graphene (a), spin-unpolarized VG (b), spin-polarized VG (c), and DG (d).	29
Figure 3.1	Configuration of C ₆ H ₆ on single layer graphene for adsorption height calculations.	34
Figure 3.2	The adsorption energy curve of C ₆ H ₆ on single layer graphene with vdW-DF (a), vdW-DF2-C09 (b), and Grimme-D2 (c).	35
Figure 3.3	Different initial configurations for C ₆ H ₆ on PG for parallel (a), and perpendicular adsorption (b).	36

Figure 3.4 Different initial configurations for C_7H_8 on PG for parallel (a), and perpendicular adsorption (b).	36
Figure 3.5 The top view, the side view and the band structure of C_6H_6 on PG for vdW-DF (a), vDW-DF2-C09 (b), and Grimme-D2 (c).	39
Figure 3.6 The top view, the side view and the band structure of C_7H_8 on PG for vdW-DF (a), vDW-DF2-C09 (b), and Grimme-D2 (c).	39
Figure 3.7 PDOS and charge density plot of C_6H_6 on PG for vdW-DF (a), vDW-DF2-C09 (b), and Grimme-D2 (c). The isovalue is set to $\pm 0.00011 \text{ \AA}^{-3}$	40
Figure 3.8 PDOS and charge density plot of C_7H_8 on PG for vdW-DF (a), vDW-DF2-C09 (b), and Grimme-D2 (c). The isovalue is set to $\pm 0.0003 \text{ \AA}^{-3}$	40
Figure 3.9 The benchmark study for Gaussian broadening value: (a) 0.01 Ry, (b) 0.015 Ry, and (c) 0.02 Ry.	42
Figure 3.10 PDOS plot of C_6H_6 on PG (a), and d and f-states of C_6H_6 and PG including DOS (b).	43
Figure 3.11 The different initial configurations for C_6H_6 (a) and C_7H_8 (b) on VG.	43
Figure 3.12 The top view, the side view and the band structure of C_6H_6 on spin-unpolarized VG for vdW-DF (a), vDW-DF2-C09 (b), and Grimme-D2 (c).	46
Figure 3.13 The top view, the side view and the band structure of C_6H_6 on spin-polarized VG for vdW-DF (a), vDW-DF2-C09 (b), and Grimme-D2 (c).	46
Figure 3.14 The top view, the side view and the band structure of C_7H_8 on spin-unpolarized VG for vdW-DF (a), vDW-DF2-C09 (b), and Grimme-D2 (c).	47
Figure 3.15 The top view, the side view and the band structure of C_7H_8 on spin-polarized VG for vdW-DF (a), vDW-DF2-C09 (b), and Grimme-D2 (c).	47

Figure 3.16 PDOS and charge density plots of C ₆ H ₆ on VG for spin-unpolarized vdW-DF (a), vdW-DF2-C09 (b), and Grimme-D2 (c). The isovalue is set to $\pm 0.00029 \text{ \AA}^{-3}$	48
Figure 3.17 PDOS and charge density plots of C ₆ H ₆ on VG for spin-polarized vdW-DF (a), vdW-DF2-C09 (b), and Grimme-D2 (c). The isovalue is set to $\pm 0.0002 \text{ \AA}^{-3}$	49
Figure 3.18 PDOS and charge density plots of C ₇ H ₈ on VG for spin-unpolarized vdW-DF (a), vdW-DF2-C09 (b), and Grimme-D2 (c). The isovalue is set to $\pm 0.00042 \text{ \AA}^{-3}$	49
Figure 3.19 PDOS and charge density plots of C ₇ H ₈ on VG for spin-polarized vdW-DF (a), vdW-DF2-C09 (b), and Grimme-D2 (c). The isovalue is set to $\pm 0.0004 \text{ \AA}^{-3}$	50
Figure 3.20 The different initial configurations for C ₆ H ₆ and C ₇ H ₈ on DG.	50
Figure 3.21 The top view, the side view and the band structure of C ₆ H ₆ on DG for vdW-DF (a), vdW-DF2-C09 (b), and Grimme-D2 (c).	51
Figure 3.22 The top view, the side view and the band structure of C ₇ H ₈ on DG for vdW-DF (a), vdW-DF2-C09 (b), and Grimme-D2 (c).	52
Figure 3.23 PDOS and charge density plots of C ₆ H ₆ on DG for vdW-DF (a), vdW-DF2-C09 (b), and Grimme-D2 (c). The isovalue is set to $\pm 0.00019 \text{ \AA}^{-3}$	52
Figure 3.24 PDOS and charge density plots of C ₇ H ₈ on DG for vdW-DF (a), vdW-DF2-C09 (b), and Grimme-D2 (c). The isovalue is set to $\pm 0.00035 \text{ \AA}^{-3}$	53
Figure 3.25 The adsorption energy curve of bilayer graphene with vdW-DF (a), vdW-DF2-C09 (b), and Grimme-D2 (c).	55
Figure 3.26 The top view and the side view for optimized geometries of C ₆ H ₆ on PP for vdW-DF (a), vdW-DF2-C09 (b), and Grimme-D2 (c).	55

Figure 3.27 The top view and the side view for optimized geometries of C_7H_8 on PP for vdW-DF (a), vDW-DF2-C09 (b), and Grimme-D2 (c).	56
Figure 3.28 The top view and the side view for optimized geometries of spin-unpolarized C_6H_6 on PV for vdW-DF (a), vDW-DF2-C09 (b), and Grimme-D2 (c).	56
Figure 3.29 The top view and the side view for optimized geometries of spin-polarized C_6H_6 on PV for vdW-DF (a), vDW-DF2-C09 (b), and Grimme-D2 (c).	57
Figure 3.30 The top view and the side view for optimized geometries of spin-unpolarized C_7H_8 on PV for vdW-DF (a), vDW-DF2-C09 (b), and Grimme-D2 (c).	57
Figure 3.31 The top view and the side view for optimized geometries of spin-polarized C_7H_8 on PV for vdW-DF (a), vDW-DF2-C09 (b), and Grimme-D2 (c).	57
Figure 3.32 The top view and the side view for optimized geometries of C_6H_6 on PD for vdW-DF (a), vDW-DF2-C09 (b), and Grimme-D2 (c).	58
Figure 3.33 The top view and the side view for optimized geometries of C_7H_8 on PD for vdW-DF (a), vDW-DF2-C09 (b), and Grimme-D2 (c).	58
Figure 3.34 Band structure of (1) PP alone, (2) C_6H_6 on PP, and (3) C_7H_8 on PP for vdW-DF (a), vDW-DF2-C09 (b), and Grimme-D2 (c).	59
Figure 3.35 Band structure of (1) PV alone, (2) C_6H_6 on PV, and (3) C_7H_8 on PV for vdW-DF (a), vDW-DF2-C09 (b), and Grimme-D2 (c).	59
Figure 3.36 Band structure of (1) PV alone, (2) C_6H_6 on PV, and (3) C_7H_8 on PV for spin-polarized vdW-DF (a), vDW-DF2-C09 (b), and Grimme-D2 (c).	60
Figure 3.37 Band structure of (1) PD alone, (2) C_6H_6 on PD, and (3) C_7H_8 on PD for vdW-DF (a), vDW-DF2-C09 (b), and Grimme-D2 (c).	60

Figure 3.38 PDOS and charge density plots of C ₆ H ₆ on PP for vdW-DF (a), vdW-DF2-C09 (b), and Grimme-D2 (c). The isovalue is set to ± 0.000095 \AA^{-3}	61
Figure 3.39 PDOS and charge density plots of C ₇ H ₈ on PP for vdW-DF (a), vdW-DF2-C09 (b), and Grimme-D2 (c). The isovalue is set to ± 0.0003 \AA^{-3}	61
Figure 3.40 PDOS and charge density plots of C ₆ H ₆ on PV for spin-unpolarized vdW-DF (a), vdW-DF2-C09 (b), and Grimme-D2 (c). The isovalue is set to $\pm 0.00035 \text{\AA}^{-3}$	62
Figure 3.41 PDOS and charge density plots of C ₆ H ₆ on PV for spin-polarized vdW-DF (a), vdW-DF2-C09 (b), and Grimme-D2 (c). The isovalue is set to $\pm 0.0002 \text{\AA}^{-3}$	62
Figure 3.42 PDOS and charge density plots of C ₇ H ₈ on PV for spin-unpolarized vdW-DF (a), vdW-DF2-C09 (b), and Grimme-D2 (c). The isovalue is set to $\pm 0.0004 \text{\AA}^{-3}$	63
Figure 3.43 PDOS and charge density plots of C ₇ H ₈ on PV for spin-polarized vdW-DF (a), vdW-DF2-C09 (b), and Grimme-D2 (c). The isovalue is set to $\pm 0.0004 \text{\AA}^{-3}$	63
Figure 3.44 PDOS and charge density plots of C ₆ H ₆ on PD for vdW-DF (a), vdW-DF2-C09 (b), and Grimme-D2 (c). The isovalue is set to ± 0.00013 \AA^{-3}	64
Figure 3.45 PDOS and charge density plots of C ₇ H ₈ on PD for vdW-DF (a), vdW-DF2-C09 (b), and Grimme-D2 (c). The isovalue is set to ± 0.00038 \AA^{-3}	64
Figure 4.1 The geometry of the B doped vacancy-defected graphene (BVG).	70
Figure 4.2 The total energy (in eV) vs. total magnetization (in μ_B) for BVG. The energy values are referenced to the minimum energy.	70

Figure 4.3	The geometry of the B doped divacancy-defected graphene (BDG).	71
Figure 4.4	Total energy (in eV) vs. total magnetization (in μ_B) for BDG. The energy values are referenced to the minimum energy.	71
Figure 4.5	The optimized configurations of BVG.	73
Figure 4.6	The initial and the optimized configurations of BVG where B is doped as an adatom.	74
Figure 4.7	Band structure of PG (a), spin-polarized VG (b), BVG with configuration labeled as A (c), B (d), C (e), D (f), E (g) and adatom (h).	75
Figure 4.8	PDOS plot of PG (a), spin-polarized VG (b), BVG with configuration labeled as A (c), B (d), C (e), D (f), E (g) and adatom (h).	76
Figure 4.9	The optimized configurations of BDG.	77
Figure 4.10	The initial and the optimized configurations of BDG where B is doped as an adatom.	78
Figure 4.11	Total energy (in eV) vs. total magnetization (in μ_B) for where B is doped as an adatom. The energy values are referenced to the minimum energy.	78
Figure 4.12	Band structure of spin-unpolarized VG (a), DG (b) and BVG with configuration labeled as A (c), B (d), C (e), D (f), E (g), F (h), G (i), H (j), I (k) and adatom (l).	80
Figure 4.13	PDOS plot of spin-unpolarized VG (a), DG (b) and BVG with configuration labeled as A (c), B (d), C (e), D (f), E (g), F (h), G (i), H (j), I (k) and adatom (l).	81
Figure 5.1	Geometries of benzene (C_6H_6) (a), toluene (C_7H_8) (b), fluorobenzene (C_6H_5F) (c), benzonitrile (C_7H_5N) (d) and benzoic acid ($C_7H_6O_2$)(e). C: gray, H: blue, F: green, N: purple, and O: red.	85

Figure 5.2 Top view and side view of C_6H_6 on VG with spin-polarized vdW-DF2-C09 (a), and spin-unpolarized vdW-DF2-C09 (b), C_6H_6 on BVG with spin-polarized vdW-DF2-C09 (c), and spin-unpolarized vdW-DF2-C09 (d).	86
Figure 5.3 Top view and side view of C_7H_8 on VG with spin-polarized vdW-DF2-C09 (a), and spin-unpolarized vdW-DF2-C09 (b), C_7H_8 on BVG with spin-polarized vdW-DF2-C09 (c), and spin-unpolarized vdW-DF2-C09 (d).	87
Figure 5.4 Band structure of C_6H_6 adsorption on spin-unpolarized VG (a), spin-unpolarized BVG (b), spin-polarized VG (c), and spin-polarized BVG (d).	88
Figure 5.5 Band structure of C_7H_8 adsorption on spin-unpolarized VG (a), spin-unpolarized BVG (b), spin-polarized VG (c), and spin-polarized BVG (d).	88
Figure 5.6 PDOS and charge density plots of C_6H_6 on spin-polarized BVG (a), and spin-unpolarized BVG (b). The isovalue is set to $\pm 0.0003 \text{ \AA}^{-3}$	89
Figure 5.7 PDOS and charge density plots of C_7H_8 on spin-polarized BVG (a), and spin-unpolarized BVG (b). The isovalue is set to $\pm 0.00045 \text{ \AA}^{-3}$	89
Figure 5.8 Initial (a), and optimized configurations of C_6H_5F doped BVG with vdW-DF2-C09 (b), and without vdW-DF2-C09 (c).	90
Figure 5.9 Initial (a), and optimized configuration of parallel adsorption of C_6H_5F on BVG with vdW-DF2-C09 (b), and without vdW-DF2-C09 (c).	91
Figure 5.10 Initial (a), and optimized configuration of C_6H_5F on BVG with vdW-DF2-C09 (b), and without vdW-DF2-C09 (c) where B is doped as an adatom.	93

Figure 5.11 Band structure, PDOS and charge density plots of C ₆ H ₅ F on BVG with different configurations labeled as F1-1 (a), F2-1 (b), F3-1 (c), and adatom (d) where vdW dispersion forces are included. The isovalue is set to $\pm 0.0003 \text{ \AA}^{-3}$	94
Figure 5.12 Band structure, PDOS and charge density plots of C ₆ H ₅ F on BVG with different configurations labeled as F1-2 (a), F2-2 (b), F3-2 (c), and adatom (d) where vdW dispersion forces are excluded. The isovalue is set to $\pm 0.0004 \text{ \AA}^{-3}$	95
Figure 5.13 Initial (a), and optimized configurations of C ₇ H ₅ N doped BVG with vdW-DF2-C09 (b), and without vdW-DF2-C09 (c).	96
Figure 5.14 Initial (a), and optimized configuration of C ₇ H ₅ N on BVG with vdW-DF2-C09 (b), and without vdW-DF2-C09 (c) where B is doped as an adatom.	97
Figure 5.15 Band structure, PDOS and charge density plots of C ₇ H ₅ N on BVG with different configurations labeled as N1-1 (a), N1-2 (b), N2-1 (c), N2-2 (d), adatom (e), and adatom w/o vdW (f). The isovalue is set to $\pm 0.00015 \text{ \AA}^{-3}$	98
Figure 5.16 Initial (a), and optimized configurations of C ₇ H ₆ O ₂ doped BVG with vdW-DF2-C09 (b), and without vdW-DF2-C09 (c).	99
Figure 5.17 Initial (a), and optimized configuration of C ₇ H ₆ O ₂ on BVG with vdW-DF2-C09 (b), and without vdW-DF2-C09 (c) where B is doped as an adatom.	101
Figure 5.18 Band structure, PDOS and charge density plots of C ₇ H ₆ O ₂ on BVG with different configurations labeled as O1-1 (a), O2-1 (b), O3-1 (c), and adatom (d) where vdW dispersion forces are included. The isovalue is set to $\pm 0.00025 \text{ \AA}^{-3}$	102

Figure 5.19 Band structure, PDOS and charge density plots of $C_7H_6O_2$ on BVG with different configurations labeled as O1-2 (a), O2-2 (b), O3-2 (c), and adatom (d) where vdW dispersion forces are excluded. The isovalue is set to $\pm 0.00012 \text{ \AA}^{-3}$ 103

LIST OF ABBREVIATIONS

α -B	α -Rhombohedral Boron Crystal
β -B	β -Rhombohedral Boron Crystal
γ -B	γ -Orthorhombic Boron Crystal
adatom	Additional Atom
Al	Aluminum
B	Boron
B ₂ H ₆	Diborane
B ₃ N ₃ H ₃	Borazine
B(CH ₃) ₃	Trimethylborazine
BCl ₃	Boron Trichloride
BDG	Boron-Doped Divacancy-Defected Graphene
Be	Beryllium
BN	Boron Nitride
BVG	Boron-Doped Vacancy-Defected Graphene
BZ	Brillouin Zone
C	Carbon
C ₃ N ₃ H ₃	Triazine
C ₆ H ₅	Phenyl
C ₆ H ₅ F	Fluorobenzene
C ₆ H ₅ NH ₂	Aniline
C ₆ H ₅ NO ₂	Nitrobenzene
C ₆ H ₆	Benzene
C ₆ H ₆ O	Phenol
C ₇ H ₅ N	Benzonitrile
C ₇ H ₆ O	Benzaldehyde
C ₇ H ₆ O ₂	Benzoic Acid
C ₇ H ₈	Toluene
C ₁₀ H ₈	Naphthalene

C ₂₄ H ₁₂	Coronene
C ₃₂ H ₁₄	Ovalene
CNT	Carbon Nanotube
CO	Carbon Monoxide
Cu	Copper
CVD	Chemical Vapor Deposition
DCACP	Dispersion Corrected Atom-Centered Potential
DFT	Density Functional Theory
DG	Divacancy-Defected Graphene
DOS	Density of States
F	Fluorine
F4-TCNQ	Tetrafluoro-Tetracyanoquinodimethane
Fe	Iron
GGA	Generalized Gradient Approximation
GO	Graphene Oxide
H	Hydrogen
H ₂ O	Water
HCl	Hydrogen Chloride
HCN	Hydrogen Cyanide
HER	Hydrogen Evolution Reaction
HF	Hydrofluoric Acid
<i>HF</i>	The Hellman-Feynman Theorem
HOMO	Highest Occupied Molecular Orbital
LAP	Local Atomic Potential
LDA	Local Density Approximation
LiBs	Lithium Ion Batteries
LUMO	Lowest Onoccupied Molecular Orbital
N	Nitrogen
NEMS	Nanoelectromechanical System
NH ₃	Ammonia
Ni	Nickel
NO	Nitric Oxide
NO ₂	Nitrogen Dioxide
O	Oxygen

ORR	Oxygen Reduction Reaction
P	Phosphorus
PAH	Polycyclic Aromatic Hydrocarbon
PBE	The Perdew-Burke-Ernzerhof Exchange Functional
PDOS	Partial Density of States
PD	Divacancy-Defected Graphene Layer On Top Of Pristine Graphene Layer
PhB(OH) ₂	Phenylboronic Acid
PP	Pristine Graphene Layer On Top Of Another Pristine Graphene Layer
PV	Vacancy-Defected Graphene Layer On Top Of Pristine Graphene Layer
PWscf	Plane-Wave-Self-Consistent Field
QE	Quantum Espresso
revPBE	The Revised Perdew-Burke-Ernzerhof Exchange Functional
S	Sulphur
TCNE	Tetracyanoethylene
vdW	Van Der Waals
VG	Vacancy-Defected Graphene
XC	Exchange-Correlation Functional

CHAPTER 1

INTRODUCTION

In the past few decades, nanomaterials have received increasing attention with the development of nanotechnology. They display unique properties when compared with their bulk counterparts. These properties have opened up numerous possibilities of using nanomaterials in many applications such as drug delivery [1], sensors [2], hydrogen storage [3,4] and solar cells [5].

Materials at the nanoscale exhibit properties that are completely different from the macroscopic scale. As the system size approaches the nanoscale, many special and useful features of nanomaterials emerge. Carbon nanotubes [6], nanowires [7], graphene [8] and quantum dots [9] are some of the most commonly investigated nanoscale materials in the literature displaying a much wider range of physical, mechanical, electrical and magnetic properties compared with their bulk forms. The electrical [10] and thermal [11] resistances of nanoscale materials go down to very low values while the magnetization [12, 13] may emerge despite the fact that bulk form of such materials does not exhibit magnetic properties. Small structural and compositional changes can lead to large variations in electronic and optical properties of the nanomaterials. This large selection of properties enables the fabrication of devices tailored specifically to the goals of each application. Since the properties of a specific material can not be extrapolated by simply scaling down the bulk material scale of that material, experimental work supported by an atomistic scale description of such systems becomes crucially important in materials design.

In this thesis, we focus on pristine and defective graphene, highlighting potential for functionalization with the use of a wide variety of molecules. This chapter provides

an overview of the properties of graphene and its extraordinary properties.

1.1 Graphene

Since carbon can form various organic compounds with other elements, in addition to the capability of forming a variety of allotropes, it receives significant attention in the scientific community [14]. Two of its allotropes, diamond and graphite, have been known since antiquity. A recent allotrope, synthesized successfully for the first time in 2004 [15], is the two-dimensional graphene.

Graphite is a three dimensional layered hexagonal lattice of carbon atoms. A single layer of graphite forms a two dimensional material namely graphene. In the broader sense, graphene is a single layer of carbon atoms bonded in the form of two-dimensional hexagonal sp^2 bonds [15, 16]. Even if it was theoretically proved that a free ideal two-dimensional film cannot be obtained due to instability with respect to folding or twisting [17, 18], graphene is now synthesized routinely in many labs [15]. In graphite, each carbon atom forms a two-dimensional structure by bonding covalently with three neighboring carbon atoms. Each layer is then connected to the neighboring layers via van der Waals (vdW) forces to form graphite. Since the vdW bond strength is much weaker than the covalent bond, graphite can be easily separated into its constituent layers. The distance between two adjacent layers (3.35 Å) is much larger than the distance between two carbon atoms (C-C bond length) which is 1.42 Å [19, 20].

The unit cell and the Brillouin zone (BZ) of graphene are given in Figure 1.1. \vec{a}_1 and \vec{a}_2 are the lattice vectors in real space while \vec{b}_1 and \vec{b}_2 are reciprocal lattice vectors.

The real space unit vectors \vec{a}_1 and \vec{a}_2 of the hexagonal lattice are expressed as:

$$\vec{a}_1 = \left(\frac{\sqrt{3}}{2}a, \frac{a}{2} \right), \vec{a}_2 = \left(\frac{\sqrt{3}}{2}a, \frac{-a}{2} \right) \quad (1.1)$$

where a is $2.46 \text{ \AA} (1.42 \times \sqrt{3})$ which is the lattice constant of graphene and equal to $|\vec{a}_1|$ and $|\vec{a}_2|$.

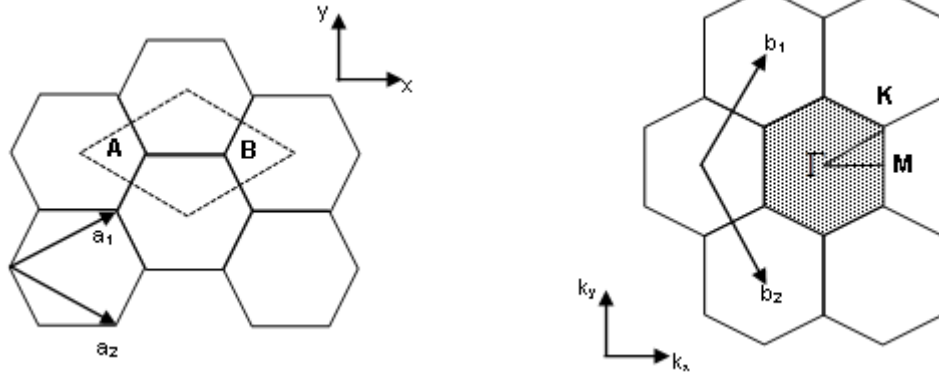


Figure 1.1: The unit cell and the BZ of graphene.

The reciprocal lattice vectors \vec{b}_1 and \vec{b}_2 of the reciprocal lattice are expressed as:

$$\vec{b}_1 = \left(\frac{2\pi}{\sqrt{3}a}, \frac{2\pi}{a} \right), \vec{b}_2 = \left(\frac{2\pi}{\sqrt{3}a}, \frac{-2\pi}{a} \right) \quad (1.2)$$

The first BZ is the shaded hexagon shown in Figure 1.1, and the highest symmetry points designated by Γ , K and M are the center, the corner and the center of the edge, respectively. The symmetry points are expressed as;

$$\Gamma = (0,0), K = \left(\frac{2\pi}{\sqrt{3}a}, \frac{2\pi}{3a} \right), M = \left(\frac{2\pi}{\sqrt{3}a}, 0 \right) \quad (1.3)$$

As shown in Figure 1.1, there are two carbon atoms per unit cell. Each carbon atom has four valence electrons three of which are utilized to make chemical bonds with the other three carbon atoms on the graphene plane [21] which are referred to as sigma (σ) bonds. σ bonds are responsible for the robustness of the lattice structure. The fourth electron is in the $2p_z$ orbital and perpendicular to the surface constituting the π system.

The two π electrons produce two bands, namely π and π^* , intersecting at six points in the first BZ, K and K' . As shown in Figure 1.2, these points are called Dirac points, and the electron dispersion relation is linear in their vicinity.

In many simple calculations, only π energy bands are considered since conduction is realized via the delocalized π electrons.

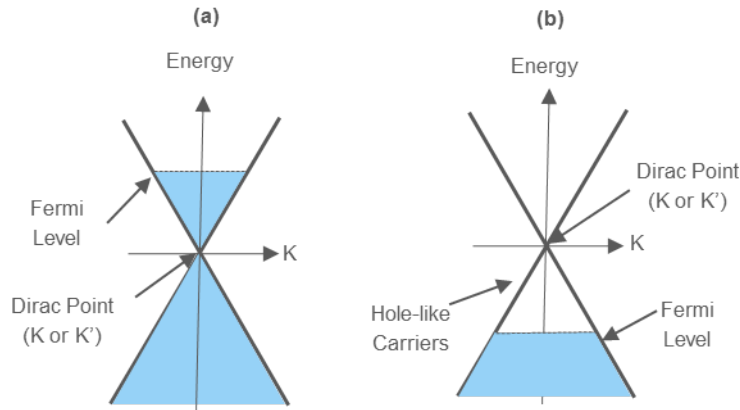


Figure 1.2: The electron dispersion relation of graphene (a) when the Fermi level is above the Dirac point, (b) when the Fermi level is below the Dirac point.

1.2 Applications Involving Graphene-Based Materials

Graphene can be seen as the building block of carbon materials such as graphite, carbon nanotubes, fullerenes and a variety of other materials. As such it has become one of the most intensively studied systems after the mechanical exfoliation (repeated peeling) of graphite to prepare graphene sheets in 2004 by Novoselov et al. [15]. In this study, it was shown that very thin graphite sheets (including monolayer graphene) can be obtained in stable and in high-quality crystal form under normal conditions, and these structures possess superior electronic properties.

Just six years after 2004, when it was shown to be an isolated and stable structure, its popularity enjoyed a steady increase in physics and material science, bringing the 2010 Nobel Prize for Physics. The reason behind this interest is the superior physical properties of graphene such as high elastic constants [22], mechanical stability [23, 24], low defect rate [25], very high electron mobility [26], long spin relaxation distance and time [27, 28] in addition to spin Hall effect [29, 30]. Additionally, with superior electronic properties and having at least 10 times more mobility than that of silicon, graphene seems to be a breakthrough in device technology, sensors, etc. [31, 32]. Several comprehensive review articles [33–36] show the potential of graphene and its derivatives.

Graphene has been widely investigated for the applications in drug delivery [1], sensors [2], hydrogen storage and solar cells [5]. For sensor applications, graphene is a

very sensitive sensor due to single atomic thickness. Unlike similar sensors, graphene allows recognition of even a single molecule with its high electrical conductivity and low noise level. Schedin et al. were able to detect the sticking and breaking events of various gas molecules by using graphene detectors at the micrometer scale [37]. Graphene-based nanoscale devices was already synthesized successfully [38, 39]. Recently, graphene has been used as an alternative nanofiller in the preparation of nanocomposites having improved mechanical [40], thermal (having thermal conductivity 25 times that of silicon) [41] and electrical properties [42]. Due to its excellent electrical conductivity and mechanical flexibility, graphene has great potential of replacing metal conductors in electronic devices [43]. Graphene is also considered as an attractive material for nanoelectromechanical system (NEMS) applications with properties such as high strength, low mass density and high elastic constants.

One of the most interesting electronic feature of graphene is massless Dirac fermions. As mentioned previously, the Fermi surface of graphene consists of six points at the edges of the BZ where the valence and conduction bands meet with linear dispersion. The dynamics of these particles are similar to the massless fermions in quantum electrodynamics. As a result, it is possible to observe the quantum Hall effect [44] in graphene at room temperature. Furthermore, the electron and hole densities can be adjusted up to 10^{13} cm^{-2} , and the charge carrier mobility can exceed $15 \times 10^3 \text{ cm}^2/\text{Vs}$ even at room temperature [15, 31, 44].

While monolayer graphene is a semimetal, it was demonstrated that bilayer graphene can be treated as a variable band-gap semiconductor by applying an external electric field perpendicular to the structure [45].

Even if graphene has been explored in several investigations for the electronics applications, it has one very severe limitation as it has no band gap [34, 46, 47]. Since the band gap governs the operation of devices such as p-n junctions, transistors, photo diodes and lasers, having no band gap limits the usage of graphene in electronic devices due to the lack of a high on/off ratio [48]. In order to eliminate this limitation, several methods have been utilized under the umbrella approach of band gap engineering, including the introduction of defects, application of strain and chemical functionalization [8]. By tuning the band gap and controlling the location of the Fermi level,

flexibility is achieved in design and optimization of devices. The electronic properties of graphene can be changed by shifting the Fermi level relative to the Dirac point by controlling the carrier type and concentration through electrical [44, 48] or chemical doping [1, 48].

The functionalization techniques can be divided into three as defect introduction, doping and molecular adsorption. In the first technique, defects and additional atoms (adatoms) can be introduced to the network [33, 49, 50]. Point defects such as mono and divacancies and adatoms locally change the electronic structure and act as functionalization centers [39, 49–51]. By breaking down the symmetry of pristine graphene, point defects may induce magnetism in the graphene sheet [52, 53]. In this thesis, in addition to the pristine graphene, defective graphene with a single vacancy (VG) and a divacancy (DG) is considered for adsorption of organic molecules since the vacancy sites exhibit high reactivity with them [54–56].

In literature, there are several studies regarding the doping of graphene in order to obtain improved electronic properties. Depending upon the dopant type, the Fermi level can shift downwards or upwards. When compared with the number of valence electrons of C, the electron deficient atoms like boron (B), aluminum (Al), beryllium (Be) are the atoms causing Fermi level shift downwards (p-type doping) while the electron rich atoms like nitrogen (N) and alkali metals cause Fermi level shift upwards (n-type doping) [57–60]. Since the atomic radii of B and N are very close to the atomic radius of C atom, B and N are the mostly used atoms as dopants with which graphene becomes p-type and n-type, respectively [57, 61]. Parallel to the result obtained by Chen et al. [22], it was found that the charge carrier mobility of n-type graphene (n-doped) is in the range 200-450 cm^2/Vs [61] while the charge carrier mobility of undoped graphene is around $2 \times 10^5 \text{ cm}^2/\text{Vs}$ [29]. Furthermore, it was observed that band gap position shifts with respect to the Fermi energy [62] for both B and N doping. In numerous studies, it has been reported that B and N doping to graphene has a promising potential for energy storage applications such as lithium ion batteries (LiBs) [58] and with the altered chemical reactivity properties in the presence of dopant, B and N doped graphene can be used as bio-sensors [63, 64]. In this thesis, the change of electronic and magnetic properties as a result of B doping is investigated in Chapter 4. Additionally, B-doped vacancy-defected graphene (BVG) is studied as a substrate for

molecular adsorption of benzene (C_6H_6) derivatives on BVG and given in Chapter 5.

The third alternative way of functionalization can be achieved by means of covalently or noncovalently bonded atomic or molecular species adsorbed on graphene [65–67]. Among them, the adsorption of transition metal atoms [68], the bonding of light atoms including small gas molecules (H_2O , H_2 , O_2 , CO , NO_2 , NO , and NH_3) [69], aromatic and non-aromatic molecules to the graphene surface are among the most commonly studied. For the adsorption of small molecules, it has been reported that nitrogen dioxide (NO_2) and water (H_2O) act as acceptors (p-type doping), while ammonia (NH_3), carbon monoxide (CO), and nitric oxide (NO) act as donors (n-type doping) [48, 70]. In several studies, it has been observed that graphene can be n-doped by depositing alkali metal atoms on the surface [38]. For both techniques, it was observed that they were very effective in order to enhance the properties of graphene and to obtain processable graphene. However, electrical conductivity and surface area of functionalized graphene obtained from both cases were observed to decrease when compared with pure graphene [71]. Furthermore, in the presence of charged impurities, it was reported that carrier mobility of graphene is reduced [22]. As an example of a noncovalently bonded molecule, tetrafluoro-tetracyanoquinodimethane (F4-TCNQ) molecule is in the group of non-aromatic molecules with a strong electron affinity, 5.2 eV [72], and molecular adsorption of F4-TCNQ results in p-type doped graphene with charge of 0.3 e/molecule being transferred from the highest occupied molecular orbital (HOMO) to the lowest unoccupied molecular orbital (LUMO) of graphene [22, 59, 69, 73]. F4-TCNQ, the halogenated adsorbate, is widely used in organic solar cells as an electron acceptor [74] with decreased carrier mobility because of the molecular separation of adsorbate and graphene and as the concentration of adsorbate increases, the Fermi level of graphene shifts towards the Dirac point. In order to see the effect of vdW interactions to the binding of molecules on graphene surfaces and since graphene has been observed to be a promising material for DNA sequencing [75–79], Le et al. [80] studied the physisorption of DNA bases namely adenine, cytosine, guanine, and thymine on graphene while Cho et al. [81] studied noncovalent interactions of these DNA bases with naphthalene and graphene. In DNA related studies, the binding energies of nucleobases on graphene were found to be 9.31, 8.48, 8.53, 7.30 kcal/mol (404, 368, 370, 317 meV/molecule) for guanine,

adenine, thymine, and cytosine, respectively while the binding separations were in the order of 3 Å for all DNA bases [80, 82, 83].

To compare the effect of functionalization techniques on electrical properties of graphene, the covalent functionalization of graphene converts the planar, sp^2 hybridization into a tetrahedral sp^3 resulting in distorted Dirac cone and introducing band gap while no change is observed in the structure after the noncovalent functionalization [84]. Noncovalent interactions basically involve hydrophobic, vdW, and electrostatic forces. VdW interaction between aromatic molecules and graphene is rather weak (order 50 meV) [85]. As a result, the superior physical properties of graphene are preserved, while improving its solubility, increasing conductivity or modifying other properties [29, 57, 61, 71, 86, 87].

The covalent functionalization of graphene is the most studied type of graphene functionalization because of resulting in more significant changes for electrical properties of graphene than the other techniques [84]. In literature, four different mechanisms have been offered to achieve covalent functionalization of graphene [86]. Different kinds of covalent functionalization have been possible with different modifying agents, dispersion stability in various solvents, dispersibility, and electrical conductivity [71]. The first mechanism offered is nucleophilic substitution where dodecyl amine [88], 4-aminobenzenesulfonic acid [89], polyethylene [90], dopamine [91] and polyglycerol [92] are the most commonly studied functionalizing molecules while sulfanilic acid [93] and polystyrene [94] are the functionalizing molecules for the second mechanism named as electrophilic addition. Amino acids and protein [95] can functionalize graphene covalently with condensation reaction. The last mechanism offered is addition reaction where polyacetylene [96], aryne [97] and alkylazides [98] are utilized as functionalizing molecules.

Another way of functionalization is through chemical adsorption of species, which has potential in applications since it enables graphene to be processed by solvent-assisted techniques. Chemical functionalization also maintains the properties of graphene by preventing its agglomeration [71]. As a starting material, graphene oxide (GO) has been used widely for the synthesis of processable graphene. The presence of additional carbonyl and carboxyl groups located at the edge of the sheets makes

GO sheets hydrophilic which allows the sheets to disperse in water [99–101]. Liu et al. [102] reported GO functionalization and the product is highly oxygenated resulting in improved noncovalent vdW interactions and leading to a range of solubility in water and organic solvents [101, 103–105].

There are various methods used for studying the physical properties of nanomaterials, and the theoretical methods are so well developed for designing materials with desired properties. One of the most preferred theoretical methods in calculations is the Density Functional Theory (DFT) that yields successful results in predetermining several properties of systems not yet synthesized and giving rise to experimental work. In this thesis, the structural and electronic properties of graphene based nanomaterials are investigated by DFT.

Accordingly, research objectives and scopes are defined, along with an outline of a roadmap for this research.

1.3 Research Objective and Scope

In this thesis, the focus is graphene functionalization by covalent and noncovalent techniques. With this respect, combination of three functionalization techniques given in Section 1.2, as defect introducing followed by B-doping and molecular adsorption, have been utilized in order to have more control on the properties of graphene. The method of choice is the state-of-the-art computational materials science methods based on DFT and its generalizations to treat long range vdW interactions.

Our aim in these investigations is to design, develop, and characterize novel materials and structures that can realize the functionality of conventional electronic devices in much smaller scales and with superior properties. It is our hope that theoretical and computational studies proposed in this thesis will support, clarify, and possibly lead to some experimental studies in graphene device physics.

Our work explores the complex interplay between defects, dopants and adsorption of organic molecules. As a benchmark of our method, the well-known adsorption characteristics of C_6H_6 on pristine graphene are reproduced. To see the effect of

different vdW corrections and functionals on adsorption geometry, adsorption energy and band structure, two different vdW functionals are used, namely vdW-DF [106], vdW-DF2-C09 [107,108] and one vdW correction is used, namely Grimme-D2 [109]. This study reveals that the vdW-DF2-C09 exchange-correlation protocol for the vdW interactions produces the closest agreement with literature.

Using this protocol, the adsorption of C_6H_6 and toluene (C_7H_8) is investigated on bilayer graphene to understand the effects of number of layers on adsorption characteristics. This study reveals an interesting fact that the presence of the second layer increases the adsorption energy by approximately 70 meV for both molecules.

As a means of extending the degree of control over functionalization, two complementary, and sometimes opposing techniques are introduced simultaneously. One or two B atoms are combined with various single and double vacancy (divacancy) configurations in a 6x6 graphene unit cell. Several configurations are explored and their electronic structures are found to reveal interesting trends.

Finally, C_6H_6 , C_7H_8 , fluorobenzene (C_6H_5F), benzonitrile (C_7H_5N), and benzoic acid ($C_7H_6O_2$) molecules are adsorbed on the B-doped defected sheets to further enhance our understanding of functionalization. While C_6H_5F and $C_7H_6O_2$ are found to adsorb through weak vdW interactions, C_7H_5N molecules are observed to form strong covalent bonds with the atoms surrounding the defect, and in particular the B atoms. The molecules are seen to introduce an unexpected reconstruction of the defective, doped graphene substrate and as a result induce significant changes to the electronic structure.

1.4 Organization of This Dissertation

Figure 1.3 presents the roadmap of this thesis, including significance of research topic and research objective, theoretical background, computational details of functionalization techniques and results.

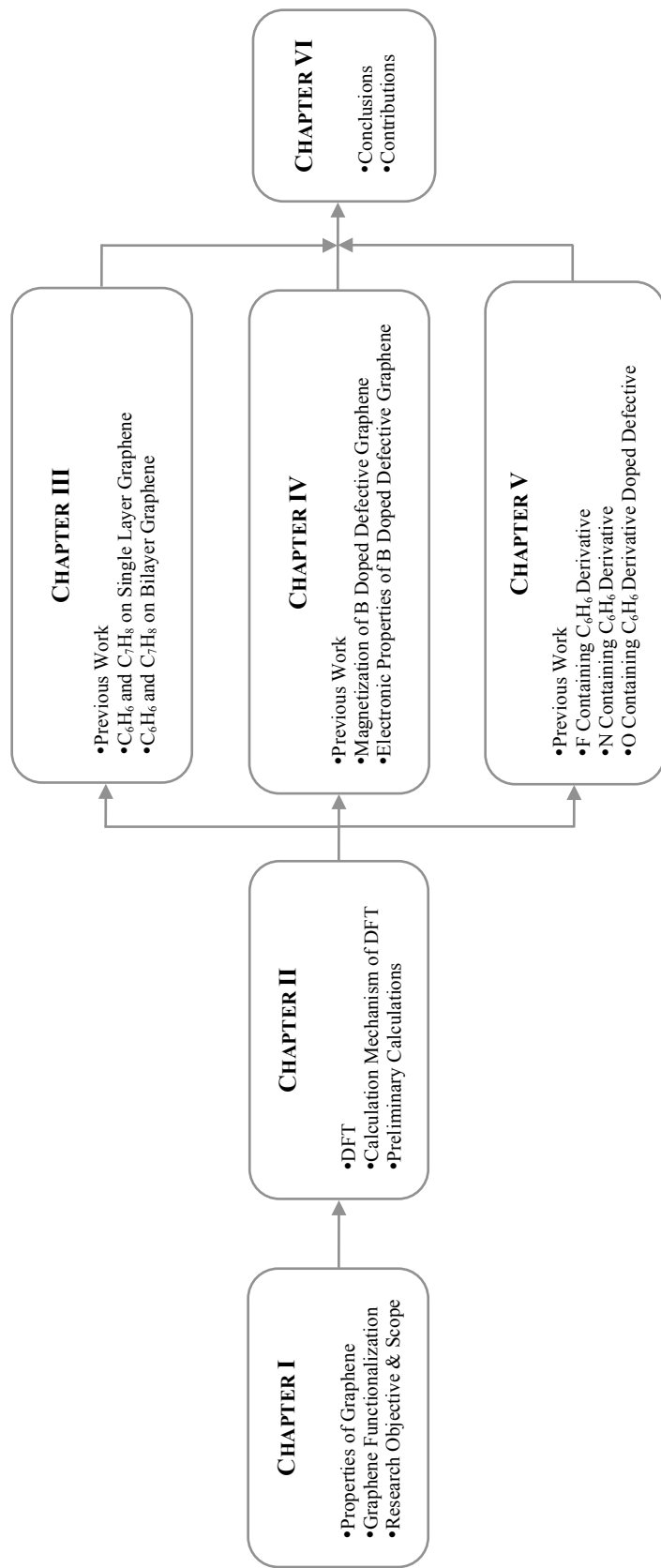


Figure 1.3: The organization of thesis.

The significance of research topic and objective are discussed in Chapter 1 while Chapter 2 provides detailed theoretical information about DFT utilized throughout this thesis followed by the preliminary calculations including benchmark study for the lattice constant and the band structure calculation of pristine and defective graphene.

In Chapter 3, we study the adsorption of organic molecules on pristine and defective graphene by choosing two types of organic molecules namely C_6H_6 and C_7H_8 . As defective graphene, VG and DG graphene are explored. In addition to adsorption of organic molecules on single layer graphene, C_6H_6 and C_7H_8 are also adsorbed on bilayer graphene in order to compare with experimental studies in the literature.

In Chapter 4, the main structure in focus is B doping to defective graphene, as BVG and B-doped divacancy-defected graphene (BDG), in order to investigate the change of electronic properties. In addition to these calculations, magnetization properties of the obtained structures are also studied.

In Chapter 5, the next aim is to concentrate on organic molecules. By exploring large number of organic dopants being adsorbed on graphene surface, adsorption energies are calculated with the most stable adsorption geometry. After calculations of B doping to defective graphene given in Chapter 4, additional molecule doping to BVG is studied by choosing additional molecules from C_6H_6 derivatives namely C_7H_8 , C_6H_5F , C_7H_5N , and $C_7H_6O_2$. Conclusions are summarized in the last chapter.

CHAPTER 2

THEORETICAL BACKGROUND

Determining the physical properties of many-particle systems such as atoms, molecules and solids requires solving the Schrödinger equation [110] for a many-particle system. Since the degrees of freedom of many electron systems are large, the solution of the Schrödinger equation for such systems is extremely difficult. In this case, there are many advantages of using a theoretical approach that focuses on particle density instead of the wave function [111]. The first such density-based approach was put forward by Thomas and Fermi, constituting a precursor DFT [112, 113]. The theoretical basis of DFT was first established by Hohenberg-Kohn [114] while the practical solution was made possible by Kohn and Sham and the constant evolution of computational resources [111, 115, 116]. Besides being a fundamental theory in the computation of electronic structures of solids, DFT has also played a major role in determining the physical and chemical properties of nanomaterials in recent years.

In this chapter, we give a brief account of the theoretical foundations of the DFT methodology as well as the approximations and technicalities necessary for its practical implementation. We also present the calculation details utilized in the rest of the thesis and some benchmark calculations.

2.1 Density Functional Theory

2.1.1 The Schrödinger Equation

In quantum mechanics, the Schrödinger equation has to be solved and many-body wave function has to be obtained in order to describe the physical properties of the many-body system. For an atomic or molecular system consisting of N electrons with coordinates $\vec{r}_1, \dots, \vec{r}_N$ and M nuclei with coordinates $\vec{R}_1, \dots, \vec{R}_M$, this equation is [117]:

$$\hat{H}\Psi_i(\vec{r}_1, \dots, \vec{r}_N; \vec{R}_1, \dots, \vec{R}_M) = E_i\Psi_i(\vec{r}_1, \dots, \vec{r}_N; \vec{R}_1, \dots, \vec{R}_M) \quad (2.1)$$

where Ψ_i is the many-body wave function of the i^{th} state of the system containing all the information available about the system. Here, E is the energy of the system, and \hat{H} is the many-body Hamiltonian operator. As seen in Equation 2.1, the wave function of a many-particle system depends on the coordinates of the nuclei, \vec{R}_I , and the coordinates of the electrons, \vec{r}_i , while the many-body Hamiltonian operator for an N -electron system is described as:

$$\begin{aligned} \hat{H} &= \hat{T}_e + \hat{T}_n + \hat{V}_{ee} + \hat{V}_{en} + \hat{V}_{nn} \\ &= -\frac{1}{2} \sum_{i=1}^N \nabla_i^2 - \frac{1}{M_A} \sum_{A=1}^M \nabla_A^2 - \sum_{i=1}^N \sum_{A=1}^M \frac{Z_A}{r_{iA}} + \sum_{A=1}^M \sum_{A < B}^M \frac{Z_A Z_B}{R_{AB}} + \sum_{i=1}^N \sum_{i < j}^N \frac{1}{r_{ij}} \end{aligned} \quad (2.2)$$

where, A and B represent nuclei while i and j denote electrons in the system. Additionally, r_{iA} is the electron-nuclei distance, R_{AB} is the distance between nuclei and r_{ij} is the distance between electrons.

For systems with a Hamiltonian seen in Equation 2.2, it is quite difficult to solve the Schrödinger equation analytically or numerically, and it is complicated to describe physical and chemical properties. For the sake of convenience, it is possible to simplify the problem by using the Born-Oppenheimer approximation where since the mass of the nucleus is much larger than the mass of the electron, is treated as stationary [118]. According to this approximation, the electrons adapt to the motion of atoms instantaneously. Therefore, we are able to separate the electronic and nuclear

degrees of freedom, treating the nuclei as classical particles. We then only concern ourselves with the electronic Hamiltonian:

$$\begin{aligned}\hat{H} &= \hat{T}_e + \hat{V}_{en} + \hat{V}_{ee} \\ &= -\frac{1}{2} \sum_{i=1}^N \nabla_i^2 - \sum_{i=1}^N \frac{Z_i}{|\vec{r} - \vec{r}_i|} + \sum_{i=1}^N \sum_{l=1}^N \frac{1}{R_{il}}\end{aligned}\quad (2.3)$$

The electronic Schrödinger equation is reduced to:

$$\hat{H}_{elec} \Psi_{elec} = E_{elec} \Psi_{elec} \quad (2.4)$$

In the following sections, we present a brief account of the steps necessary to convert this many-particle description into a density-based one.

2.1.2 Hohenberg-Kohn Theorem

An alternative way to the direct solution for the Schrödinger equation is to focus on the electron density instead of wave function having $4N$ (3 position, 1 spin for each electron) variables. This alternative way was introduced by Hohenberg and Kohn [114] which gave rise to DFT shifting the focus from the full wave function to density

In terms of the wave function, the electron density can be written as:

$$\rho(\vec{r}) = N \int \dots \int |\Psi(\vec{r}, \vec{r}_2, \dots, \vec{r}_N)|^2 d\vec{r}_2 d\vec{r}_3 \dots d\vec{r}_N \quad (2.5)$$

Integration over all space of electron density gives total number of electron as:

$$\int \rho(\vec{r}) d\vec{r} = N \quad (2.6)$$

In 1964, Hohenberg and Kohn proposed two theorems [114] giving rise to DFT. According to their first theorem, the ground state energy of a system of interacting electrons in an external potential is a functional of $\rho(\vec{r})$ [119] determining all properties

of the ground state including kinetic energy, $T[\rho]$, potential energy, $V[\rho]$ and total energy, $E[\rho]$.

$$E[\rho] = T[\rho] + V_{ne}[\rho] + V_{ee}[\rho] = \int \rho(\vec{r}) v(\vec{r}) dr + F_{HK}[\rho] \quad (2.7)$$

where $V_{ee}(\rho)$ is the potential energy of the electron-electron interactions, $V_{ne}(\rho)$ is the potential energy of the nucleus-electron interactions, and $v(\vec{r})$ is the external potential. $F_{HK}[\rho]$ is the universal Hohenberg-Kohn functional and described as:

$$F_{HK}[\rho] = T(\rho) + V_{ee}[\rho] \quad (2.8)$$

where $T(\rho)$ is the kinetic energy of the system. $V_{ee}(\rho)$ defined in Equations 2.7 and 2.8 consists of two terms as:

$$V_{ee}(\rho) = J[\rho] + \text{non-classical term} \quad (2.9)$$

In Equation 2.9, non-classical term consists of quantum mechanical effects such as self-interaction correction, exchange and Coulomb correlation, and $J[\rho]$ is the classical Coulombic interaction between the electrons.

The second Hohenberg-Kohn theorem states that $F_{HK}[\rho]$ delivers the lowest energy if and only if the input density is the true ground state density meaning that the energy obtained from Equation 2.7 (given in Equation 2.10) represents an upper bound to the true ground state energy, E_0 with an external potential, \tilde{V}_{ext} and trial density, $\tilde{\rho}(\vec{r})$.

$$E_0 \leq E[\tilde{\rho}] = T[\tilde{\rho}] + V_{ne}[\tilde{\rho}] + V_{ee}[\tilde{\rho}] \quad (2.10)$$

As the Hohenberg-Kohn theorems are only formulated for the ground state, conventional DFT can not be rigorously used to calculate any excited state properties.

2.1.3 The Kohn-Sham Method

Shortly after the Hohenberg-Kohn theorem was proposed, the Kohn-Sham method was suggested an auxiliary system of noninteracting electrons was imagined whose

density was thought to be the same as the true system in the ground state. The density in this case can be written within the Kohn-Sham ansatz as:

$$n(\vec{r}) = \sum_i^N |\phi_i(\vec{r})|^2 \quad (2.11)$$

with the total energy

$$E[n(\vec{r})] = \sum_i^N \varepsilon_i \quad (2.12)$$

where ε_i are single-particle energy levels.

$F[\rho(\vec{r})]$ is separated into three parts as:

$$F[\rho(\vec{r})] = T[\rho(\vec{r})] + E_H[\rho(\vec{r})] + E_{xc}[\rho(\vec{r})] \quad (2.13)$$

where $T[\rho(\vec{r})]$ is the kinetic energy, $E_H[\rho(\vec{r})]$ is the Hartree energy, and $E_{xc}[\rho(\vec{r})]$ is the exchange correlation energy. To produce reasonably accurate values, approximations to the exchange-correlation functional have been utilized.

The kinetic energy of the system is given by:

$$T[\rho(\vec{r})] = - \sum_{j=1}^N \frac{1}{2} \int \psi_j^*(\vec{r}) \nabla^2 \psi_j(\vec{r}) d^3\vec{r} \quad (2.14)$$

$T[\rho(\vec{r})]$ corresponds to the kinetic energy of a set of N non-interacting Kohn-Sham particles. The difference between this energy and the true electronic energy is a part of the exchange-correlation term in Equation 2.13.

The Hartree energy, $E_H[\rho(\vec{r})]$ corresponds to the classical electrostatic energy of the electrons and is given by:

$$E_H[\rho(\vec{r})] = \frac{1}{2} \int \frac{\rho(\vec{r}) \rho(\vec{r}')}{|\vec{r} - \vec{r}'|} d^3\vec{r} d^3\vec{r}' \quad (2.15)$$

The energy expression given in Equation 2.18 must be minimized with respect to the orbitals in order to obtain the orbitals that give rise to the ground state energy. The

minimization of energy is performed under the usual constraint $\langle \psi_i | \psi_j \rangle = \delta_{ij}$. The resulting equations are the Kohn-Sham equations:

$$\left[-\frac{1}{2} \nabla^2 + \int \frac{\rho(\vec{r}')}{|\vec{r} - \vec{r}'|} d\vec{r}' + V_{xc}(\vec{r}) - \sum_A^M \frac{Z_A}{|\vec{r}_A - \vec{r}|} \right] \psi_i = \epsilon_i \psi_i \quad (2.16)$$

which needs to be solved self-consistently. The simple sum of Kohn-Sham energies overcounts the Hartree energy and includes a spurious term originating from the exchange-correlation energy. This sum must therefore be corrected appropriately to yield the ground state energy of the true system.

2.1.4 Exchange-Correlation Functionals

DFT models the electron correlation as a function of the electron density, $\rho(\vec{r})$. E_{xc} embodies both static and dynamic correlation. At this point, the quality of a DFT calculation depends largely on the choice of the exchange-correlation (XC) functional. Since the XC functional cannot be calculated exactly, numerous approximations have been developed throughout the years.

The very first approximation developed is local density approximation (LDA) in which main principle is taking the known result of a homogeneous electron gas system and applying it locally to a non-uniform system [120].

$$E_{xc}^{LDA}[\rho] = \int \rho(\vec{r}) \epsilon_{xc}(\rho(\vec{r})) d\vec{r} \quad (2.17)$$

where $\epsilon_{xc}(\rho(\vec{r}))$ is the exchange-correlation energy per electron for a uniform electron gas with the density $\rho(\vec{r})$. The values of $\epsilon_{xc}(\rho(\vec{r}))$ are obtained by Monte Carlo calculations [121] in practice. This energy per particle is then weighted with $\rho(\vec{r})$. This approximation gives good results for bulk properties while it is not appropriate for molecular systems where charge density is non-uniform. The atomic ground state energies and ionization energies are underestimated while the binding energies are overestimated [122, 123].

LDA can be improved by using the gradient of the density at a given point \vec{r} within the generalized gradient approximation (GGA). For this type of approximation, the

main principle is using the information about $\rho(\vec{r})$ at \vec{r} in addition to the information about the gradient of the charge density, $\nabla\rho(\vec{r})$.

$$E_{xc}^{GGA} = \int \rho(\vec{r}) \varepsilon_{xc}[\rho(\vec{r}), \Delta\rho(\vec{r})] d\vec{r} \quad (2.18)$$

In our work, GGA is used for all calculations.

2.1.5 Van der Waals Interactions

VdW forces result from the interaction of fluctuating charge distributions in one discernable fragment with those in an adjacent one. Although very weak vdW interactions between atoms and molecules play an important role in many systems [124]. Since conventional DFT fails to describe long-range electron correlations that are responsible for vdW forces [125, 126], some suggestions have been made recently in order to include the effect of vdW interactions in DFT [127–129]. These suggestions are based on either directly adding a semi-empirical dispersion correction to the total energy [124, 130] or reconstructing the exchange-correlation functional [106] that enables its inclusion self-consistently.

These suggestions are classified in literature as starting from the most approximate approach and leading to the more sophisticated one [129]. As shown in Figure 2.1, "stairway to heaven" [131] starts with a vdW corrected pseudopotential and continues with simple C_6 correction (DFT-D method), environment dependent C_6 correction (DFT-D3 and vdW(TS) methods) and non-local vdW correlation functional (vdW-DF).

The bottom step of the stairway shown in Figure 2.1 is the dispersion corrected atom-centered potentials (DCACP) [132] and the local atomic potentials (LAP) methods which involves the addition of a dispersion-corrected pseudopotential [90]. Since these simple approaches have become inadequate to be applied for all systems, it is necessary to have new suggestion and move to the next step.

The DFT-D method is based on a semi-empirical dispersion correction to the total energy, E_{DFT} . The energy functional is:

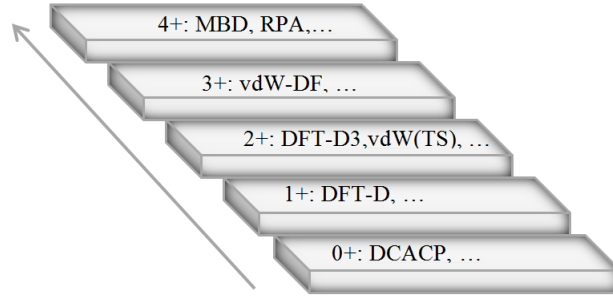


Figure 2.1: Classification of functionals as “stairway to heaven”.

$$E_{DFT-D} = E_{DFT} + E_{disp} \quad (2.19)$$

where E_{disp} is the dispersion and described as:

$$E_{disp} = - \sum_{A,B} \left(\frac{C_6^{AB}}{r_{AB}^6} + \frac{C_8^{AB}}{r_{AB}^8} + \frac{C_{10}^{AB}}{r_{AB}^{10}} + \dots \right) \quad (2.20)$$

The simplified form of E_{disp} used in DFT-D method is:

$$E_{disp} = - \sum_{A,B} \frac{C_6^{AB}}{r_{AB}^6} \quad (2.21)$$

where A and B are pairwise additives while C_6^{AB} is the dispersion coefficient. Even if C_6/r^6 correction is the most commonly used one, it represents only the leading term of the correction while neglecting many-body dispersion effects in addition to the faster decaying terms (C_8^{AB}/r_{AB}^8 , C_{10}^{AB}/r_{AB}^{10} , etc.).

To achieve better accuracy, a better estimate for the dispersion coefficient is required and for this purpose, Grimme developed an improved method commonly referred to as the DFT-D2 method [109, 124]. Similar with DFT-D method, DFT-D2 method adds an additional term to the total energy, and similar with the Equation 2.19, the energy functional becomes:

$$E_{DFT-D2} = E_{DFT} + E_{disp} \quad (2.22)$$

Different from DFT-D method, the dispersion coefficients are calculated from a for-

mula coupling ionization potentials and static polarizabilities of isolated atoms. E_{disp} with the damping function, $f(r_{AB}, A, B)$, is described as:

$$E_{disp} = - \sum_{A,B} f(r_{AB}, A, B) \frac{C_6^{AB}}{r_{AB}^6} \quad (2.23)$$

where $f(r_{AB}, A, B)$ is equal to one for large r values while it vanishes for small r values.

A more natural way of introducing vdW interactions to DFT calculation is to reconstruct the exchange-correlation functional entirely to include a non-local kernel. This method is commonly referred to in the literature as the vdW-DF method. In Figure 2.1, it is represented by the third step.

The vdW-DF method adds non-local (i.e., long range) correlations to local or semi-local correlation functionals and the exchange-correlation for this method, E_{xc} is given as:

$$E_{xc} = E_x^{GGA} + E_c^{LDA} + E_c^{nl} \quad (2.24)$$

where E_x^{GGA} is the exchange energy approximated within GGA, E_c^{LDA} is the correlation energy approximated within LDA, and E_c^{nl} is the non-local correlation energy describing dispersive interactions. E_c^{nl} is defined as:

$$E_c^{nl} = \int \int dr_1 dr_2 n(r_1) \varphi(r_1, r_2) n(r_2) \quad (2.25)$$

where $n(r)$ is the electron density, $\varphi(r_1, r_2)$ is integration kernel.

VdW-DF is an important development, however, it has drawbacks such as overestimating long range dispersion interactions. In order to overcome this overestimation, the method involving changes to exchange and non-local correlation terms has been suggested and named as vdW-DF2 [133, 134]. The Perdew-Burke-Ernzerhof (PBE) and revised PBE (revPBE) exchange functionals are mostly used in combination with the vdW-DF and vdW-DF2 method [136]. However, revPBE results in large intermolecular binding distances and inaccurate binding energies, C09 exchange has been proposed as an alternative way to remedy this shortcoming [107].

In Chapter 3, vdW-DF, vdW-DF2-C09 and Grimme-D2 (DFT-D2) will be used to study the effect of different vdW functionals and corrections on adsorption geometry, adsorption energy and band structure. These calculations reveal that the vdW-DF2-C09 exchange-correlation protocol for the vdW interactions produces the closest agreement with the literature, therefore vdW-DF2-C09 is used in the calculations presented in later chapters.

2.1.6 Pseudopotentials

Electrons can be divided into two groups as the core and the valence electrons around the nucleus. Core electrons are localized around the nucleus and not affected by chemical interactions. On the other hand, valence electrons play a major role in the formation of chemical bonds and in the determination of the electronic properties of materials. These electrons, which fill the valence orbitals, experience a field formed by the nucleus and the core electrons.

The wave functions of the valence electrons are orthogonal to the wave functions of the core electrons. In order to maintain this constraint, valence wave functions oscillate rapidly in the core region. This is due to the fact that the interaction potential between the valence electrons and the core electrons is very large in the region $r < r_c$ [137], as shown in Figure 2.2. Here, r_c is the core radius, the blue straight lines represent the pseudopotential and pseudo wave function while the red dashed lines are for real potential and real wave function.

In most periodic software that implements DFT, a plane wave basis is used to expand the Kohn-Sham orbitals. The sharp Coulombic potentials close to the nuclei necessitates a large number of plane wave basis functions in order to resolve the oscillations in the wave functions of the valence electrons in the core region. To avoid this and to limit the calculations only to the chemically relevant electrons, the pseudopotential approach has been developed which treats only valence electrons explicitly [138–140].

The generation of a pseudopotential begins with the solution of the Kohn-Sham equation for an isolated atom. Pseudowave functions are obtained by placing a smoother

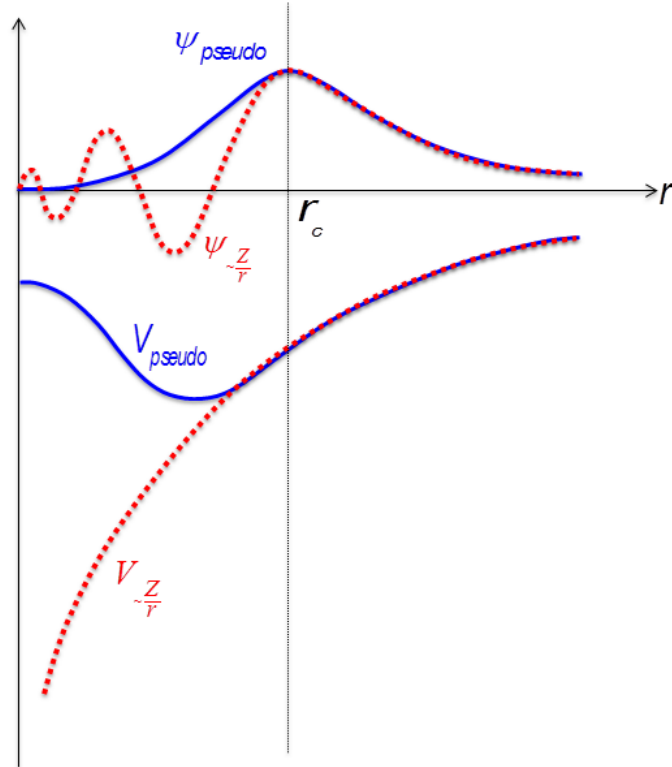


Figure 2.2: The real and pseudo potentials and wave functions.

function in place of the part of the real wave function oscillating in the core region ($r < r_c$). This wave function should be compatible with the real wave function outside the core region [141]. The Schrödinger equation is then inverted to obtain the pseudopotential, which must then be identical to the true potential outside the core region. In this thesis, we employ ultrasoft pseudopotentials [142] since they require a much smaller set of plane waves in the basis set expansion.

In our work, the interaction of the valence electrons with the atomic core states is described by ultrasoft pseudopotentials and we use PBE type ultrasoft pseudopotentials with vdW-DF2-C09 and Grimme-D2 while revPBE is used with vdW-DF for hydrogen (H) and carbon (C) in Chapter 3. In Chapter 4 and in Chapter 5, PBE type ultrasoft pseudopotentials are used for boron-doped vacancy-defected graphene (BVG) and boron-doped divacancy-defected graphene (BDG) calculations. Additionally, PBE type ultrasoft pseudopotentials are used for fluorine (F) and nitrogen (N) while PBE type Vanderbilt ultrasoft pseudopotential is used for oxygen (O) atom in Chapter 5.

2.2 Mechanism of a Density Functional Theory Calculation

2.2.1 Self-Consistency Cycle

The calculations in our work are performed by using the Quantum Espresso (QE) package [143] which uses a Plane-Wave-Self-Consistent field (PWscf) approach. QE is an open source code based on DFT, plane-waves and pseudopotentials aiming to solve the Kohn-Sham equations self-consistently. The flowchart of the self-consistency cycle [144] is shown in Figure 2.3.

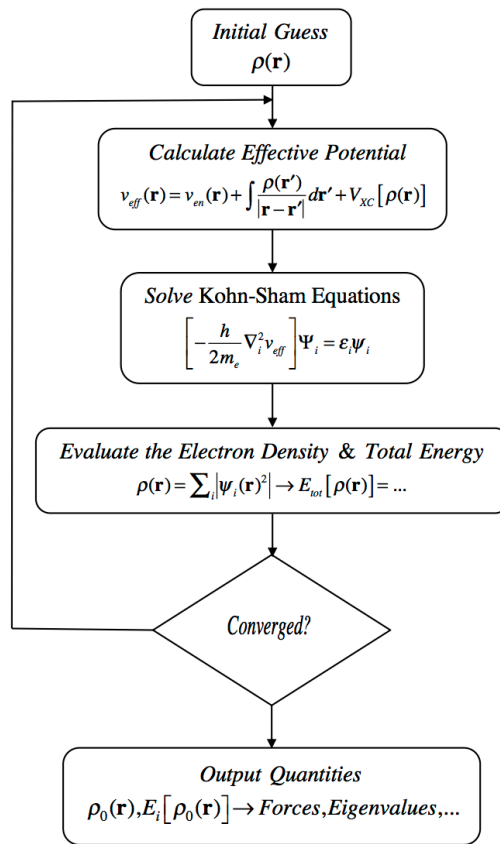


Figure 2.3: Kohn-Sham self-consistency cycle.

As shown in Figure 2.3, the initial density is selected in accordance with the atom type and the atomic positions. Afterwards, the Kohn-Sham equations for the Kohn-Sham orbitals are solved and the density obtained from the solution of these equations is compared to the initial density. If the density obtained is close enough to the density obtained in the previous cycle, the calculation is terminated. Otherwise, the second

step will be repeated with the calculated density. This process continues until there is agreement between the consecutive densities.

2.2.2 Structure Optimization

A system reaches the structural equilibrium configuration when the forces on the nuclei reach zero. Once the ground state density has been obtained through self-consistent iterations indicated in Section 2.2.1, the Kohn-Sham orbitals corresponding to this density can be used to calculate several properties of the system including the force on the atoms.

The Hellman-Feynman (*HF*) theorem is a general statement about derivatives of expectation values at the ground state and force for the electronic part is expressed as:

which states that the change in the Hamiltonian operator can be calculated by ignoring the change in the wave function while differentiating the energy to obtain forces. The atoms are displaced along the HF forces. Afterwards, the self-consistency cycle displayed in Figure 2.3 is repeated with the addition of electronic and ionic contributions to find the total force of *i*th atom.

2.2.3 Computational Details

The calculations presented in this thesis are performed by using QE package [143]. For the exchange-correlation functional, the Perdew-Burke-Ernzerhof (PBE) approximation is used [143]. The interaction of the valence electrons with the atomic core states is described by ultrasoft pseudopotentials. The Brillouin Zone (BZ) is sampled according to the Monkhorst-Pack scheme [145] with 3x3x1 k-points for 6x6 unit cells. A kinetic energy cutoff of 30 Ry for wave functions and 300 Ry for charge density are used in all calculations since they gave well-converged values for both graphene and molecules in the previous studies [64, 146–151].

Another point that has to be taken into account is that atoms are free to relax in each cell and the vacuum between periodic cells needs to be large enough in order to prevent the interaction. For this purpose, a vacuum thickness of 15 Å is used in all

calculations.

Electronic bands are calculated on the path between certain critical points in Brillouin zone. Starting from Γ (center of the Brillouin zone), the path reaches K and M. XCrysDen [152] and Jmol [153] are used to visualize the structures during calculations.

Density of states (DOS) is the total number of the states in a given energy interval. DOS is described as:

$$DOS(E) = \frac{1}{N} \sum_k \delta(E - \varepsilon_k) \quad (2.26)$$

where N is the number of wave vector, k is the phonon frequencies for wave vectors and ε_k is the energy of the single particle.

A partial density of states (PDOS) calculations are performed to obtain a projection of the Kohn-Sham orbitals onto a suitably defined atomic regions. The PDOS calculation is a useful tool for analyzing the charge transfer in a chemical process.

In addition to the DOS and PDOS calculations, the charge density difference calculations are performed to look at the difference or the effect of the adsorbed system's interaction with the substrate. These calculations are performed after structure optimization calculations. VESTA visualization software [154] is used in order to visualize charge density plots. Furthermore, charge transfer between the graphene network and the adsorbates are investigated using the Bader charge analysis implemented by Henkelman et al. [155]. Additionally, Löwdin charge analysis [156] is used for analyzing the charge transfer characteristics of benzene derivatives presented in Chapter 5.

2.3 Preliminary Calculations

2.3.1 Lattice Constant Optimization Calculations

As a benchmark, lattice constant optimization calculations for graphene were performed for the functionals and correction described in Section 2.1.5. To check whether turning on spin polarization has any effect on lattice constants, we conduct some calculations with spin-polarized exchange-correlation (XC) functionals as well. In our production calculations, we include spin-polarization.

In experimental studies given in literature, lattice constant of graphene (a) is 2.46 Å [157]. The optimized lattice constant (a) values and error with respect to experimental value are tabulated in Table 2.1. From these results, it may be concluded that the vdW-DF2-C09 yields the best results for graphene based structures, and it is observed that lattice constants are independent of spin magnetization. These benchmark tests are also in good agreement with the previous studies reported in literature [158, 159].

Table 2.1: The lattice constant optimization for graphene.

Functional	a (Å)	% error
vdW-DF	2.4629	0.1175
spin polarized vdW-DF	2.4629	0.1175
vdW-DF2-C09	2.4602	0.0096
spin polarized vdW-DF2-C09	2.4602	0.0096
Correction	a (Å)	% error
Grimme-D2	2.4615	0.0617
spin polarized Grimme-D2	2.4615	0.0617
	a (Å)	% error
PBE	2.4619	0.0766
spin polarized PBE	2.4617	0.0691

2.3.2 Pristine and Defective Graphene Calculations

As a basis for this work, the electronic properties of pristine graphene and graphene with point defects (mono and divacancy) have been reviewed. The other aim of these preliminary calculations is to test the accuracy of the parameters being used in the calculations.

For pristine graphene, as shown in Figure 2.4a, a 6x6 unit cell consisting of 72 C atoms is used. For the optimized geometry, bond length is calculated to be 1.4215 Å which agree well with the values reported in the literature [160, 161]. For graphene with point defects, 6x6 unit cells consisting of 71 C and 70 C atoms have been chosen to model vacancy-defected (VG) and divacancy-defected graphene (DG), respectively. For the geometry optimized structures, it is observed that total magnetization is equal to 0.00 μ_B per cell for DG while it is 1.43 μ_B per cell for VG in good agreement with the previous works [162–164]. From these results, it is concluded that there is no effect of magnetization for divacancy in graphene sheet.

The optimized geometries of spin-unpolarized VG, spin-polarized VG and DG are presented in Figure 2.4b, Figure 2.4c and Figure 2.4d, respectively. For VG, one of the C atoms in Figure 2.4b and in Figure 2.4c, surrounding the vacancy undergoes an out-of-plane displacement of about 0.48 Å resulting in a distorted structure while the remaining two atoms surrounding the vacancy move close to each other to a distance of 2.1 Å where the initial distance is 2.46 Å for pristine graphene. When spin-polarization is included, C atoms surrounding the defect comes closer to each other and one of the C atoms surrounding the vacancy becomes coplanar with 0.07 Å out-of-plane displacement while the initial displacement is 0.2 Å away from the planar surface.

In addition to pristine graphene, spin-unpolarized VG and DG, band structure calculations have been performed for spin-polarized VG to see the effect of spin polarization on the electronic properties of VG since magnetism is observed with a monovacancy in graphene sheet [52, 53] as indicated in Section 1.2. The optimized structures with their band structures are presented in Figure 2.4 in addition to their charge density and DOS plots. For the band structure of spin-polarized VG, red lines in Figure 2.4c

represent the majority spin while blue lines represent the minority spin. As seen from Figure 2.4a, for pristine graphene, the Fermi level appears at the Γ point due to zone folding and for VG, spin polarization lifts the degeneracies while the Fermi level is depressed below the original location similarly with DG.

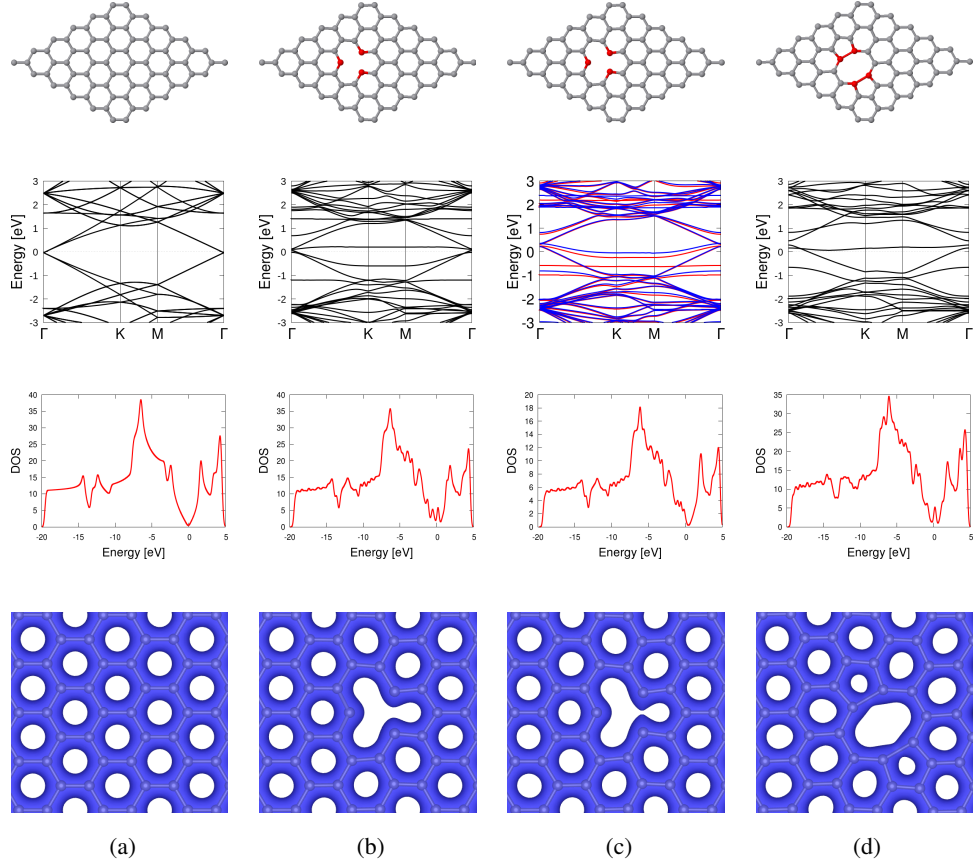


Figure 2.4: Optimized structures, band structures, DOS and charge density plots of pristine graphene (a), spin-unpolarized VG (b), spin-polarized VG (c), and DG (d).

For VG and DG, the defect formation energies are calculated from:

$$E_{def} = E_{def-gr} + \mu_C - E_{pr-gr} \quad (2.27)$$

where E_{def} is the defect formation energy, E_{def-gr} is the energy of defective graphene while μ_C is the chemical potential of the C atom which is taken as E_{pr-gr}/N where N is the number of C atoms in the unit cell of graphene and E_{pr-gr} is the energy of pristine graphene.

From Equation 2.27, VG and spin-polarized VG formation energies are calculated to be 7.80 eV and 7.60 eV, respectively which are very high due to the existence

of an under-coordinated carbon atom while being in good agreement with previous theoretical and experimental results [165–169]. On the other hand, DG formation energy is calculated to be 7.71 eV which shows similar trend with the previous studies where formation energies of divacancies in carbon nanotubes and graphene are found to be much lower than the formation energy of monovacancy, suggesting that the coalescence of monovacancies into divacancies is energetically favorable [169–174].

CHAPTER 3

ORGANIC MOLECULES ON PRISTINE AND DEFECTIVE GRAPHENE

In this chapter, we study the adsorption of benzene (C_6H_6) and toluene (C_7H_8) on pristine and defective graphene. In addition to single layer graphene, we study adsorption of C_6H_6 and C_7H_8 on bilayer graphene. Van der Waals (vdW) dispersion forces are included in order to treat molecule-graphene interaction. To see the effect of different vdW dispersion forces on adsorption geometry, adsorption energy and band structure, three different exchange-correlation functionals are employed: vdW-DF [106], vdW-DF2-C09 [107, 108] and Grimme-D2 [109].

3.1 Previous Work

C_6H_6 is a flat polycyclic aromatic hydrocarbon (PAH). C atoms (each carbon contains three sigma bonds) are each bonded to two neighboring C atoms and two H atoms. C_6H_6 is a colourless liquid with a characteristic odor evaporating into the air very quickly while dissolving slightly in water. It is mainly employed in the production of polystyrene and other chemicals such as detergents, dyes, pesticides and drugs [175]. Due to its industrial applications, adsorption characteristics of C_6H_6 is widely investigated in addition to its detection since exposure to C_6H_6 increases the risk of cancer and other illnesses [176, 177]. As indicated in Chapter 1, for applications involving graphene based devices, molecular adsorption on graphene with different chemical species such as small gas molecules [69, 70, 178, 179] are the subject of various theoretical [54, 70, 180–183] and experimental [15, 37] studies.

Non-covalent functionalization of graphene using various organic molecules [38,184] and bio-molecules [23] has attracted growing attention in electrical and optical applications. In many previous studies [185,186] C_6H_6 was investigated as a prototype for π - π interactions [187]. Different exchange-correlation functionals [106,188] were tested in order to provide an improved description of the long-range weak dipole-dipole interaction and the electronic structure of the interface between graphene and organic molecules [189]. For the adsorption of C_6H_6 on graphene, graphite or carbon nanotubes, the distance between the graphene sheet and C_6H_6 was calculated to be $3.60 \pm 0.2 \text{ \AA}$ based on the weak vdW forces [69,188,190,191] while adsorption energies range from 20 to 29 kJ/mol (207-301 meV/ C_6H_6 molecule) [20,186]. However, in some recent DFT studies, larger adsorption energies (79.2 kJ/mol - 821 meV/ C_6H_6 molecule) for C_6H_6 on graphene were calculated which would prevent the desorption of C_6H_6 [192].

Chakarova-Käck et al. [188] conducted vdW-DF calculations for the adsorption energies of C_6H_6 and naphthalene ($C_{10}H_8$) on graphite while Alzahrani [193] focused on the electronic properties of these adsorbed systems and found that graphene's low energy electronic properties remain unchanged upon C_6H_6 and $C_{10}H_8$ adsorption unless C_6H_6 was artificially placed very close to graphene resulting in a covalent bond formation [186,192,194]. Caciuc et al. [195] concluded that the strength of C_6H_6 -graphene interaction corresponds to physisorption with no significant charge transfer between adsorbent and adsorbate. In spite of the several studies for C_6H_6 adsorption on pristine graphene, the studies dealing with the adsorption of C_6H_6 on defective graphene are missing.

The other organic molecule studied in this work is toluene, a colorless, water insoluble molecule with the chemical formula C_7H_8 . C_7H_8 is a C_6H_6 derivative with an extra CH_3 group. Contrary to C_6H_6 , there are very few studies dealing with the adsorption mechanism of C_7H_8 on graphene [196], it has been observed that, electronic properties of graphene around the Dirac point are not disturbed by adsorption of C_7H_8 while the Fermi level remains at the Dirac point indicating that no charge transfer between C_7H_8 and graphene [197]. Similar to C_6H_6 , studies dealing with the adsorption of C_7H_8 on defective graphene are missing.

3.2 Organic Molecules on Single Layer Graphene

Before starting the adsorption calculations, C_6H_6 and C_7H_8 are optimized separately and the resulting geometries are used for the following calculations. The molecular adsorption energies are calculated using:

$$E_{ads} = E_{graphene} + E_{molecule} - E_{molecule+graphene} \quad (3.1)$$

where $E_{graphene}$ is the energy of graphene sheet, $E_{molecule}$ is the energy of an isolated neutral organic molecule, and $E_{molecule+graphene}$ is the total energy of the system consisting of the organic molecule and graphene. With this definition, positive adsorption energies correspond to stable adsorption geometries. For physisorbed species, $E_{molecule}$ and $E_{graphene}$ are both calculated using the relevant exchange-correlation functionals.

As a result of geometry optimization, equilibrium separation between the organic molecule and graphene can be obtained in addition to adsorption energy values. However, simple geometry optimization may miss the correct adsorption height values due to the possibility of multiple minima. As a check, we run a series of single-point scf calculations for a specified adsorption height value interval in order to obtain a better resolved profile. A similar study was conducted by Chakarova-Käck et al. [188] and for a direct comparison, the configuration utilized in their study is subjected to scf calculations. The configuration used for the parallel adsorption of C_6H_6 on pristine graphene (PG) is displayed in Figure 3.1 which will be referred to as site Br in Section 3.2.1.

For this scan, the adsorption height of C_6H_6 in the z-direction is changed from 2.5 Å to 4.5 Å with an increment of 0.1 Å an scf calculation is performed for each height, and equilibrium adsorption heights are determined from each data set. The adsorption energy curves with respect to different adsorption heights for vdW-DF, vdW-DF2-C09 and Grimme-D2 are shown in Figure 3.2 for C_6H_6 adsorption on 6x6 PG where the adsorption heights are calculated to be 3.43 Å, 3.27 Å and 3.19 Å for vdW-DF, vdW-DF2-C09 and Grimme-D2, respectively which are in very good agreement with the values tabulated in Table 3.1. For vdW-DF, the calculated adsorption height is in

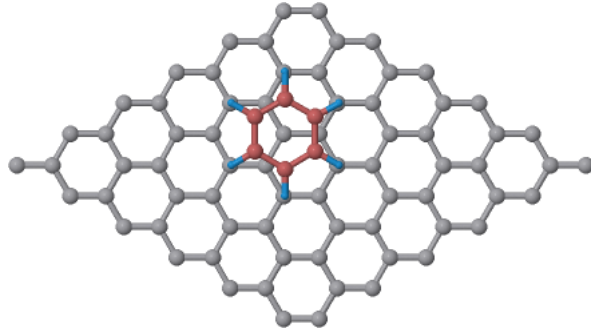


Figure 3.1: Configuration of C_6H_6 on single layer graphene for adsorption height calculations.

good agreement with the previous theoretical and experimental results reported to be $3.60 \pm 0.2 \text{ \AA}$ [188, 190, 191].

In order to probe the adsorption behaviour of C_6H_6 in lateral directions, the adsorption height values are fixed and the optimization calculations are performed where atomic positions in a plane parallel to the graphene sheet are free to change. After obtaining the optimized geometry, the final energy values are compared with the adsorption energy values presented in Figure 3.2 and it is observed that the difference is around 1 meV showing that the full optimization gives a robust geometry.

The defect formation energies of VG and DG are calculated using Equation 2.27 for vdW-DF, vdW-DF2-C09 and Grimme-D2. For VG, the formation energies are calculated to be 7.30 eV, 7.78 eV and 7.84 eV for vdW-DF, vdW-DF2-C09 and Grimme-D2, respectively and when spin-polarization is included, the formation energies reduce to 7.24 eV, 7.66 eV and 7.64 eV for vdW-DF, vdW-DF2-C09 and Grimme-D2, respectively. DG formation energies are calculated to be 7.10 eV, 7.77 eV and 7.79 eV for vdW-DF, vdW-DF2-C09 and Grimme-D2, respectively which shows the same trend with VG as formation energy is lowest for vdW-DF and formation energies for vdW-DF2-C09 (7.78 eV for VG and 7.77 eV for DG) are very similar with the formation energies where vdW interactions are excluded (7.80 eV for VG and 7.71 eV for DG) which confirms the indication in Section 2.3.1 that vdW-DF2-C09 yields the best results.

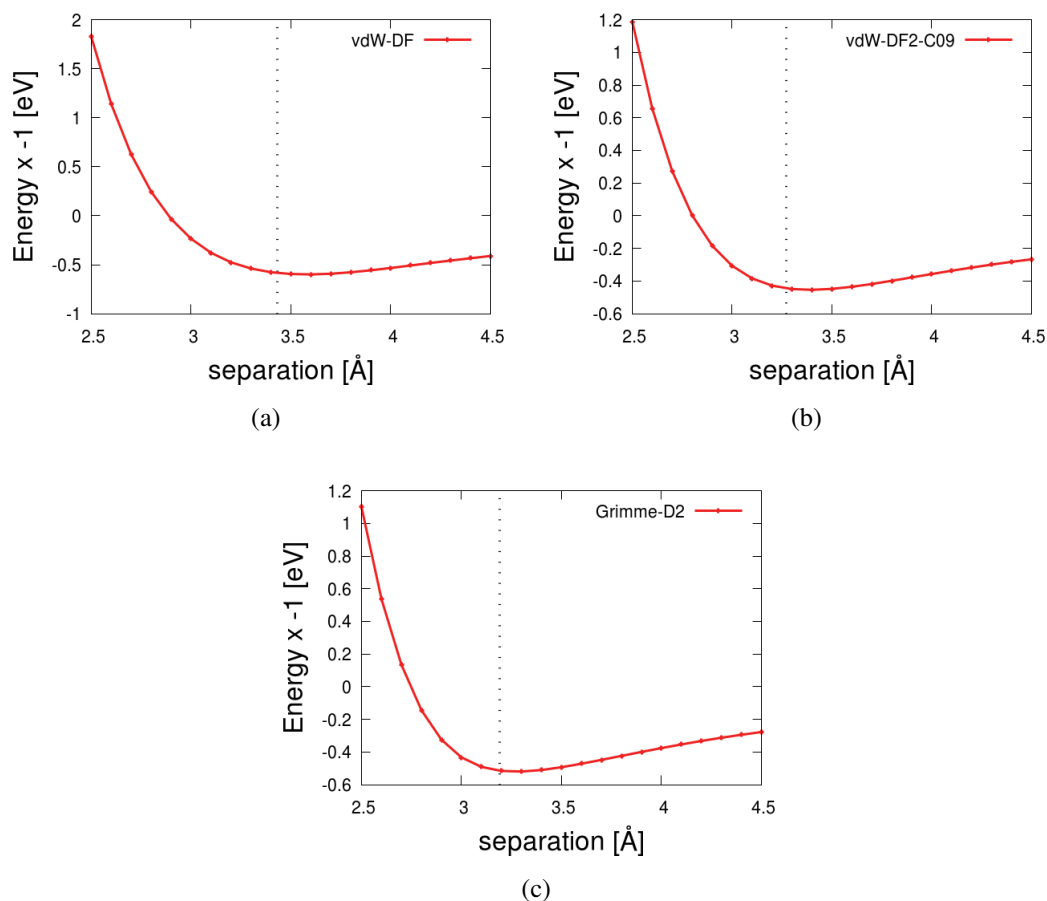


Figure 3.2: The adsorption energy curve of C_6H_6 on single layer graphene with vdW-DF (a), vdW-DF2-C09 (b), and Grimme-D2 (c).

3.2.1 Organic Molecules on Pristine Graphene

A 6x6 unit cell of PG, consisting of 72 atoms, is used as substrate during calculations. C_6H_6 and C_7H_8 are adsorbed on graphene, separately. In literature, it is stated that due to the unreactivity of organic molecules and graphene, organic molecules interact weakly with graphene [8]. In order to confirm this weak interaction and determine the preferred sites, 14 different configurations are investigated including both parallel and perpendicular adsorption of C_6H_6 and C_7H_8 . These configurations are seen in Figure 3.3 and Figure 3.4 along with labels where the letter "r" in the label indicates rotation along the axis perpendicular to the molecular plane with respect to the configuration labeled without the letter "r".

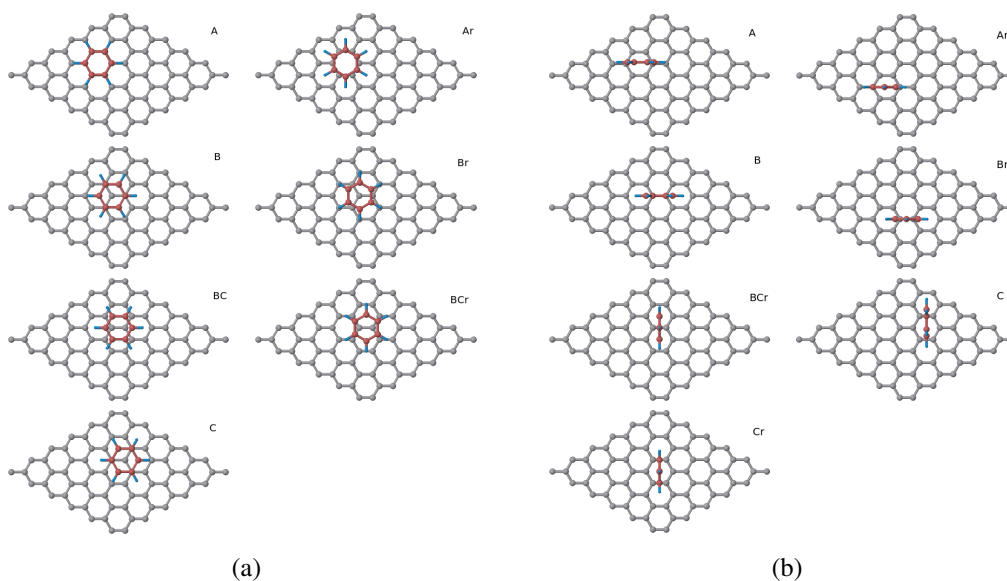


Figure 3.3: Different initial configurations for C_6H_6 on PG for parallel (a), and perpendicular adsorption (b).

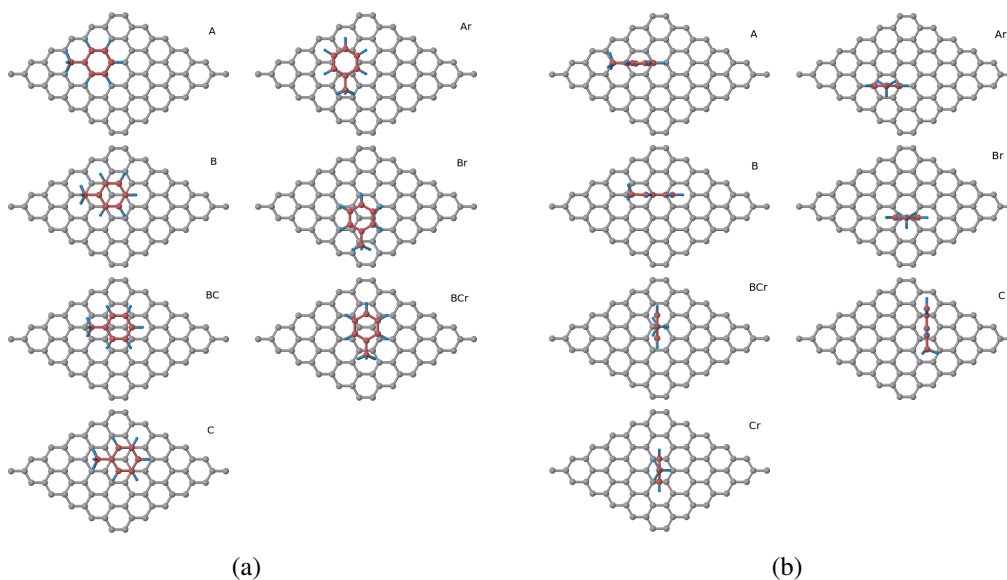


Figure 3.4: Different initial configurations for C_7H_8 on PG for parallel (a), and perpendicular adsorption (b).

The adsorption energies and graphene-molecule distances obtained from these configurations are listed in Table 3.1. During structural optimization, the organic molecules induce small degrees of curvature on the graphene layer where the degree of curvature is highest for vdW-DF. Thus, the adsorption height distances are taken as the vertical separation of the average value in the z-direction of C atoms in graphene and the H atom of the organic molecule closest to the graphene layer.

As observed from Table 3.1, the preferred geometry of C_6H_6 and C_7H_8 molecule on graphene is a parallel configuration for all exchange-correlation functionals. When the geometries with the highest adsorption energy are investigated, a general trend is deduced where the axial H atoms of the molecule facing the graphene layer are located on top of the centers of the empty hexagonal sites of the honeycomb lattice of graphene. The preferred geometries of C_6H_6 are labeled C for all exchange-correlation functionals (see Figure 3.3) while the preferred geometries of C_7H_8 are labeled C, C and B for vdW-DF, vdW-DF2-C09 and Grimme-D2, respectively. Moreover, it is observed that adsorption energies are very close to each other for some sites in parallel configuration.

In its optimized structure, C_6H_6 is located at a distance of 3.46 Å and the adsorption energy is 596 meV while C_7H_8 is located at a distance of 3.13 Å and the adsorption energy is 689 meV for vdW-DF. The adsorption distance of C_6H_6 is 3.30 Å with 441 meV and 3.21 Å with 524 meV for vdW-DF2-C09 and Grimme-D2, respectively while the adsorption distance of C_7H_8 is 2.93 Å with 498 meV and 2.74 Å with 593 meV for vdW-DF2-C09 and Grimme-D2, respectively. These values are in good agreement with the previous theoretical and experimental results [20, 186, 197].

The top view and the side view of the optimized geometries with the highest adsorption energies tabulated in Table 3.1 are presented with their band structures in Figure 3.5 and Figure 3.6 for C_6H_6 and C_7H_8 , respectively. The band structure for the non-covalent interaction of C_6H_6 and C_7H_8 with PG reveal no deviation around the K-point from PG's band structure.

In order to separate the contribution of states coming from the adsorbate and the substrate, we present the results of a partial density of states (PDOS) analysis in Figures 3.7 and 3.8.

Table 3.1: The adsorption energies and distances of C_6H_6 and C_7H_8 on PG at different sites.

		Parallel				Perpendicular							
		vdW-DF		vdW-DF2-C09		Grimme-D2		vdW-DF		vdW-DF2-C09		Grimme-D2	
site	d [Å]	E [meV]	d [Å]	E [meV]	d [Å]	E [meV]	site	d [Å]	E [meV]	d [Å]	E [meV]	d [Å]	E [meV]
C_6H_6													
A	3.39	576	3.46	416	3.28	463	A	2.77	359	2.62	240	2.61	315
Ar	3.53	579	3.46	420	3.26	469	Ar	2.57	348	2.57	237	2.57	288
B	3.44	595	3.31	440	3.17	523	B	2.73	360	2.61	245	2.61	320
Br	3.43	594	3.27	437	3.19	518	Br	2.60	339	2.60	230	2.60	278
BC	3.55	594	3.32	436	3.21	514	BCr	2.64	363	2.62	226	2.62	274
BCr	3.51	593	3.29	432	3.21	512	C	2.75	363	2.61	246	2.61	323
C	3.46	596	3.30	441	3.21	524	Cr	2.61	347	2.62	236	2.62	283
C_7H_8													
A	3.21	668	2.95	456	2.83	527	A	2.67	387	2.42	253	2.62	316
Ar	3.24	669	3.00	458	2.86	534	Ar	2.85	285	2.81	176	2.70	250
B	3.15	688	2.93	498	2.74	593	B	2.76	390	2.63	248	2.61	322
Br	3.03	672	3.00	497	2.61	590	Br	4.42	181	3.10	198	4.41	130
BC	3.20	685	2.95	487	2.93	581	BCr	3.08	304	3.03	201	2.75	245
BCr	3.22	687	2.92	492	2.65	583	C	3.56	285	3.58	176	3.58	195
C	3.13	689	2.93	497	2.63	591	Cr	3.02	286	2.84	176	2.74	251

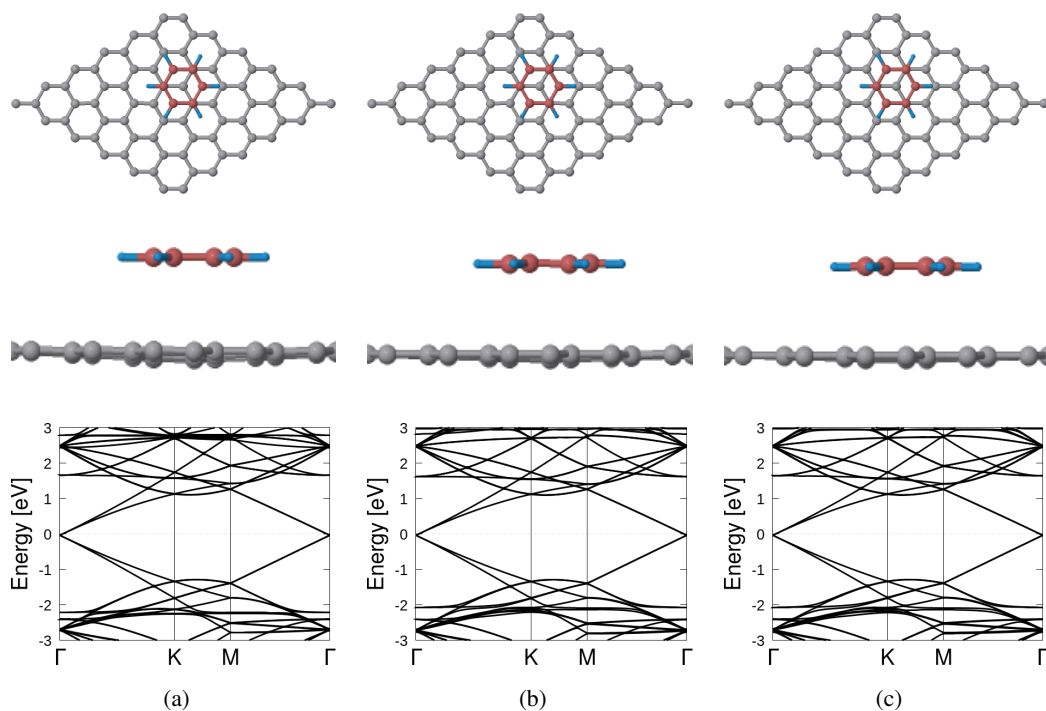


Figure 3.5: The top view, the side view and the band structure of C_6H_6 on PG for vdW-DF (a), vdW-DF2-C09 (b), and Grimme-D2 (c).

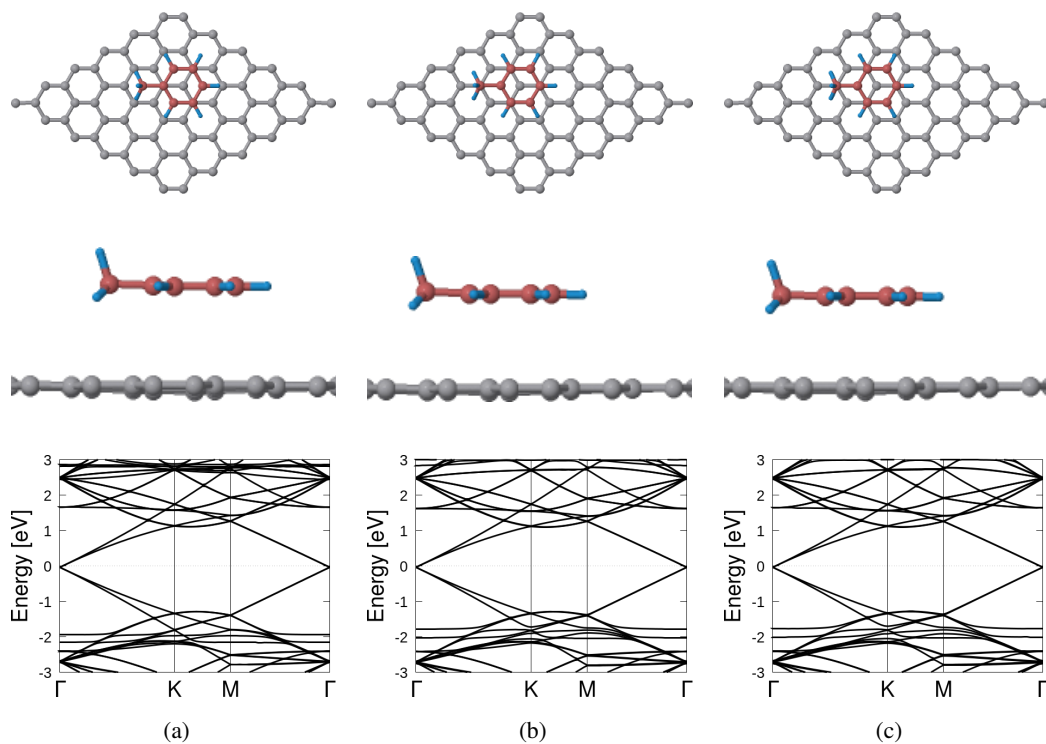


Figure 3.6: The top view, the side view and the band structure of C_7H_8 on PG for vdW-DF (a), vdW-DF2-C09 (b), and Grimme-D2 (c).

In order to understand the effect of the adsorption on charge distribution, charge density difference calculations are performed for those geometries with the highest adsorption energy and plots are presented in Figure 3.7 and Figure 3.8 for C_6H_6 and C_7H_8 , respectively. In these plots, red color represents regions with charge depletion while blue color represents those with charge accumulation. From the Bader charge analysis, the charge transfer between the substrate and the molecule is calculated to be negligibly small for the physisorbed species. C_6H_6 donates a charge of 0.007 e to the graphene network while donation is 0.013 e for C_7H_8 when vdW-DF2-C09 is employed.

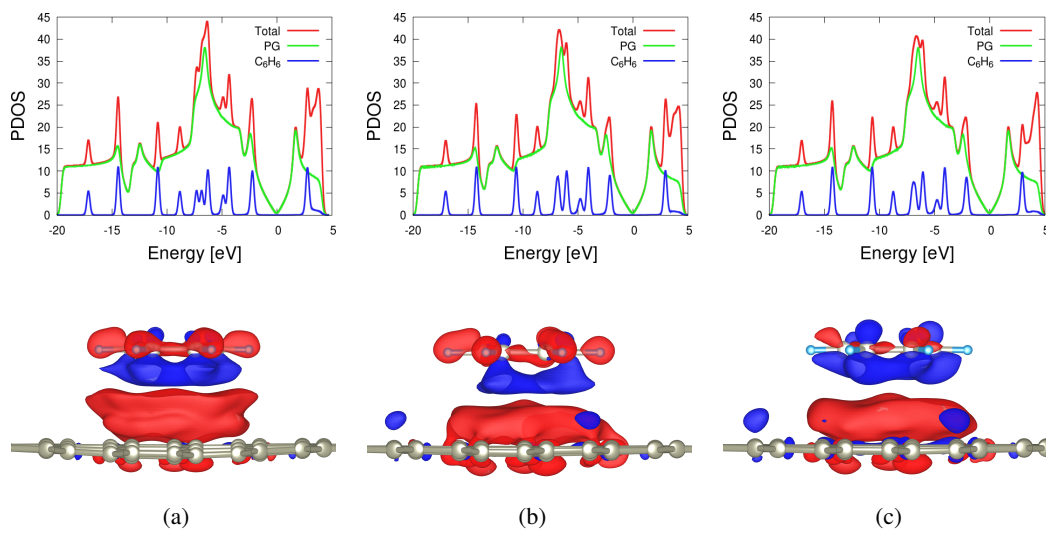


Figure 3.7: PDOS and charge density plot of C_6H_6 on PG for vdW-DF (a), vdW-DF2-C09 (b), and Grimme-D2 (c). The isovalue is set to $\pm 0.00011 \text{ \AA}^{-3}$.

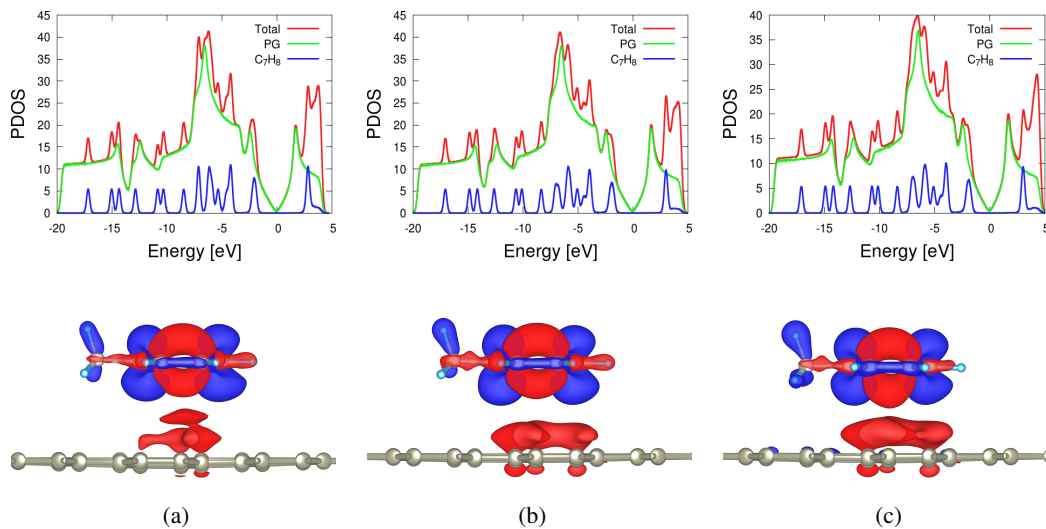


Figure 3.8: PDOS and charge density plot of C_7H_8 on PG for vdW-DF (a), vdW-DF2-C09 (b), and Grimme-D2 (c). The isovalue is set to $\pm 0.0003 \text{ \AA}^{-3}$.

The charge density difference plots shown in Figure 3.7 indicate a small amount of charge transfer between the π -systems of both C_6H_6 and graphene and the other orbitals. This seems to introduce a small dipole moment pointing away from graphene and towards C_6H_6 in the interface. Interestingly, the charge rearrangement profile of C_6H_6 appears somewhat different for Grimme-D2 than it does for the other two vdW protocols.

The charge transfer upon adsorption in the case of C_7H_8 is somewhat different when compared to that of C_6H_6 . The positively charge region immediately below the molecule is absent although the charge depleted region above graphene is still visible. The axial H molecules are still depleted while those belonging to the CH_3 group have acquired a small amount of positive charge.

3.2.1.1 Unoccupied States in PDOS Plots

As indicated in Chapter 2, PDOS calculations are performed in order to analyze the charge transfer. The QE package [143] provides a parameter by the name of as degauss symbolizing Gaussian broadening in Ry which defines the sharpness of peaks in the PDOS plot. By examining the sharpness of peaks for PDOS plot of C_6H_6 adsorption on PG with vdW-DF2-C09, a benchmark study has been done in order to determine degauss value to be used during the production calculations. For this purpose, 3 different degauss values are studied namely 0.01, 0.015 and 0.02 Ry.

The peaks in Figure 3.9a are very sharp with 0.01 Ry Gaussian broadening and oscillations take place in the PDOS plot of pristine graphene while peaks become wider by increasing Gaussian broadening. Upon analysis of Figure 3.9b and Figure 3.9c, 0.015 Ry Gaussian broadening was seen to give optimal results and was preferred during calculations.

On the other hand, it is observed that summation of C_6H_6 states and PG states does not give the total DOS for unoccupied states in Figure 3.9b since the effect of unoccupied d and f-orbitals have been ignored in the pseudopotential used for C. In order to include the effect of unoccupied d and f-orbitals to the PDOS plot, calculations have been repeated for C_6H_6 adsorption on PG with a different pseudopotential

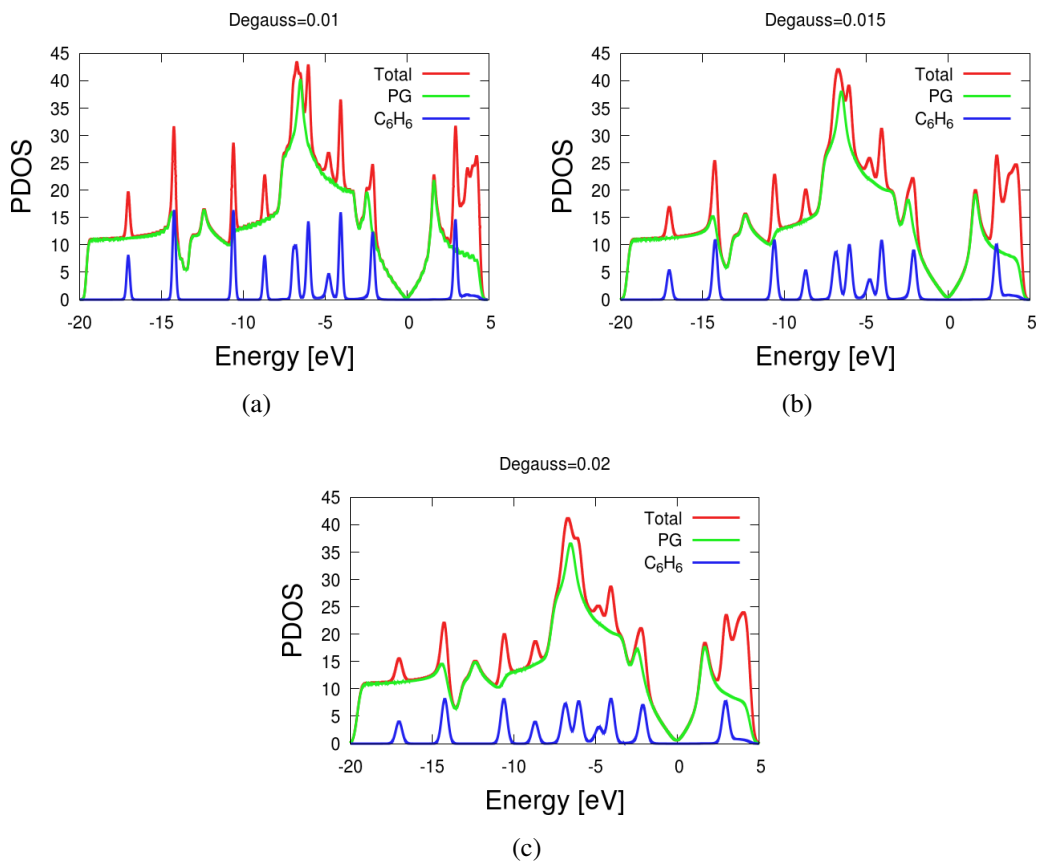


Figure 3.9: The benchmark study for Gaussian broadening value: (a) 0.01 Ry, (b) 0.015 Ry, and (c) 0.02 Ry.

containing contributions from the d- and f-orbital. While including d- and f-orbital configurations appears to fix this problem (Figure 3.10), we continue to use the former pseudopotential excluding these contributions as the effect is largely confined to the unoccupied states.

3.2.2 Organic Molecules on Vacancy-Defected Graphene

A 6x6 unit cell of VG consisting of 71 atoms is used as adsorbent for the calculations in this section. C_6H_6 and C_7H_8 are adsorbed on defective graphene, separately. 5 different configurations for C_6H_6 and 7 different configurations for C_7H_8 are considered, all in the vicinity of the defect and all in the parallel configuration. These configurations are displayed in Figure 3.11a and Figure 3.11b, respectively.

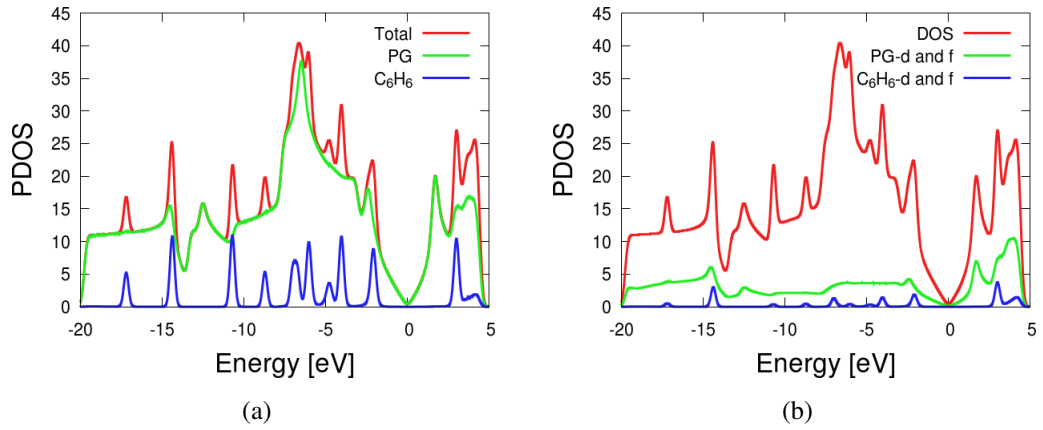


Figure 3.10: PDOS plot of C_6H_6 on PG (a), and d and f-states of C_6H_6 and PG including DOS (b).

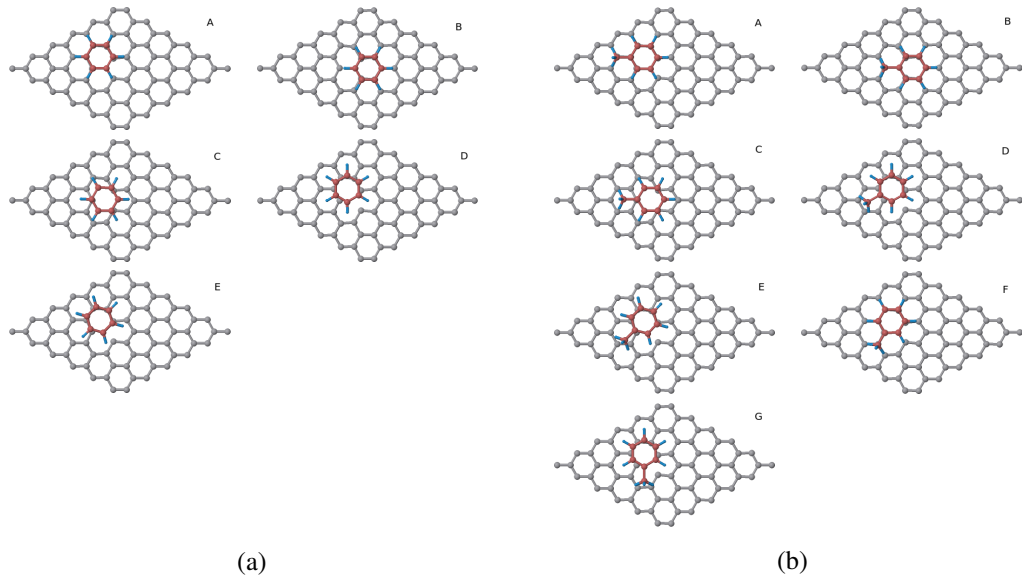


Figure 3.11: The different initial configurations for C_6H_6 (a) and C_7H_8 (b) on VG.

As some graphene point defects are expected to be magnetic (indicated in Section 2.3.2), spin polarization is activated in all calculations conducted in this section. After optimization calculations, it is observed that total magnetization of the VG/ C_6H_6 system is equal to $0.69 \mu_B$, $1.27 \mu_B$ and $1.40 \mu_B$ per cell for spin-polarized vdW-DF, vdW-DF2-C09 and Grimme-D2, respectively while total magnetization of C_7H_8 /VG is equal to $0.68 \mu_B$, $1.31 \mu_B$ and $1.45 \mu_B$ per cell for spin polarized vdW-DF, vdW-DF2-C09 and Grimme-D2, respectively. Previous calculations conducted on the graphene vacancy defect yields a total magnetization of about $1.43 \mu_B$. Considering the weak interaction between the substrate and the adsorbate, we do not expect

this value to change significantly upon adsorption. This result can be considered a further and interesting indication of the shortcomings of the vdW-DF scheme for the problem at hand.

The adsorption energies obtained from these configurations are listed in Table 3.2. Similar to the adsorption of organic molecules on PG, C_6H_6 and C_7H_8 induce small degrees of curvatures on VG while one of the C atoms surrounding the vacancy is distorted in the opposite direction of curvature formation and the degree of curvature is highest for vdW-DF as seen from the side view displayed in Figure 3.12 and Figure 3.14 for C_6H_6 and C_7H_8 , respectively. In the spin-polarized case, the distortion of all C atoms around the vacancy is in the same direction as the curvature formation as presented in Figure 3.13 and Figure 3.15 for C_6H_6 and C_7H_8 , respectively.

In the optimized structure, C_6H_6 has the highest adsorption energy with a value of 555 meV, 391 meV and 435 meV while C_7H_8 has the highest adsorption energy with a value of 607 meV, 425 meV and 482 meV for vdW-DF, vdW-DF2-C09 and Grimme-D2, respectively. For spin-polarized cases, the highest adsorption is calculated to be 596 meV for C_6H_6 with vdW-DF and for C_7H_8 , it is 678 meV with the same functional. As apparent from Table 3.2, sites with the highest adsorption energy changes not only with the change of exchange-correlation functional but also with inclusion of spin-polarization.

Similar to the adsorption on PG (Figure 3.5 and Figure 3.6), the band structure for the non-covalent interaction of C_6H_6 and C_7H_8 on VG reveal no deviation around the K-point from defective graphene's band structure as shown in Figure 3.12 and Figure 3.14. For the band structure of spin-polarized cases, red lines represent the majority spin while blue lines represent the minority spin in Figure 3.13 and Figure 3.15 for C_6H_6 and C_7H_8 , respectively, and it is observed that spin polarization lifts the degeneracies while the Fermi level is depressed below the original location.

Table 3.2: The adsorption energies of C_6H_6 and C_7H_8 on VG at different sites.

	vdW-DF	spin-polarized vdW-DF	vdW-DF2-C09	spin-polarized vdW-DF2-C09	Grimme-D2	spin-polarized Grimme-D2	
site	E [meV]	E [meV]	E [meV]	E [meV]	E [meV]	E [meV]	
C_6H_6	A	507	594	356	399	394	445
	B	555	586	391	397	435	445
	C	510	562	373	401	417	454
	D	507	596	360	405	399	451
	E	506	594	358	401	395	448
C_7H_8	A	576	671	390	431	443	504
	B	607	638	416	433	469	500
	C	588	643	425	444	482	518
	D	574	658	392	438	446	506
	E	573	677	391	435	442	508
	F	575	678	392	439	440	505
	G	586	670	402	445	452	507

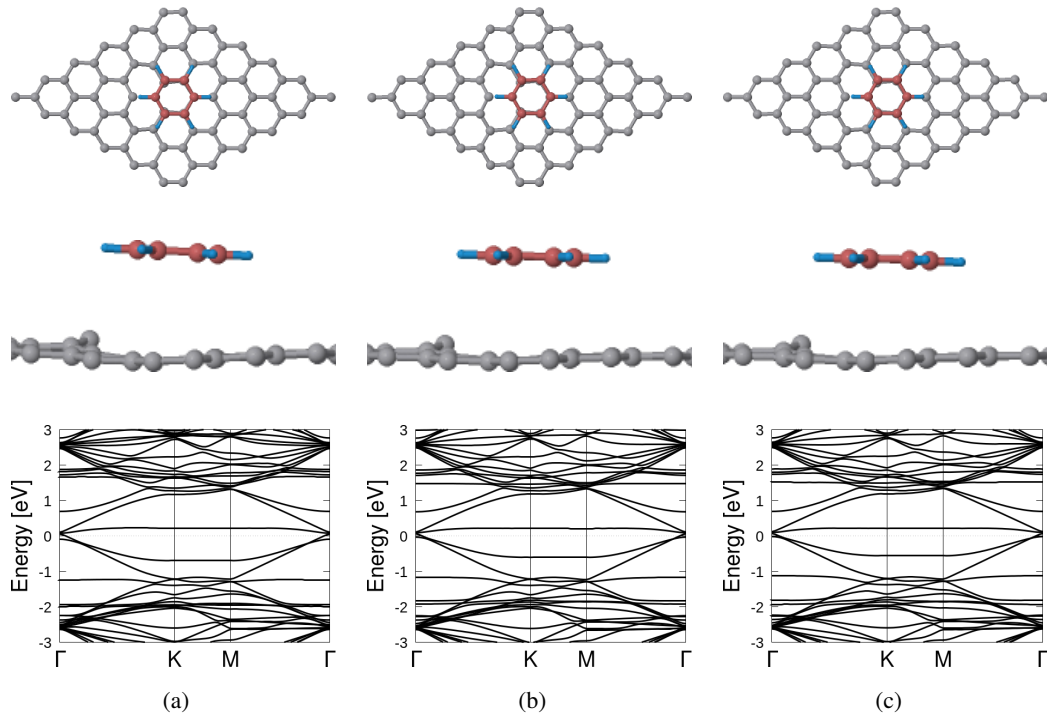


Figure 3.12: The top view, the side view and the band structure of C₆H₆ on spin-polarized VG for vdW-DF (a), vdW-DF2-C09 (b), and Grimme-D2 (c).

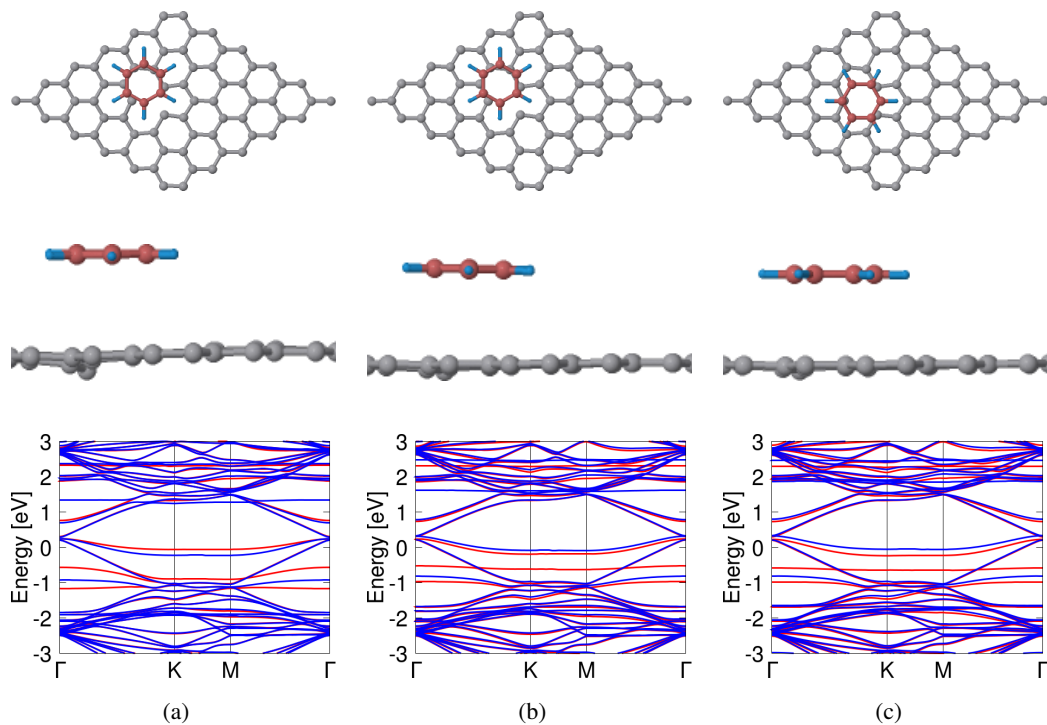


Figure 3.13: The top view, the side view and the band structure of C₆H₆ on spin-polarized VG for vdW-DF (a), vdW-DF2-C09 (b), and Grimme-D2 (c).

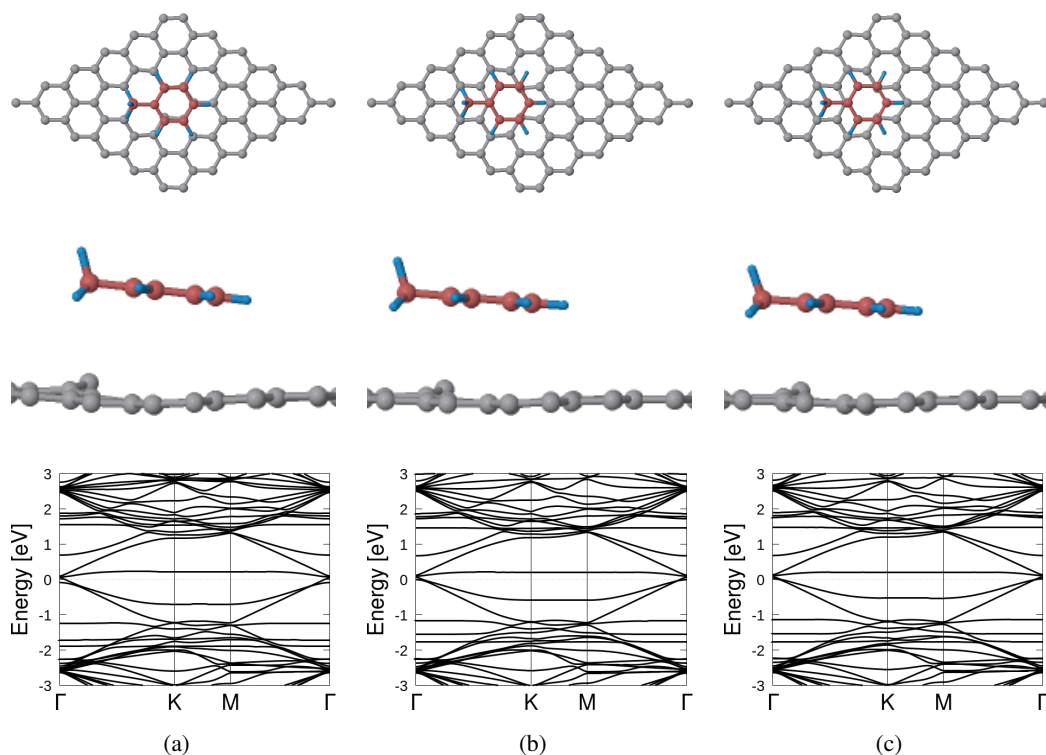


Figure 3.14: The top view, the side view and the band structure of C_7H_8 on spin-polarized VG for vdW-DF (a), vdW-DF2-C09 (b), and Grimme-D2 (c).

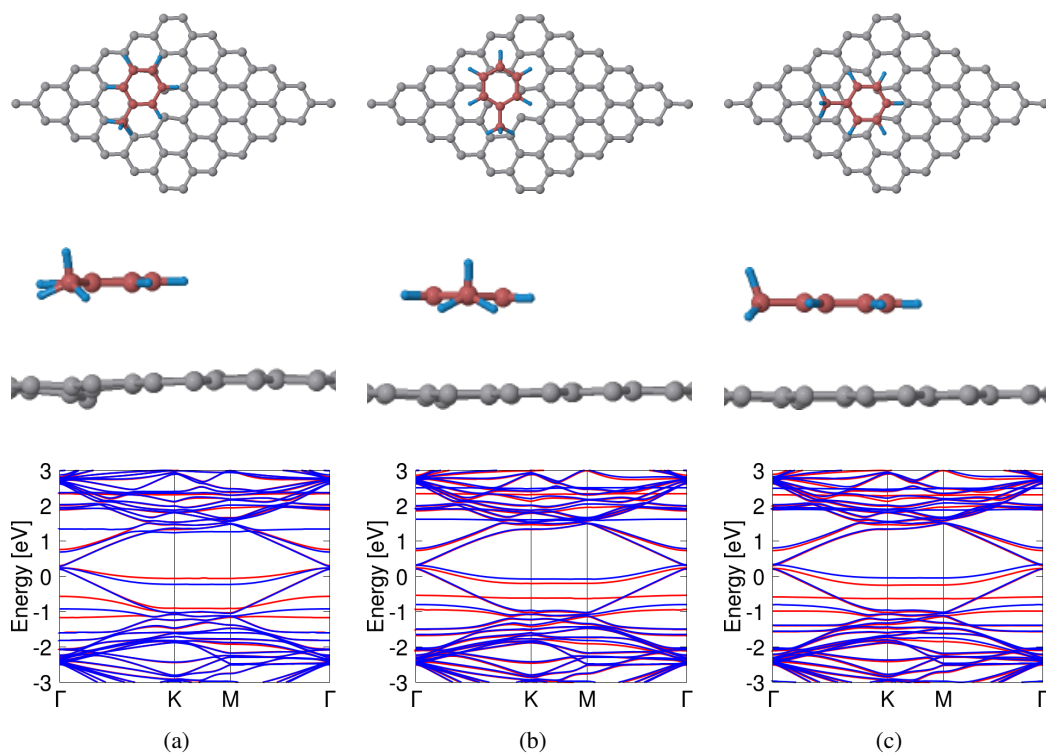


Figure 3.15: The top view, the side view and the band structure of C_7H_8 on spin-polarized VG for vdW-DF (a), vdW-DF2-C09 (b), and Grimme-D2 (c).

PDOS and charge density difference plots for C_6H_6 and C_7H_8 are displayed in Figure 3.16 and Figure 3.18 while the plots for calculations including spin-polarization are presented in Figure 3.17 and Figure 3.19 for C_6H_6 and C_7H_8 , respectively where red color represents charge depletion while blue color represents charge accumulation. The rearrangement of charge in the case of the monovacancy is rather different from that of defect-free graphene. In this case, the portions of the molecule that is closer to the elevated atom has lost some electrons to both its own π orbitals and the lone atom. Although there are still remnants of the interface transfer familiar from PG, the charge transfer is decidedly asymmetric. There is 0.007 e donation from C_6H_6 to VG while 0.011 e is transferred from C_7H_8 to VG when vdW-DF2-C09 is employed.

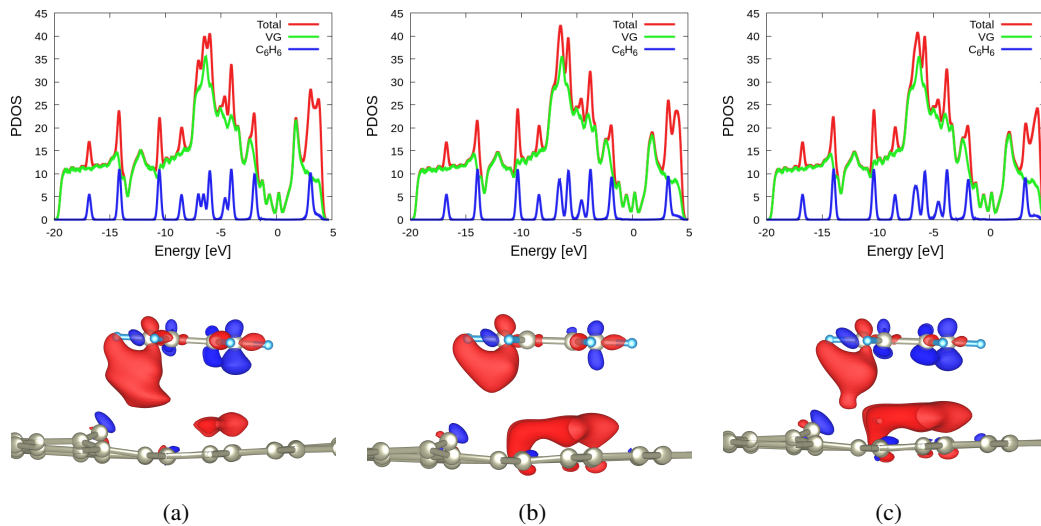


Figure 3.16: PDOS and charge density plots of C_6H_6 on VG for spin-unpolarized vdW-DF (a), vdW-DF2-C09 (b), and Grimme-D2 (c). The isovalue is set to $\pm 0.00029 \text{ \AA}^{-3}$.

3.2.3 Organic Molecules on Divacancy-Defected Graphene

A 6×6 unit cell of graphene was used with two neighboring C atoms missing to model the divacancy defected graphene in this section. C_6H_6 and C_7H_8 are adsorbed on DG, separately. Similarly to the previous section (Section 3.2.2), 5 different configurations for C_6H_6 and 7 different configurations for C_7H_8 are formed around the defect as parallel adsorption of organic molecules on defective graphene which are shown in Figure 3.20.

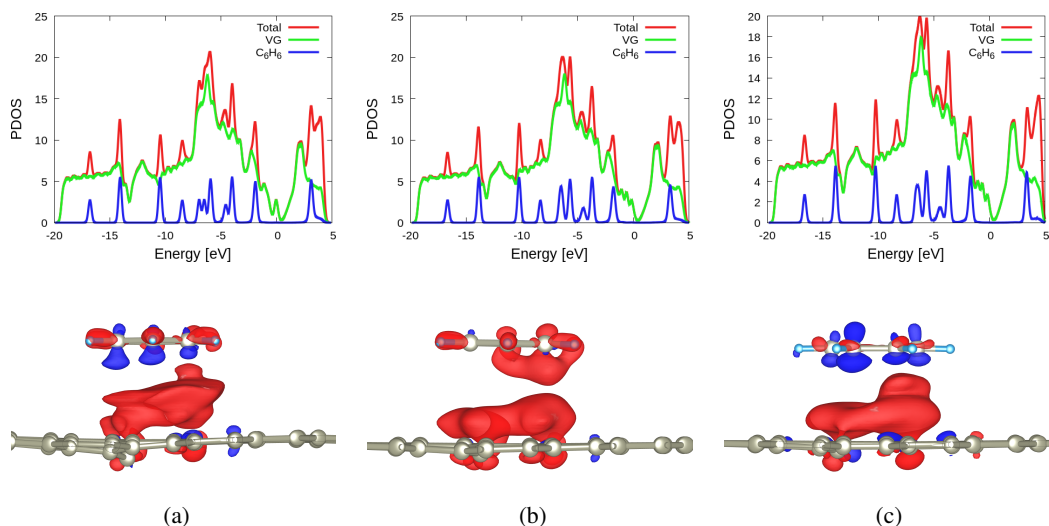


Figure 3.17: PDOS and charge density plots of C_6H_6 on VG for spin-polarized vdW-DF (a), vdW-DF2-C09 (b), and Grimme-D2 (c). The isovalue is set to $\pm 0.0002 \text{ \AA}^{-3}$.

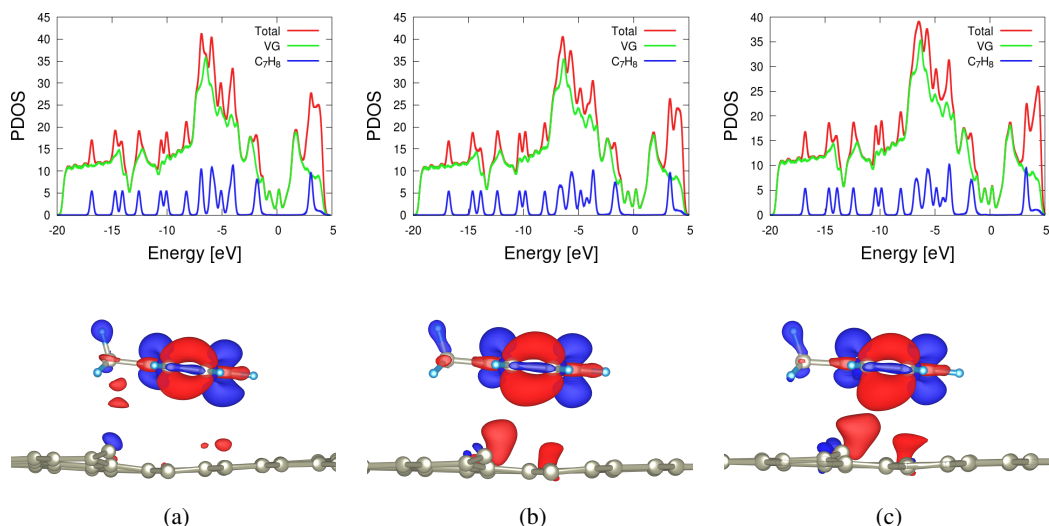


Figure 3.18: PDOS and charge density plots of C_7H_8 on VG for spin-unpolarized vdW-DF (a), vdW-DF2-C09 (b), and Grimme-D2 (c). The isovalue is set to $\pm 0.00042 \text{ \AA}^{-3}$.

The adsorption energies obtained from these configurations are listed in Table 3.3. Similar to the adsorption geometry of organic molecules on PG, DG has a negligible degree of curvature which can be taken into account as almost planar geometry without any distortion of the atoms surrounding the defect.

In the optimized structure, C_6H_6 has the most stable configuration with an adsorption energy of 576 meV, 404 meV and 452 meV while these values for C_7H_8 are 651 meV, 448 meV and 518 meV for vdW-DF, vdW-DF2-C09 and Grimme-D2, respectively. As seen from Table 3.2, the sites with the highest adsorption energy does not change with

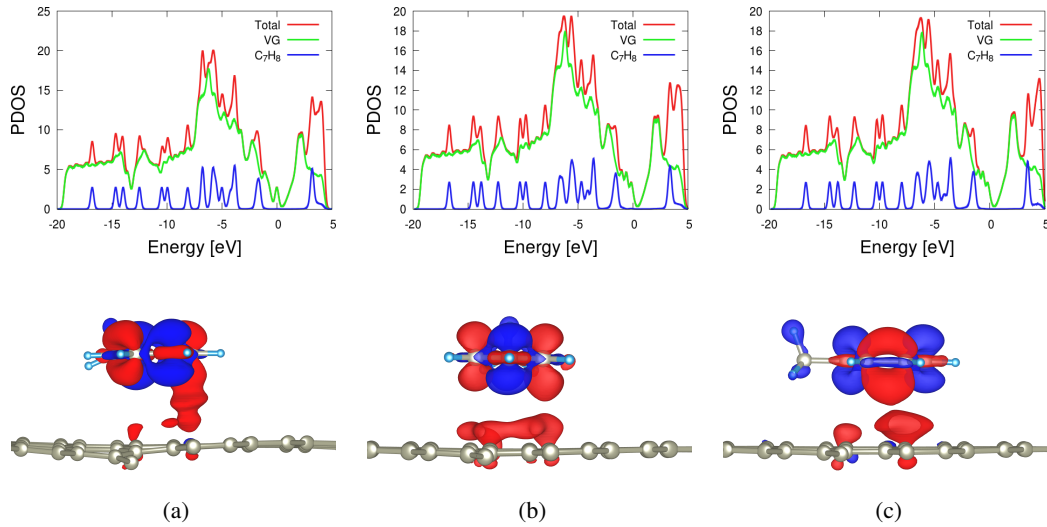


Figure 3.19: PDOS and charge density plots of C_7H_8 on VG for spin-polarized vdW-DF (a), vdW-DF2-C09 (b), and Grimme-D2 (c). The isovalue is set to $\pm 0.0004 \text{ \AA}^{-3}$.

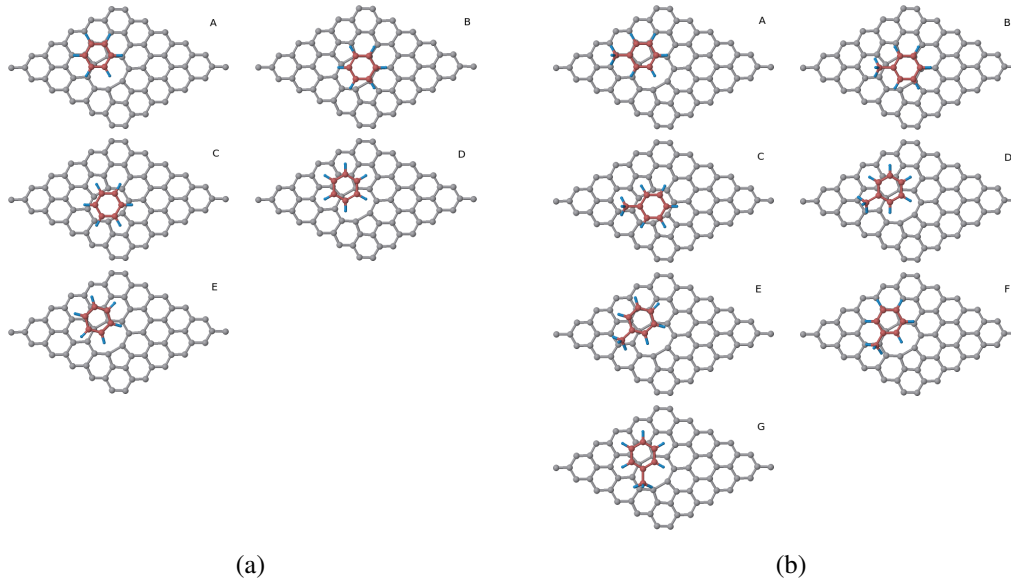


Figure 3.20: The different initial configurations for C_6H_6 and C_7H_8 on DG.

the change of exchange-correlation functional.

The band structures for the molecule/DG systems reveal no deviation around the K-point from the band structure of graphene with a divacancy as seen in Figure 3.21 and Figure 3.22 for C_6H_6 and C_7H_8 , respectively. PDOS and charge density difference plots for C_6H_6 and C_7H_8 are shown in Figure 3.23 and Figure 3.24. As consistent with PDOS plots, additional states from the molecules only fall on the conduction

Table 3.3: The adsorption energies of C_6H_6 and C_7H_8 on DG at different sites.

		vdW-DF	vdW-DF2-C09	Grimme-D2
site		E [meV]	E [meV]	E [meV]
C_6H_6	A	575	401	450
	B	564	400	447
	C	553	382	426
	D	576	404	452
	E	575	401	451
C_7H_8	A	649	440	512
	B	641	445	512
	C	630	428	496
	D	650	444	516
	E	650	444	516
	F	651	448	518
	G	647	447	513

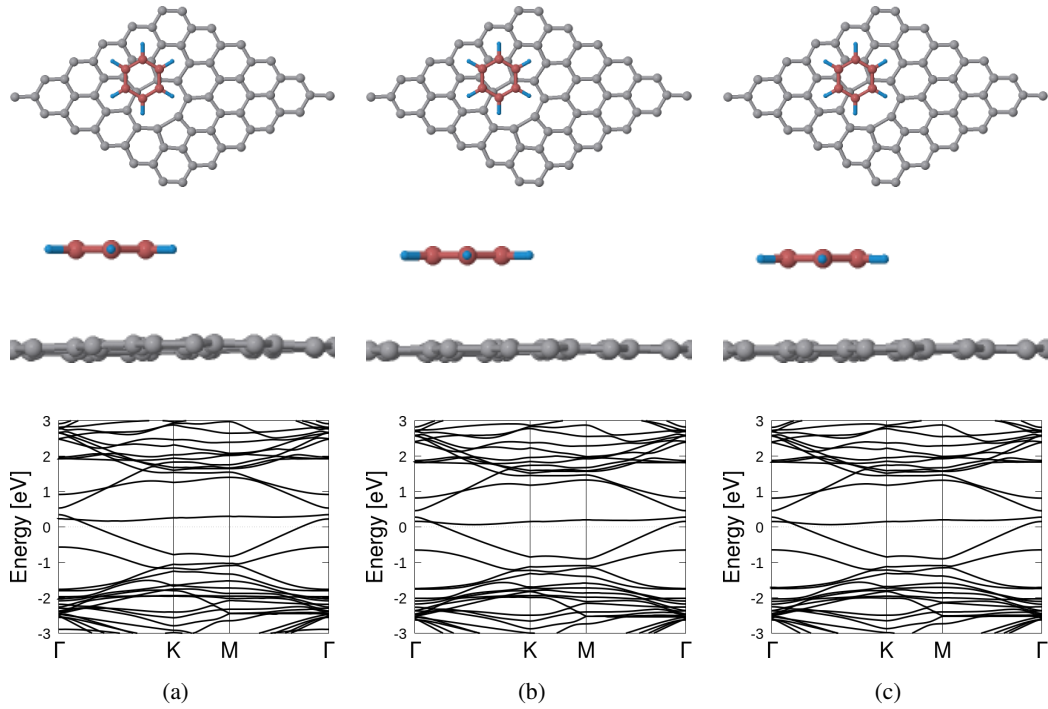


Figure 3.21: The top view, the side view and the band structure of C_6H_6 on DG for vdW-DF (a), vdW-DF2-C09 (b), and Grimme-D2 (c).

and valence bands. The charge transfer upon adsorption is once again reminiscent of the PG case where there seems to be a small dipole moment induced in the interface region that points from the molecule to the substrate. Bader charge analysis shows

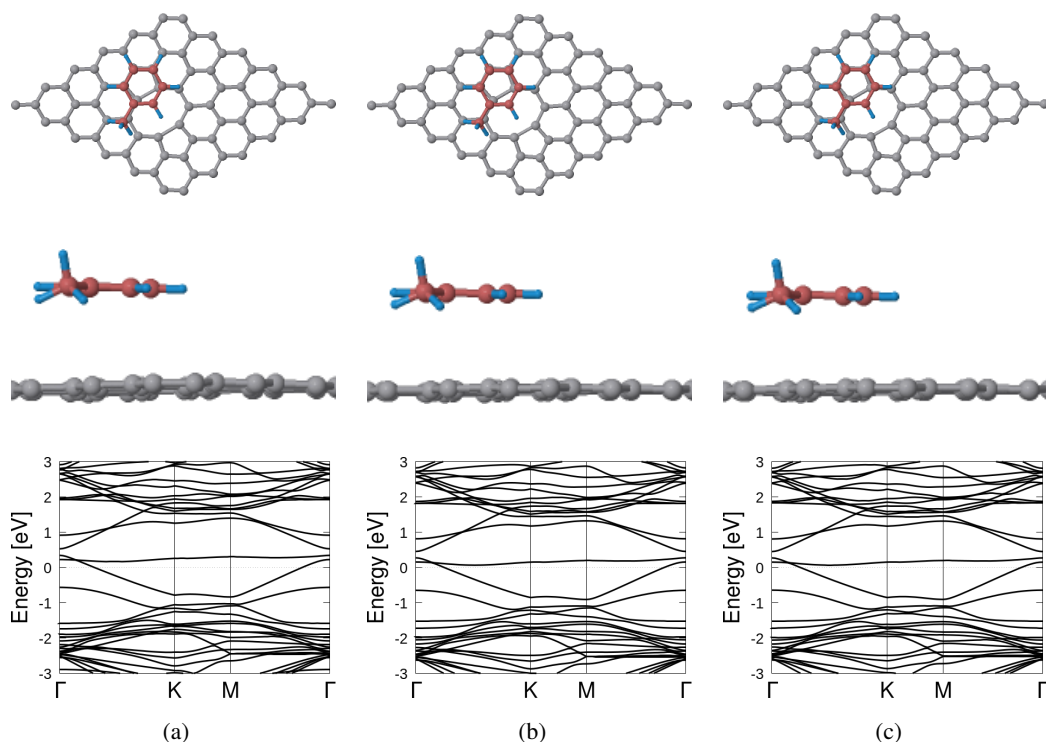


Figure 3.22: The top view, the side view and the band structure of C_7H_8 on DG for vdW-DF (a), vdW-DF2-C09 (b), and Grimme-D2 (c).

there is 0.019 e transfer from C_6H_6 to DG while 0.012 e is transferred from C_7H_8 to DG confirming the electron accepting characteristics of graphene-based surfaces.

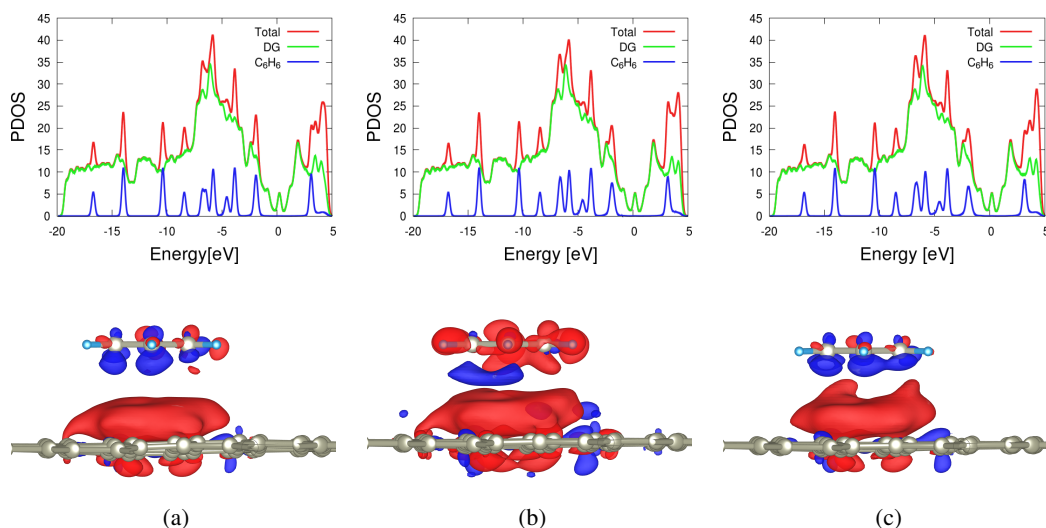


Figure 3.23: PDOS and charge density plots of C_6H_6 on DG for vdW-DF (a), vdW-DF2-C09 (b), and Grimme-D2 (c). The isovalue is set to $\pm 0.00019 \text{ \AA}^{-3}$.

There are numerous theoretical studies in literature on C_6H_6 adsorption on graphene while the experimental studies are still rare. In experimental studies, graphene is

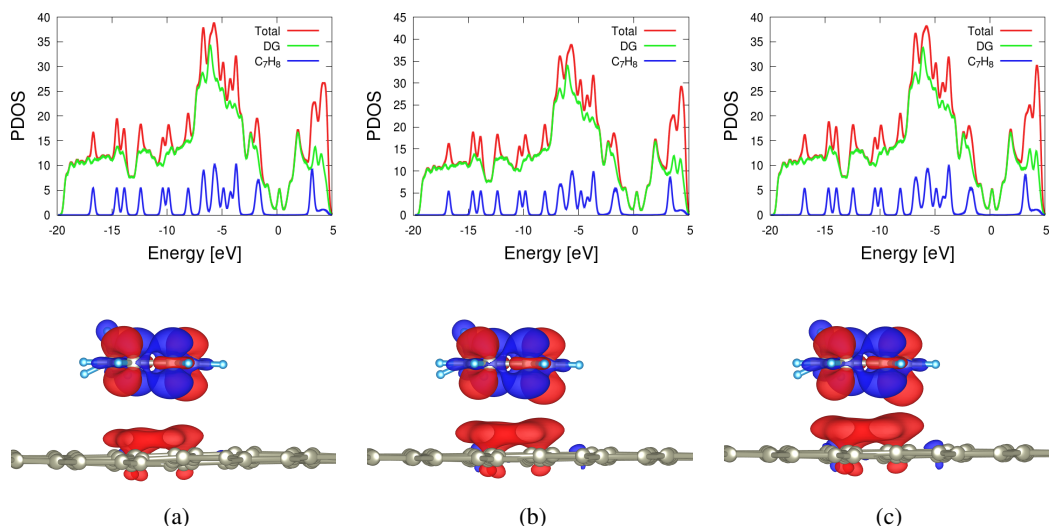


Figure 3.24: PDOS and charge density plots of C_7H_8 on DG for vdW-DF (a), vdW-DF2-C09 (b), and Grimme-D2 (c). The isovalue is set to $\pm 0.00035 \text{ \AA}^{-3}$.

grown continuously on both sides of the copper (Cu) surface, forming a crystalline single layer [8, 185, 198, 199]. In these experiments, adsorption energy is calculated for different coverages. It has been found that C_6H_6 adsorption characteristics on graphene is affected by the supports while the desorption energy for C_6H_6 adsorption on a graphene layer depends on the reactivity of the support. This, then, makes a direct comparison of theoretical and experimental results rather difficult. In spite of this difficulty, previous computational adsorption energy calculations and the experimental adsorption energy [20, 186, 188, 192, 194, 195] are found to be in agreement with our results.

When adsorption energy values are compared for organic molecules on pristine and defective graphene, it can be seen that the adsorption energy is highest for adsorption of species on PG. In addition to the change in adsorption energies, for vdW-DF2-C09 adsorption site with the highest adsorption energy changes with respect to the change of adsorbent. For instance, site C of C_6H_6 exhibits the highest adsorption energy of 441 meV on PG while the energy is 391 meV on VG for site B and 404 meV on DG for site D. In this case, adsorption energy is higher for the adsorption on divacancy than on vacancy.

3.3 Organic Molecules on Bilayer Graphene

In order to understand the effects of the number of graphene layers on adsorption characteristics, the adsorption of C_6H_6 and C_7H_8 on bilayer graphene has been investigated.

First, adsorption height calculations have been performed for the three exchange-correlation functionals with the methodology described in Section 3.2. Concerning the relative location of the two layers, AB stacking has been utilized since AB-stacked structure is more stable than the AA-stacked structure [200]. The adsorption energy curves with respect to different adsorption heights for three different exchange-correlation functionals are shown in Figure 3.25. The calculated adsorption heights are 3.64 Å, 3.29 Å and 3.23 Å for vdW-DF, vdW-DF2-C09 and Grimme-D2, respectively where the adsorption height is minimum with Grimme-D2 while it is maximum with vdW-DF. These adsorption heights are taken as the initial distance between two layers of graphene sheets in the following calculations.

C_6H_6 and C_7H_8 are adsorbed on top of bilayer graphene with the adsorption distance as calculated and presented in Section 3.2. Regarding the position of organic molecule, the geometry with the highest adsorption energy on single layer graphene (Section 3.2.1) have been used. The optimized geometries are shown in Figure 3.26 and Figure 3.27. The adsorption energy values are calculated from Equation 3.1 where $E_{graphene}$ is the energy of bilayer graphene sheet. With this definition, the adsorption energy values for vdW-DF2-C09 are 508 meV at a distance of 3.31 Å for C_6H_6 and 565 meV at a distance of 2.84 Å for C_6H_6 on bilayer graphene where a pristine graphene layer is on top of another pristine graphene layer (PP).

Organic molecules induce small degrees of curvatures on the layers of graphene layer as also observed in Section 3.2.1. However, the distortion remains largely confined to the first layer.

Furthermore, organic molecules are adsorbed on top of bilayer graphene where the top layer of the bilayer has a single vacancy. The adsorption geometry is chosen to be the one with the highest adsorption energy on VG (Section 3.2.2). In the rest of this section, we will refer to the bilayer as PV, signifying the presence of a pristine layer

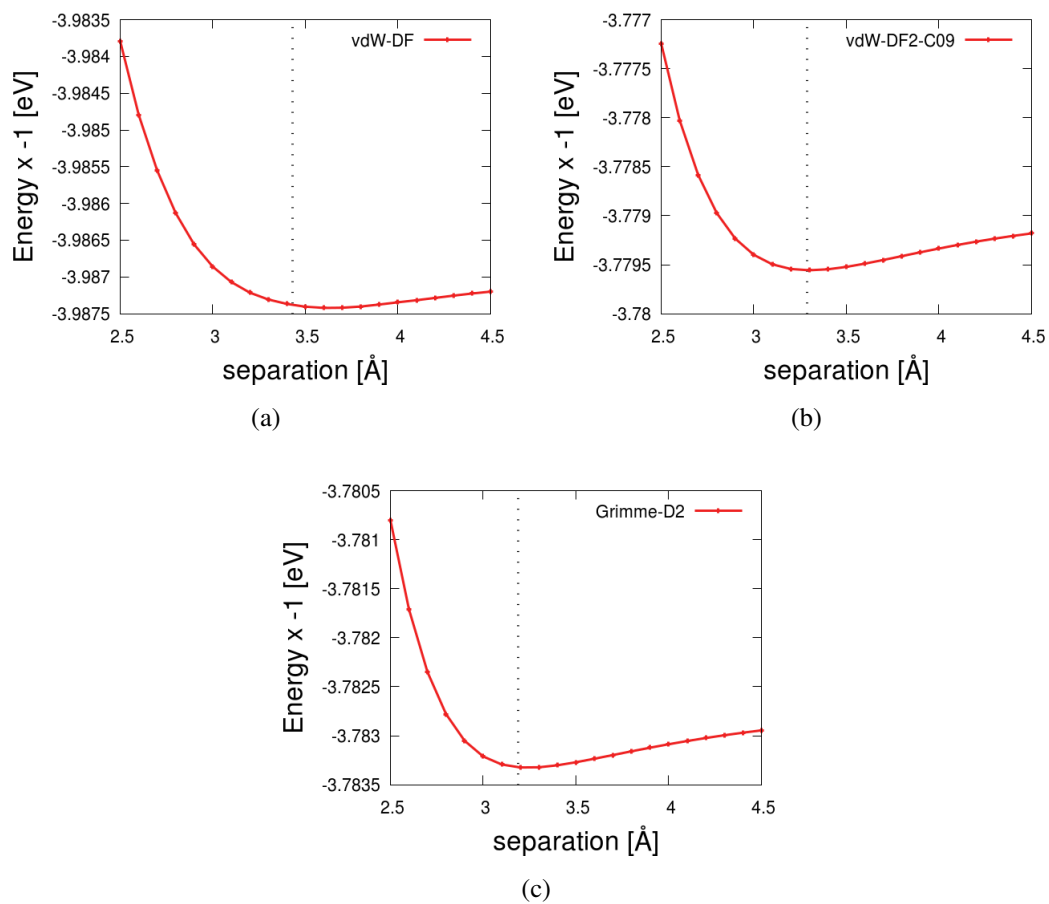


Figure 3.25: The adsorption energy curve of bilayer graphene with vdW-DF (a), vdW-DF2-C09 (b), and Grimme-D2 (c).

together with a layer with a single vacancy.

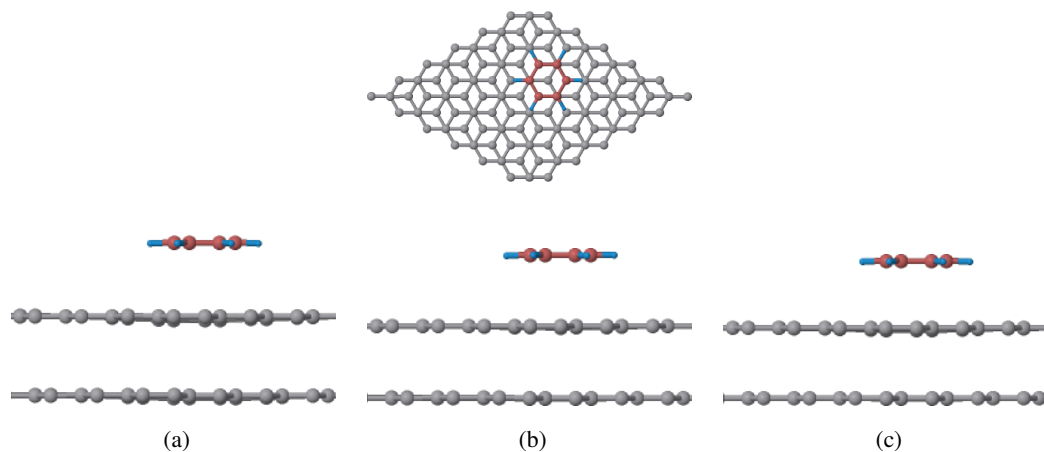


Figure 3.26: The top view and the side view for optimized geometries of C_6H_6 on PP for vdW-DF (a), vdW-DF2-C09 (b), and Grimme-D2 (c).

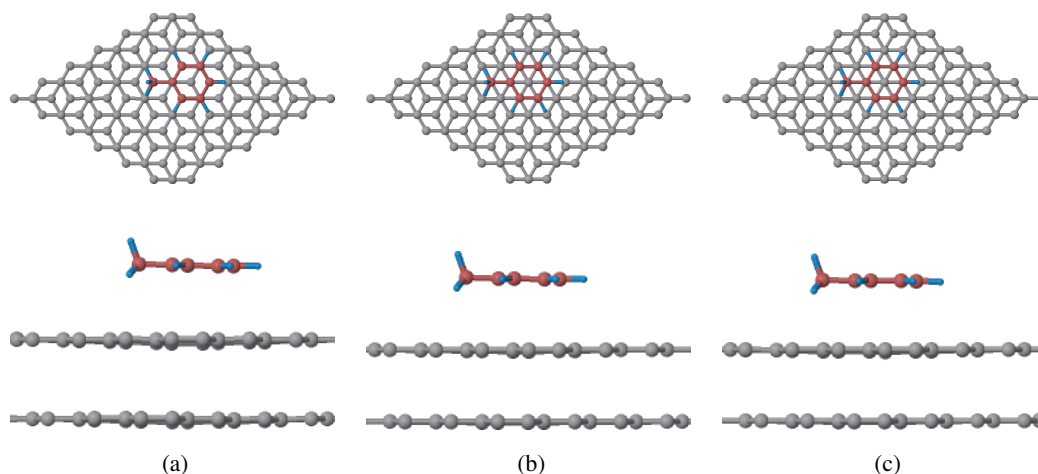


Figure 3.27: The top view and the side view for optimized geometries of C_7H_8 on PP for vdW-DF (a), vdW-DF2-C09 (b), and Grimme-D2 (c).

The optimized geometries are shown in Figure 3.28 and Figure 3.30 and the adsorption energy values for vdW-DF2-C09 are 432 meV at a distance of 3.57 Å for C_6H_6 and 486 meV at a distance of 3.12 Å for C_7H_8 . For spin-polarized calculations, the adsorption energy values are calculated to be 462 meV at a distance of 3.28 Å for C_6H_6 and 331 meV at a distance of 3.32 Å for C_7H_8 while their optimized geometries are shown in Figure 3.29 and Figure 3.31 for C_6H_6 and C_7H_8 , respectively. The calculated spin magnetization is $1.24 \mu_B$ and $1.27 \mu_B$ per cell for C_6H_6 and C_7H_8 , respectively while spin magnetization is $1.34 \mu_B$ per cell for PV. Interestingly, the magnetization value is seen to decrease slightly upon adsorption of the molecule.

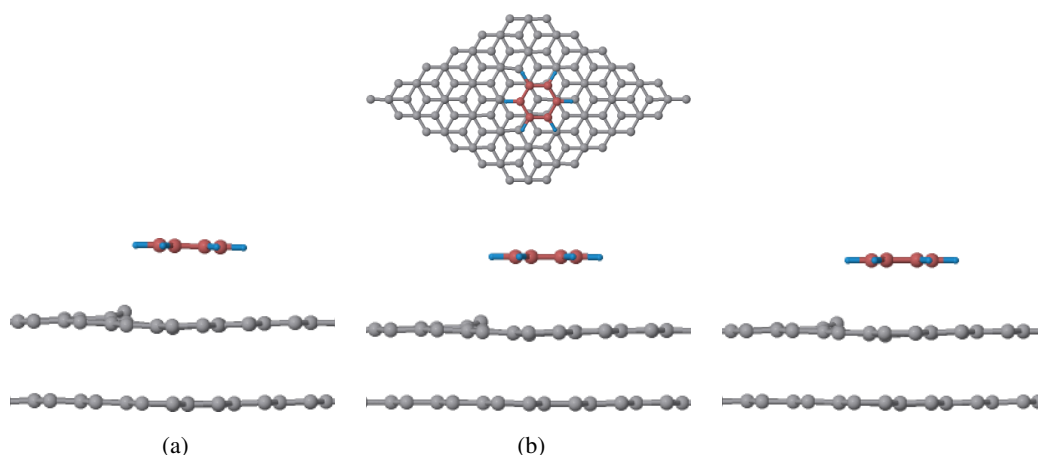


Figure 3.28: The top view and the side view for optimized geometries of spin-unpolarized C_6H_6 on PV for vdW-DF (a), vdW-DF2-C09 (b), and Grimme-D2 (c).

As another group of calculations, organic molecules are adsorbed on top of bilayer graphene where the top layer of the bilayer has a divacancy. The adsorption geometry

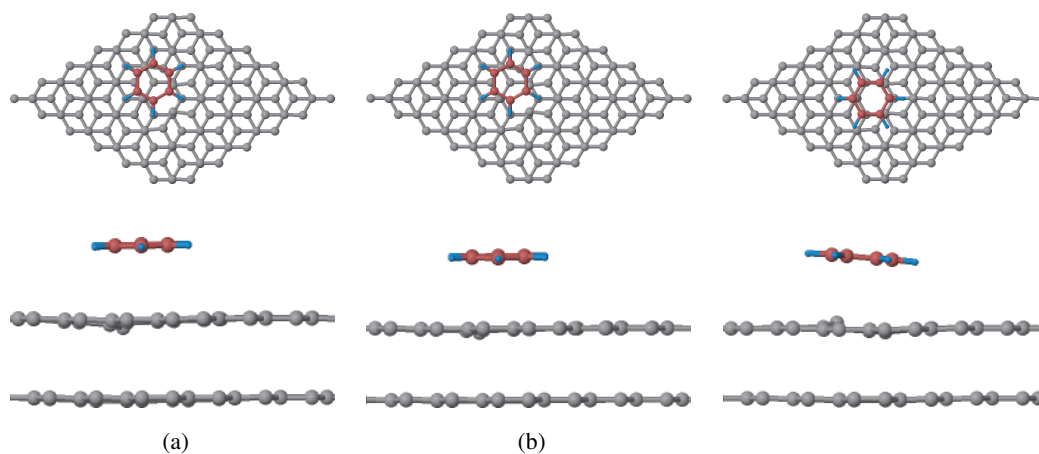


Figure 3.29: The top view and the side view for optimized geometries of spin-polarized C_6H_6 on PV for vdW-DF (a), vdW-DF2-C09 (b), and Grimme-D2 (c).

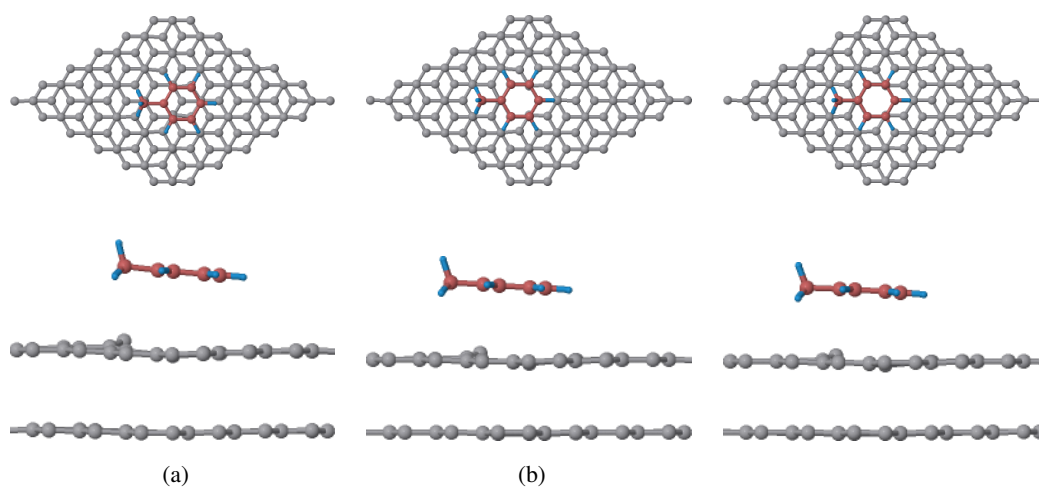


Figure 3.30: The top view and the side view for optimized geometries of spin-unpolarized C_7H_8 on PV for vdW-DF (a), vdW-DF2-C09 (b), and Grimme-D2 (c).

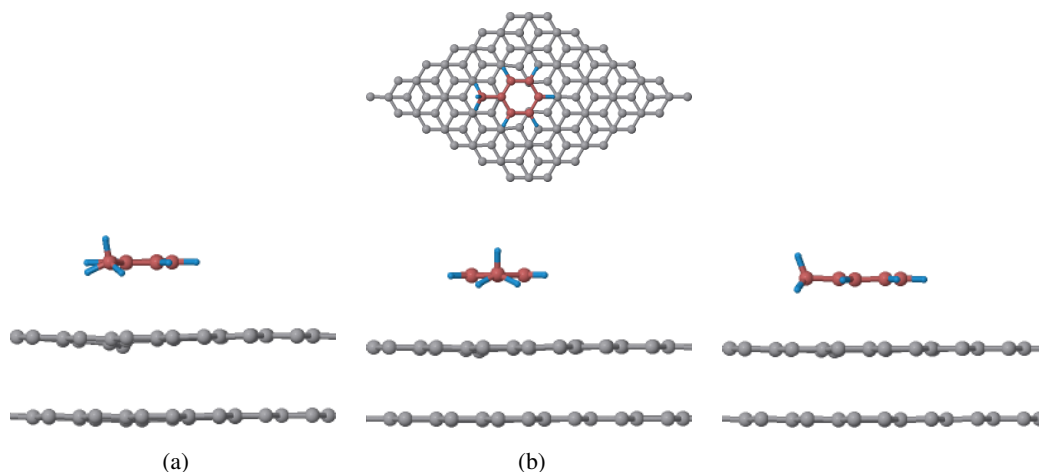


Figure 3.31: The top view and the side view for optimized geometries of spin-polarized C_7H_8 on PV for vdW-DF (a), vdW-DF2-C09 (b), and Grimme-D2 (c).

is chosen to be the one with the highest on DG (Section 3.2.3). In the rest of this section, we will refer to the bilayer as PD, signifying the presence of a pristine layer together with a layer with a divacancy.

The optimized geometries obtained after optimization calculations are shown in Figure 3.32 and Figure 3.33 and the adsorption energy values for vdW-DF2-C09 are 466 meV at a distance of 3.37 Å for C₆H₆ and 515 meV at a distance of 2.87 Å for C₇H₈.

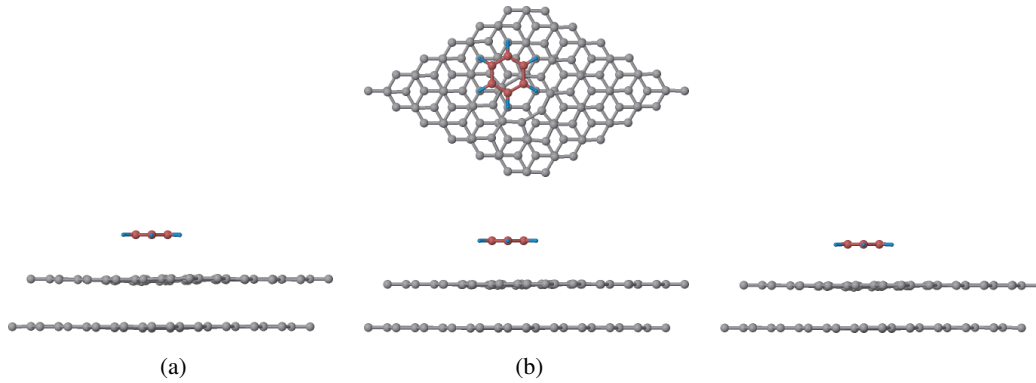


Figure 3.32: The top view and the side view for optimized geometries of C₆H₆ on PD for vdW-DF (a), vdW-DF2-C09 (b), and Grimme-D2 (c).

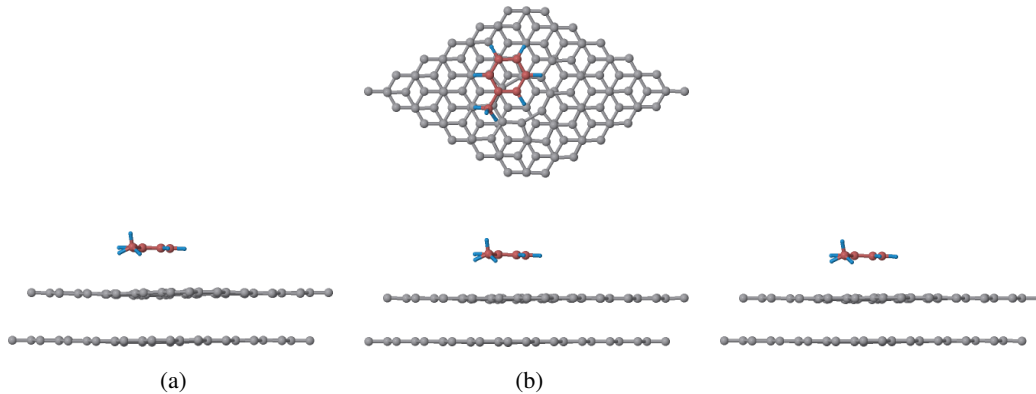


Figure 3.33: The top view and the side view for optimized geometries of C₇H₈ on PD for vdW-DF (a), vdW-DF2-C09 (b), and Grimme-D2 (c).

From the band structures displayed in Figure 3.34, it is observed that there is no deviation around the K-point from bilayer graphene’s band structure (displayed on top of Figure 3.34). For defective graphene, no deviation is observed around the K-point of defective graphene’s band structure (displayed on top of Figure 3.35 and Figure 3.37) as displayed in Figure 3.35 for PV and Figure 3.37 for PD.

Additional states from the molecules only fell on the conduction and valence parts as observed for organic molecules on single layer graphene sheet (for PDOS plots,

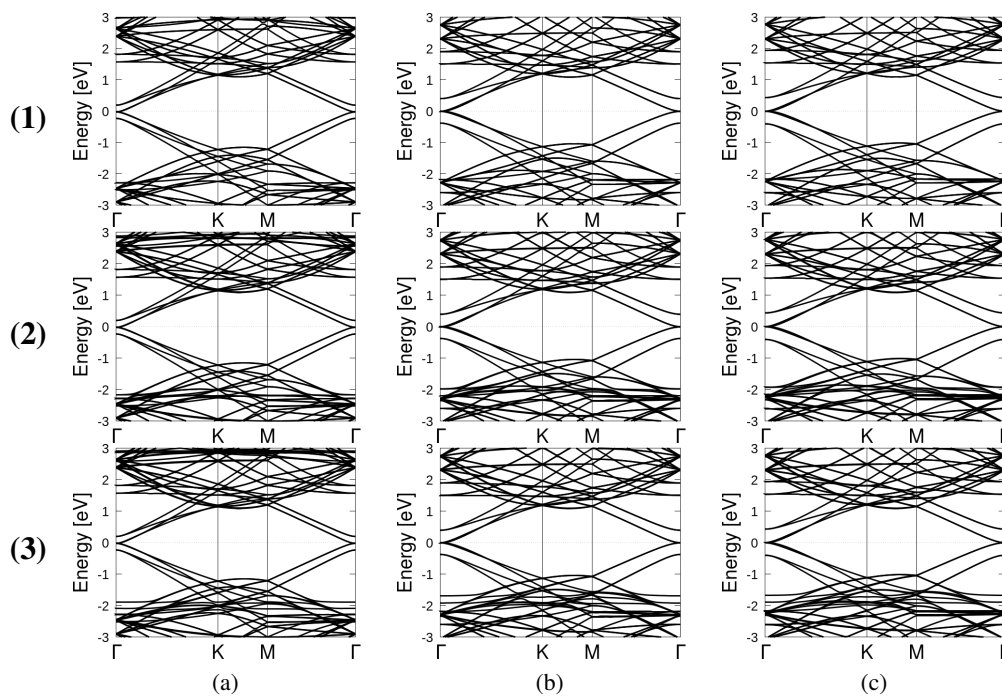


Figure 3.34: Band structure of (1) PP alone, (2) C_6H_6 on PP, and (3) C_7H_8 on PP for vdW-DF (a), vDW-DF2-C09 (b), and Grimme-D2 (c).

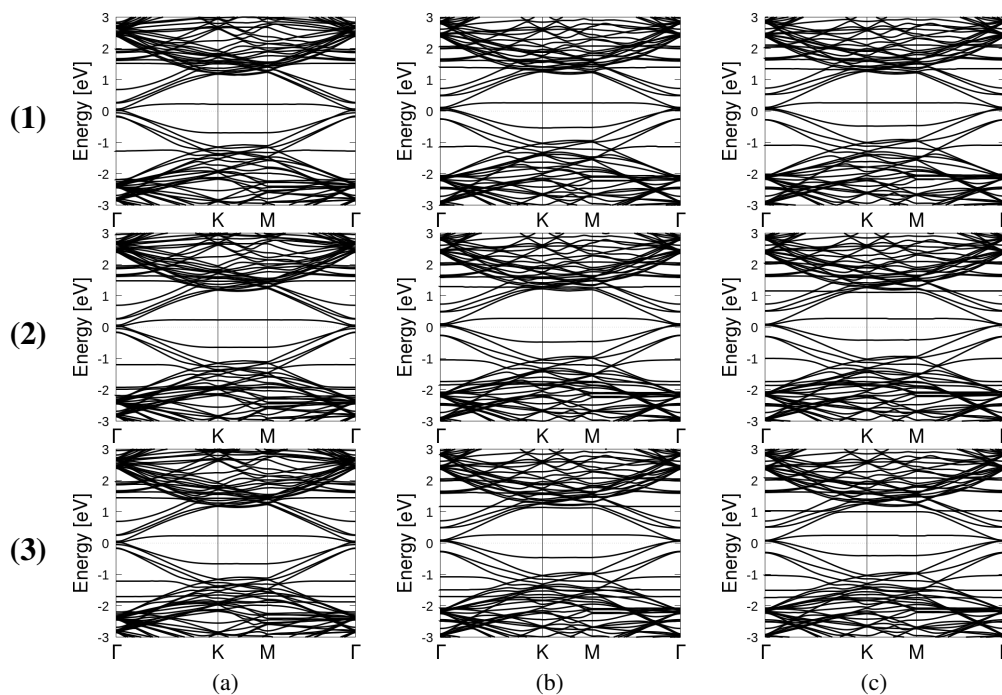


Figure 3.35: Band structure of (1) PV alone, (2) C_6H_6 on PV, and (3) C_7H_8 on PV for vdW-DF (a), vDW-DF2-C09 (b), and Grimme-D2 (c).

see Figure 3.38 and Figure 3.39 for PP adsorbent Figure 3.40 and Figure 3.42 for PV adsorbent, Figure 3.44 and Figure 3.45 for PD adsorbent).

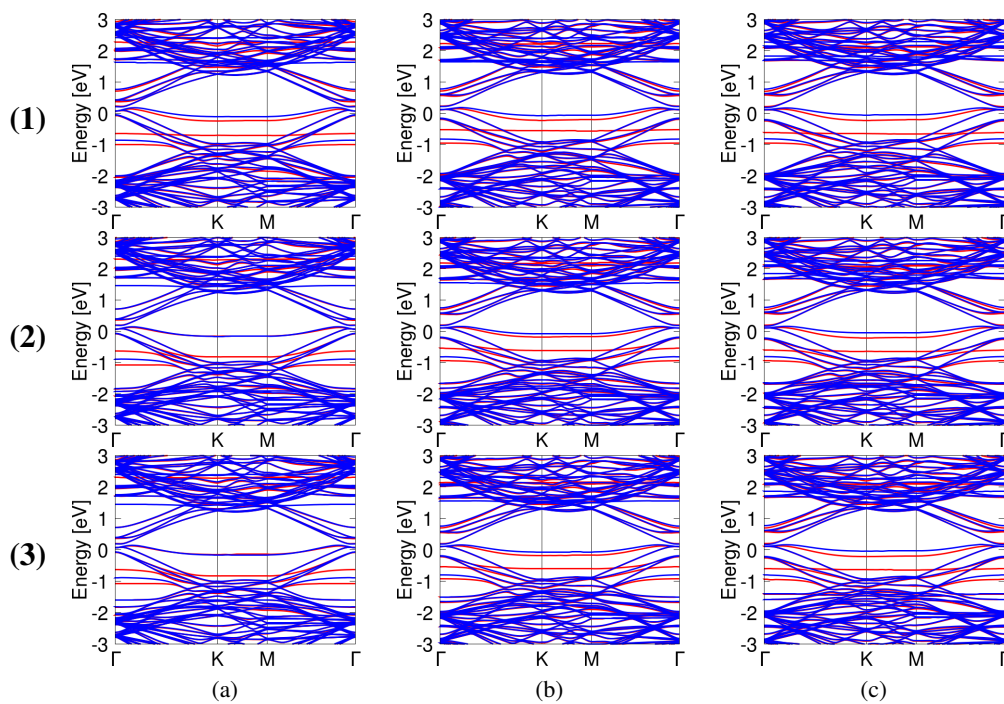


Figure 3.36: Band structure of (1) PV alone, (2) C₆H₆ on PV, and (3) C₇H₈ on PV for spin-polarized vdW-DF (a), vdW-DF2-C09 (b), and Grimme-D2 (c).

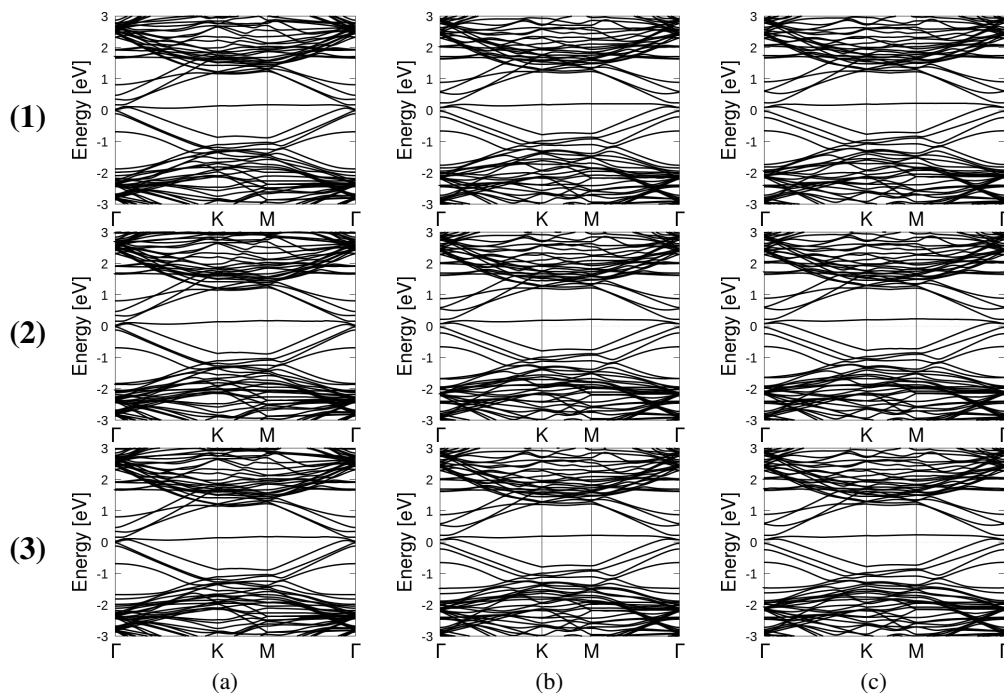


Figure 3.37: Band structure of (1) PD alone, (2) C₆H₆ on PD, and (3) C₇H₈ on PD for vdW-DF (a), vdW-DF2-C09 (b), and Grimme-D2 (c).

The charge density plots for adsorption on PP are presented in Figure 3.38 and Figure 3.39 for C_6H_6 and C_7H_8 (see Figure 3.40 and Figure 3.42 for PV, Figure 3.44 and Figure 3.45 for PD). The charge difference profiles are very similar to those for the single layer graphene, as expected. Bader charge analysis shows there is 0.008 e transfer from C_6H_6 to PP while 0.008 e is transferred from C_7H_8 to surface confirming the electron accepting characteristics of graphene-based surfaces. For PV, 0.006 e donation from C_6H_6 is observed to the top layer as VG while 0.009 e is donated from C_7H_8 . Similar characteristics is observed with 0.013 e donation from C_6H_6 to the top layer of PD while C_7H_8 donates 0.009 e to the surface.

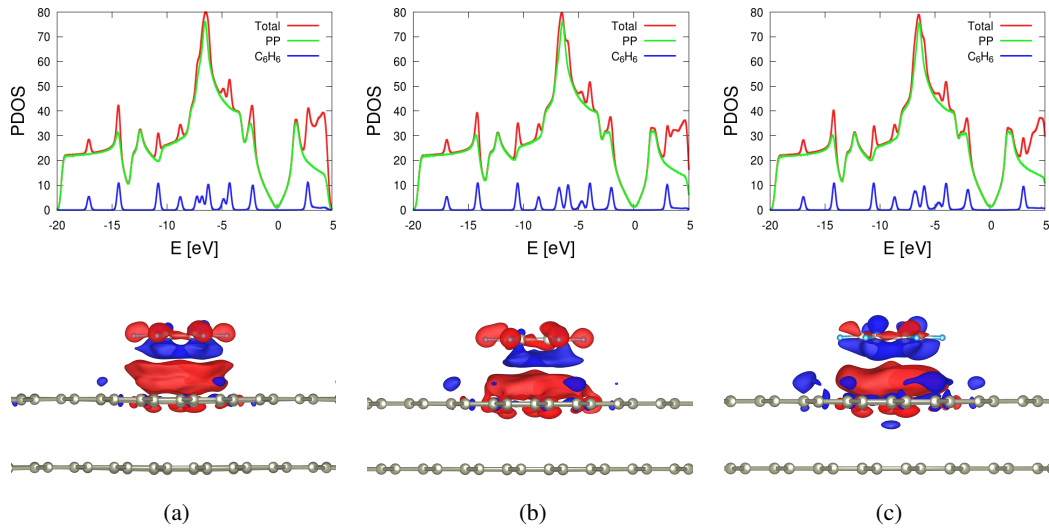


Figure 3.38: PDOS and charge density plots of C_6H_6 on PP for vdW-DF (a), vdW-DF2-C09 (b), and Grimme-D2 (c). The isovalue is set to $\pm 0.000095 \text{ \AA}^{-3}$.

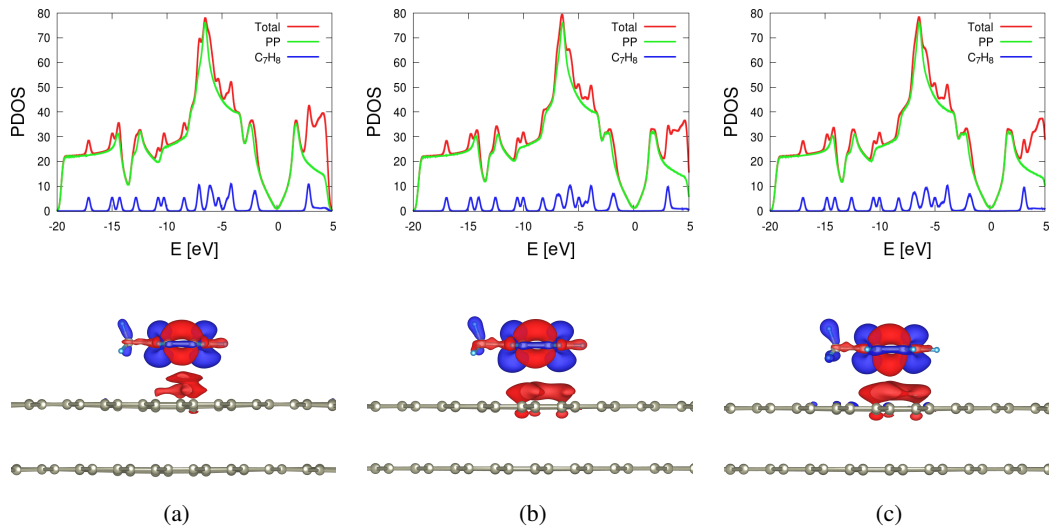


Figure 3.39: PDOS and charge density plots of C_7H_8 on PP for vdW-DF (a), vdW-DF2-C09 (b), and Grimme-D2 (c). The isovalue is set to $\pm 0.0003 \text{ \AA}^{-3}$.

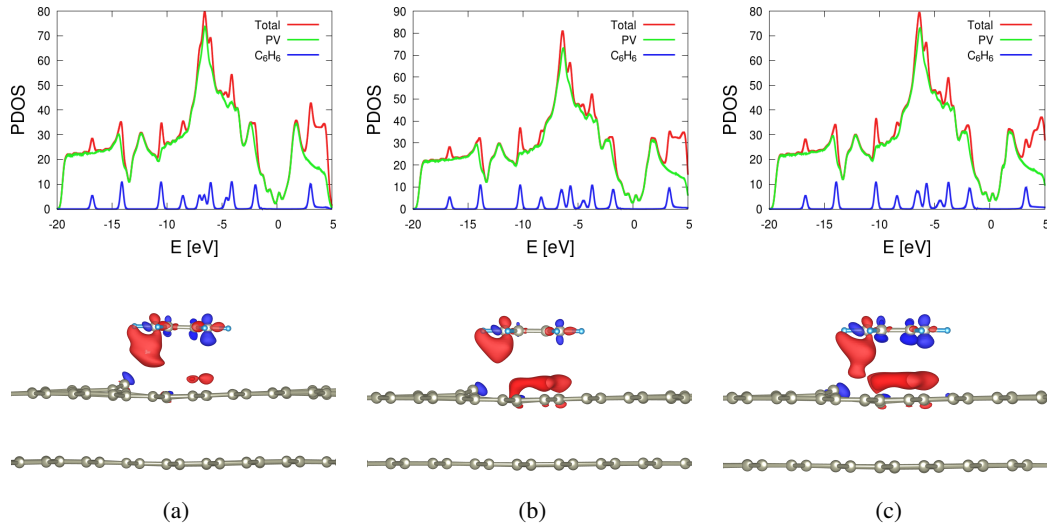


Figure 3.40: PDOS and charge density plots of C₆H₆ on PV for spin-unpolarized vdW-DF (a), vdW-DF2-C09 (b), and Grimme-D2 (c). The isovalue is set to $\pm 0.00035 \text{ \AA}^{-3}$.

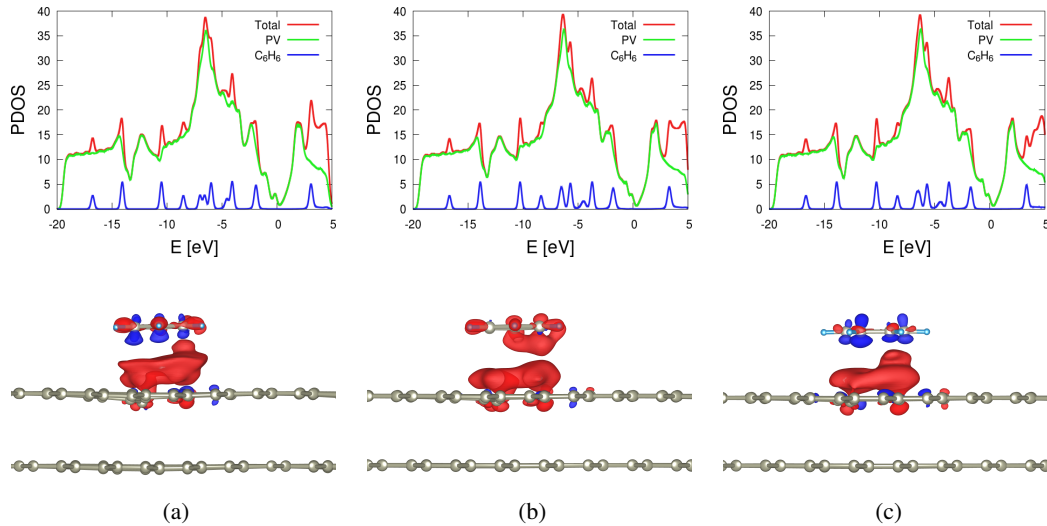


Figure 3.41: PDOS and charge density plots of C₆H₆ on PV for spin-polarized vdW-DF (a), vdW-DF2-C09 (b), and Grimme-D2 (c). The isovalue is set to $\pm 0.0002 \text{ \AA}^{-3}$.

In order to see the effect of the second layer of graphene on the adsorption energy, the adsorption energy values for vdW-DF, vdW-DF2-C09 and Grimme-D2 are tabulated in 3.4. As seen from Table 3.4, the adsorption energy is higher for both organic molecules on bilayer graphene than the adsorption energy of organic molecules on single layer graphene. From Table 3.4, with the existence of vdW-DF2-C09, an interesting fact has been revealed that the presence of the second layer increases the adsorption energy by approximately 70 meV for both molecules. For vdW-DF and Grimme-D2, this difference is approximately 50 meV. Furthermore, adsorption ener-

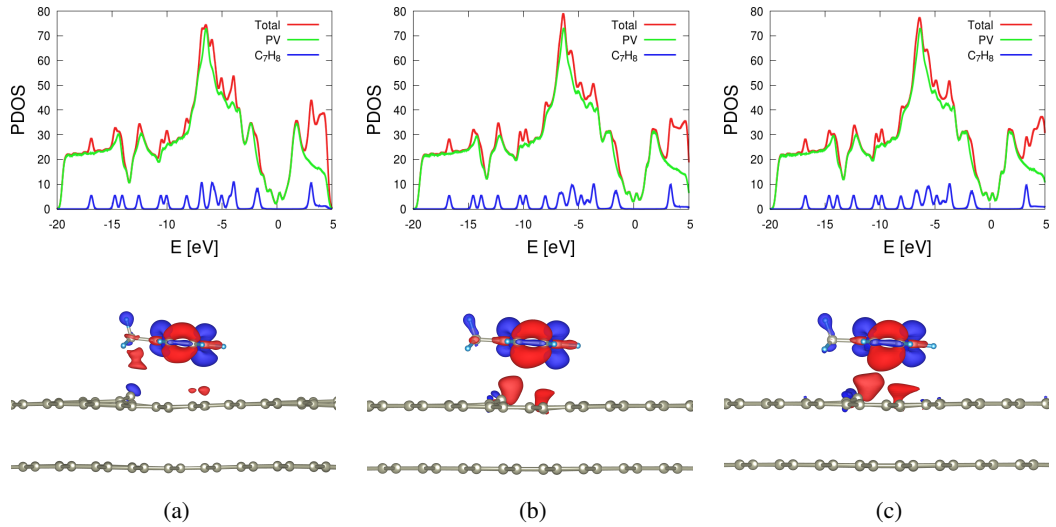


Figure 3.42: PDOS and charge density plots of C_7H_8 on PV for spin-unpolarized vdW-DF (a), vdW-DF2-C09 (b), and Grimme-D2 (c). The isovalue is set to $\pm 0.0004 \text{ \AA}^{-3}$.

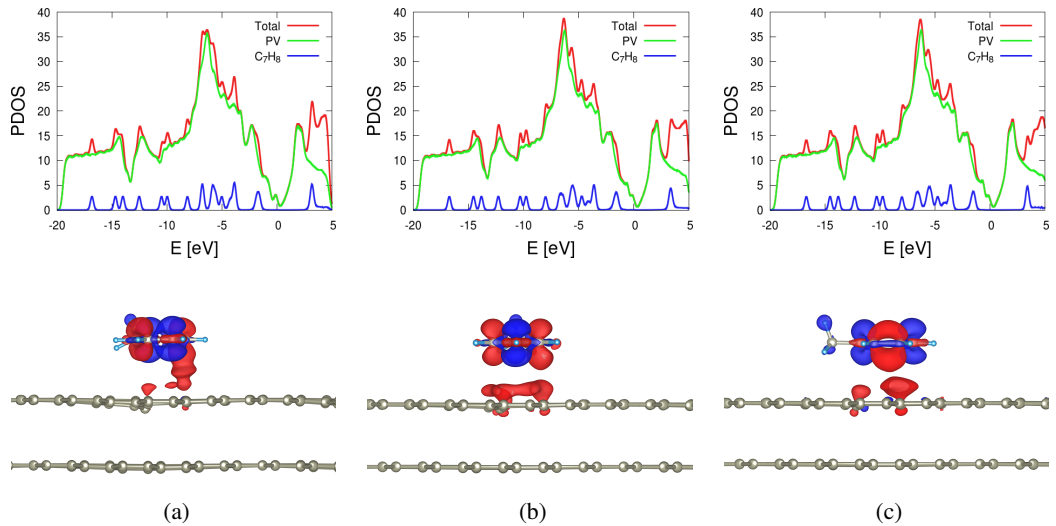


Figure 3.43: PDOS and charge density plots of C_7H_8 on PV for spin-polarized vdW-DF (a), vdW-DF2-C09 (b), and Grimme-D2 (c). The isovalue is set to $\pm 0.0004 \text{ \AA}^{-3}$.

gies of both molecules on divacancy defects are higher than being adsorbed on vacancy defect probably due to a higher degree of alignment, which results from the flat geometry of the divacancy. Additionally, charge transfer values are tabulated with the adsorption energy values and adsorption distances for organic molecules on bilayer graphene and single layer graphene in Table 3.5 where vdW-DF2-C09 is employed.

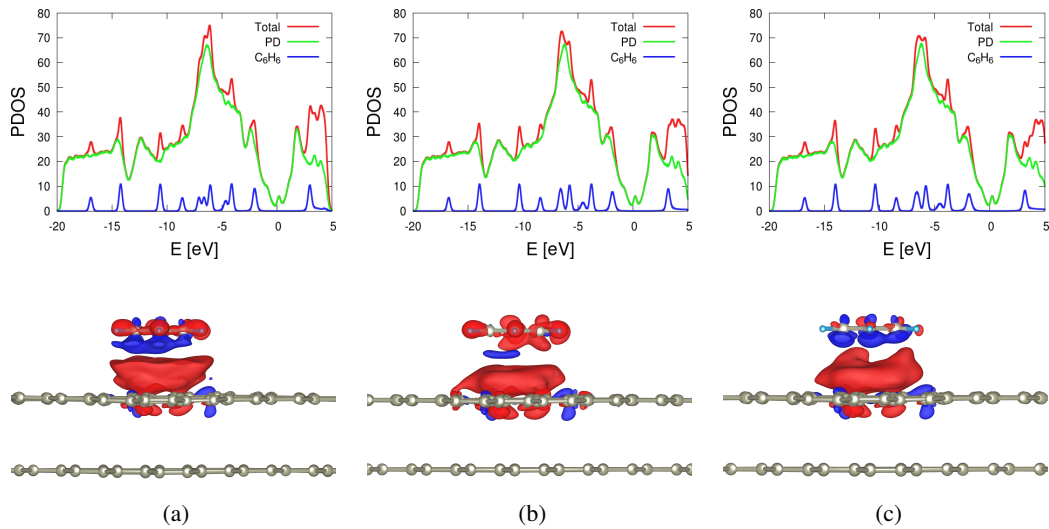


Figure 3.44: PDOS and charge density plots of C_6H_6 on PD for vdW-DF (a), vdW-DF2-C09 (b), and Grimme-D2 (c). The isovalue is set to $\pm 0.00013 \text{ \AA}^{-3}$.

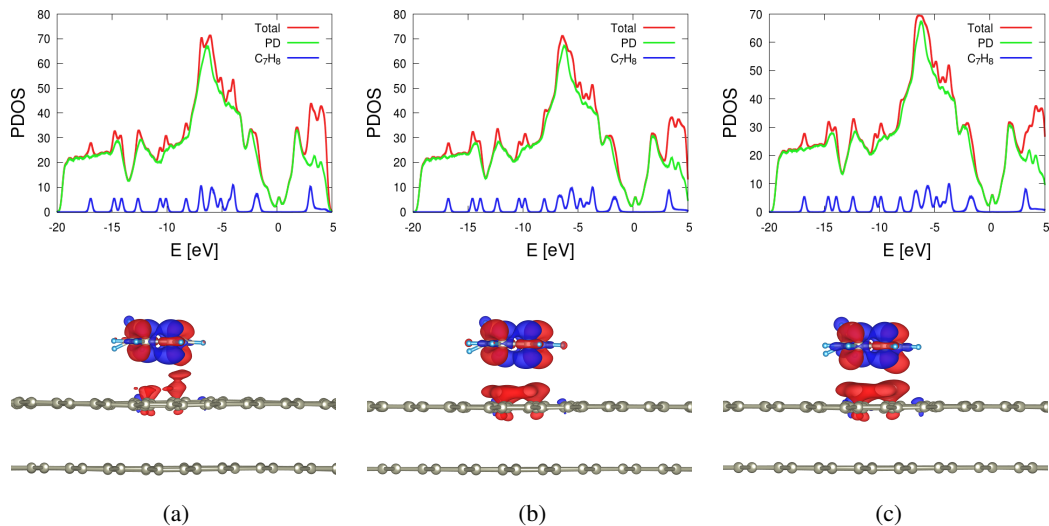


Figure 3.45: PDOS and charge density plots of C_7H_8 on PD for vdW-DF (a), vdW-DF2-C09 (b), and Grimme-D2 (c). The isovalue is set to $\pm 0.00038 \text{ \AA}^{-3}$.

Table 3.4: The adsorption energies for C_6H_6 C_7H_8 on single layer and bilayer graphene.

	Single Layer Graphene			Bilayer Graphene				
	vdW-DF	vdW-DF2-C09	Grimme-D2	vdW-DF	vdW-DF2-C09	Grimme-D2		
	E [meV]	E [meV]	E [meV]	E [meV]	E [meV]	E [meV]		
C_6H_6	on PG	596	441	524	on PP	643	508	554
	on VG	555	391	435	on PV	592	432	466
	on DG	575	404	452	on PD	611	466	495
C_7H_8	on PG	689	498	593	on PP	730	566	640
	on VG	607	425	482	on PV	659	486	536
	on DG	651	448	518	on PD	695	515	567

Table 3.5: The adsorption distances, energies and charge transfer values of C_6H_6 and C_7H_8 on single layer and bilayer graphene. (vdW-DF2-C09 employed calculations are displayed).

		Single Layer Graphene			Bilayer Graphene			
		d [\AA]	E [meV]	charge transfer per molecule (e)	d [\AA]	E [meV]	charge transfer per molecule (e)	
C_6H_6	PG	3.30	441	+0.007	PP	3.28	508	+0.008
	VG	3.71	391	+0.007	PV	3.55	432	+0.006
	DG	3.42	404	+0.019	PD	3.37	466	+0.013
C_7H_8	PG	2.93	498	+0.013	PP	2.89	566	+0.008
	VG	3.19	425	+0.011	PV	3.14	486	+0.009
	DG	2.96	448	+0.012	PD	2.93	515	+0.009

CHAPTER 4

BORON DOPING TO DEFECTIVE GRAPHENE

In this chapter, we focus on one of the most commonly utilized dopants for graphene, namely boron (B). Our motivation derives from the academic and technological importance of doped graphene. The vacancy defect and substitutional B both result in the displacement of the Fermi level. Introducing them both in the graphene network may provide us with a potential tool to controllably engineer the electronic properties of graphene. For this purpose, we present a systematic study of the magnetization characteristics of B doped defective graphene and the effect of the details of substitutional doping of boron in the defective graphene sheet by changing the doping configuration. This chapter can be viewed as a preliminary study for the investigation of adsorption of benzene derivatives on B doped defective graphene to be presented in Chapter 5. To act as our undoped substrate, we choose two types of defective graphene sheets with a single mono vacancy and a single divacancy defect. In all of the calculations presented in this chapter, vdW dispersion forces are included with vdW-DF2-C09 since this exchange-correlation protocol for the vdW interactions produces the closest agreement for graphene-based structures [159, 201] and spin-polarization is included for the calculations of B doped vacancy-defected graphene.

4.1 Previous Work

Pristine graphene has limited usage in electronic devices since it has zero band gap, and it is important to have tunable band gap for device applications. Various ap-

proaches including chemical doping have been proposed for band gap engineering of graphene so as to improve their semiconducting properties. Furthermore, chemical doping of elements in graphene gives rise to useful applications such as supercapacitance ability [202], fuel cells [203], batteries [58] and water splitting [204,205], oxygen reduction reaction (ORR) [206], hydrogen evolution reaction (HER), field emission [207], hydrogen storage [208], solar cells [209], battery applications [210] and anode materials for lithium ion batteries (LiBs) [211,212].

Experimental and theoretical studies show the possibility of producing p-type and n-type semiconducting graphene for manipulating the band structure [197]. P-type dopants such as aluminum (Al), boron (B), hydrogen (H), fluorine (F), oxygen (O), tetracyanoethylene (TCNE) and n-type dopants such as nitrogen (N), phosphorus (P) and sulphur (S) have been extensively studied earlier [213–218] in the form of substituted and covalently bonded foreign atoms [60,212].

Among the dopants described above, B and N are the most commonly studied ones due to their comparable sizes and atomic masses with carbon. Such chemically doped materials have unique properties; for example, N is a good electron-donor while B is a good electron-acceptor which allows graphene to be a versatile material which can be used in many energy-related areas [63]. Lherbier et al. [216] studied the charge mobilities and conductivity of the system by doping graphene with different concentrations of B and N impurities while Wu et al. [219] studied the band gap opening in graphene by doping B and N separately, and Deng et al. [220] studied the band gap opening in graphene by codoping with B and N [197].

The heteroatom in our focus is B which is a unique element in terms of electron deficiency and Lewis acidity. B doping causes the Dirac point to move below the Fermi level [56,220] and offers a wide variety of functionalization in chemical sensing [221], nanoelectronics [222,223], photocatalysis [224] and battery electrodes [225,226]. In literature, several synthesis methods, like the chemical vapour deposition (CVD) with diborane (B_2H_6), boron trichloride (BCl_3), and phenylboronic acid ($PhB(OH)_2$) [224,225,227–229], the reactive microwave plasma method with trimethylborane ($B(CH_3)_3$) [230], arc-discharge process [227], hydrothermal method [231] have been reported [212,226]. From the studies of Faccio et al. [232], it was

reported that the process of boron doping was unfavorable for pristine graphene while it turned to be favorable when B atoms fill in already existing carbon vacancies.

Despite all the available work, a systematic study of exact role of concentration and position of dopant atoms in modulating the band gap of graphene has not appeared in the literature yet. In the rest of this chapter, we first present a brief investigation of the magnetic properties of B defective graphene, as the magnetic state of graphene defects may depend sensitively on the calculation parameters. Once an unambiguous understanding of the magnetic behavior is achieved, we proceed with the structural and electronic properties of these composite defects.

4.2 Magnetization of Boron Doped Defective Graphene

4.2.1 Magnetization of Boron Doped Vacancy-Defected Graphene

When a vacancy is formed, two of the three neighboring atoms form a weak bond, leaving out the third neighbor as seen in Figure 2.4. This unsaturated atom may further break the symmetry by means of an out-of-plane displacement or remain at the same level as the graphene sheet. The extent of the out-of-plane displacement depends on the spin state. In our preliminary calculations (Section 2.3.2), the magnetization of the single vacancy in graphene was calculated to be $1.43 \mu_B$ per cell in the state where the unsaturated atom is 0.07 \AA above the graphene plane.

In the case of the unsaturated C atom replaced by B (see Figure 4.1), the energy of the system depends very sensitively on the magnetization state. A simple geometry optimization may miss the correct ground state of the system. In order to shed light on this issue, we conduct a series of geometry optimizations with fixed magnetization. The energy as a function of the magnetization state is shown in Figure 4.2. In Figure 4.2, two sets of calculations are presented. The red curve corresponds to an initial configuration where the B atom starts out at the same level as the graphene sheet. The blue curve, on the other hand, corresponds to an initial configuration where the B atom is initially displaced by 0.4 \AA . Both configurations, however, result in very similar final states. In either case, the configuration corresponding to the minimum has

a magnetic moment of about $0.9 \mu_B$ per cell and the B atom is only 0.01 \AA elevated with respect to the surface. When the optimized coordinates from the $\mu = 0.9\mu_B$ calculation is subjected to a second geometry optimization with free magnetization, the magnetization remains around $0.94 \mu_B$ per cell.

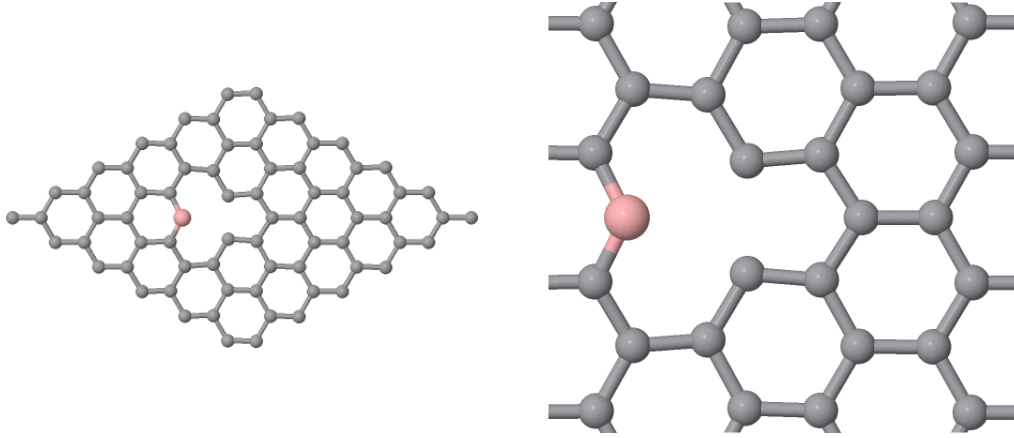


Figure 4.1: The geometry of the B doped vacancy-defected graphene (BVG).

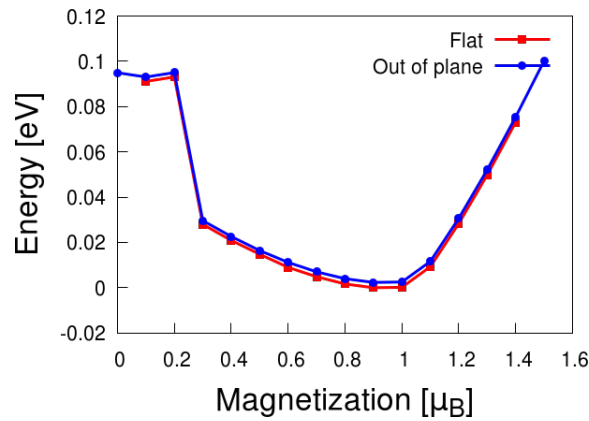


Figure 4.2: The total energy (in eV) vs. total magnetization (in μ_B) for BVG. The energy values are referenced to the minimum energy.

4.2.2 Magnetization of Boron Doped Divacancy-Defected Graphene

When a divacancy is formed, atoms around the divacancy rearrange to form bonds. As the strength of the bonds are different the atoms may once again further break the symmetry by means of some sort of distortion. To analyze the dependence of optimized geometry on the spin state, the same analyses are done as explained in the previous section. In our preliminary calculations (Section 2.3.2), the magnetization

of the divacancy in graphene is found to be $0 \mu_B$ with the unsaturated atoms at the same level as the graphene sheet.

In the case of the replacement by B of one of the C atoms in the immediate vicinity of the void, as shown in Figure 4.3, we conduct a series geometry optimizations with fixed magnetization. The energy as a function of the magnetization state is shown in Figure 4.4. Similar to Figure 4.2, the red curve represents the calculations of BVG where B is initially planar while the blue curve is for the configuration of B being displaced by 0.4 \AA . In either case, the configuration corresponding to the minimum has a magnetic moment of about $0 \mu_B$, and the B atom is only 0.01 \AA elevated with respect to the surface. When the optimized coordinates from the $\mu=0 \mu_B$ is subjected to a second geometry optimization with free magnetization, the magnetization remains around $0 \mu_B$ per cell.

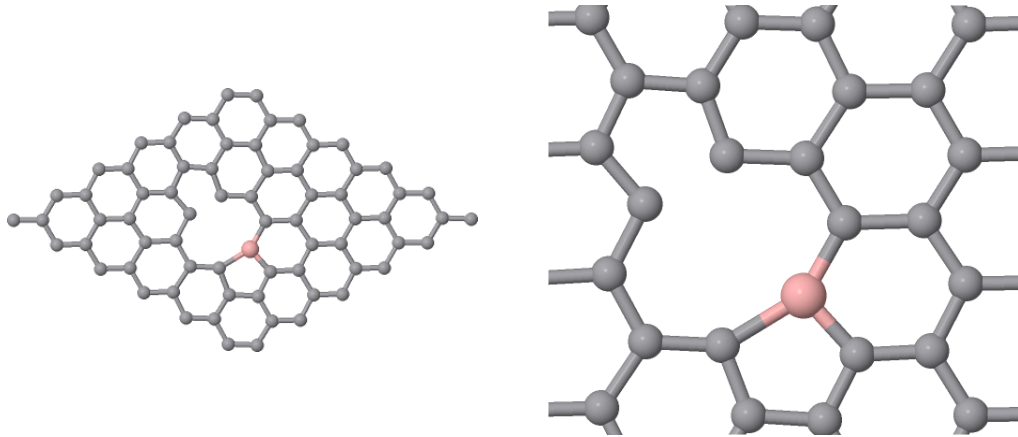


Figure 4.3: The geometry of the B doped divacancy-defected graphene (BDG).

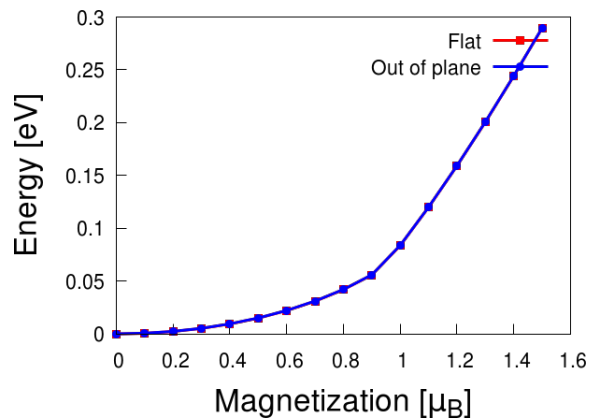


Figure 4.4: Total energy (in eV) vs. total magnetization (in μ_B) for BDG. The energy values are referenced to the minimum energy.

4.3 Electronic Properties of Boron Doped Defective Graphene

In this section, we first focus on VG followed by a study of DG. For B doping, the formation energies are calculated from:

$$E_{form} = E_{B-doped} - E_{pr-gr} + \mu_{Carbon} + \mu_{Boron} \quad (4.1)$$

where E_{form} is the formation energy, $E_{B-doped}$ is the energy of the B doped defective graphene while μ_{Carbon} is the chemical potential of the C atom which is taken as E_{pr-gr}/N where N is the number of C atoms in the unit cell of graphene. μ_{Boron} is the chemical potential for B as the energy per atom. There are several crystal forms of B and among them, only α -rhombohedral (α -B), β -rhombohedral (β -B), and γ -orthorhombic boron (γ -B) have been currently established as pure phases [233,234]. With the form of B, chemical potential and accordingly formation energy can change. In literature, there are several studies differing in the formation energies depending on the crystal form of B used as reference. Panchakarla et al. [57] studied B doping both experimentally and theoretically and estimated the energy of formation by utilizing gaseous form of dopant. With this estimation, formation energy of pristine graphene was 5.6 eV/B atom, suggesting the possibility of B doped graphene synthesis. Besides that, Faccio et al. [232] expressed $\mu_{Boron} = -77.06$ eV from the previous studies [235] where B was in its β -rhombohedral structure. For B doping to 6x6 pristine graphene, formation energy was calculated to be 0.919 eV while it was -1.582 eV for B doping to 6x6 VG where B is doped in vacancy with symmetric disposition [232]. In another study done by Hardikar et al. [236], the formation energies were expressed as -2.30 eV for one B doping to VG and -1.25 eV for one B doping to DG without giving information about the crystal structure of B. In our work, we take B in its gaseous form and formation energies are calculated to be -2.99 eV and -2.25 eV for one B doping to VG and DG, respectively which are in parallel agreement with previous results of Hardikar et al. [236].

4.3.1 Boron Doped Vacancy-Defected Graphene

Starting out with the optimized geometry of VG, we study two groups for configurations. In the first group we remove one C atom from the optimized geometry of VG and replace it with B while in the second group we remove two C atoms and replace them with B. In one of the configurations (labeled as E), out of plane displacement of B by 0.2 Å is examined. In order to see the effect of the B position, the optimization calculations are performed for different configurations of these groups. The optimized configurations are shown in Figure 4.5.

Upon single B doping, the atoms of VG remain coplanar, while the bond length of the two C–B bonds around B slightly increase by 0.15 Å to 1.54 Å. In the case of double B-doped graphene, C-B bonds lengths increase by 0.11 Å to 1.50 Å and the distance between B-B shrinks by 0.21 Å to 2.30 Å in case of two B doping. Additionally, out of plane doped B becomes coplanar at the end of optimization calculations.

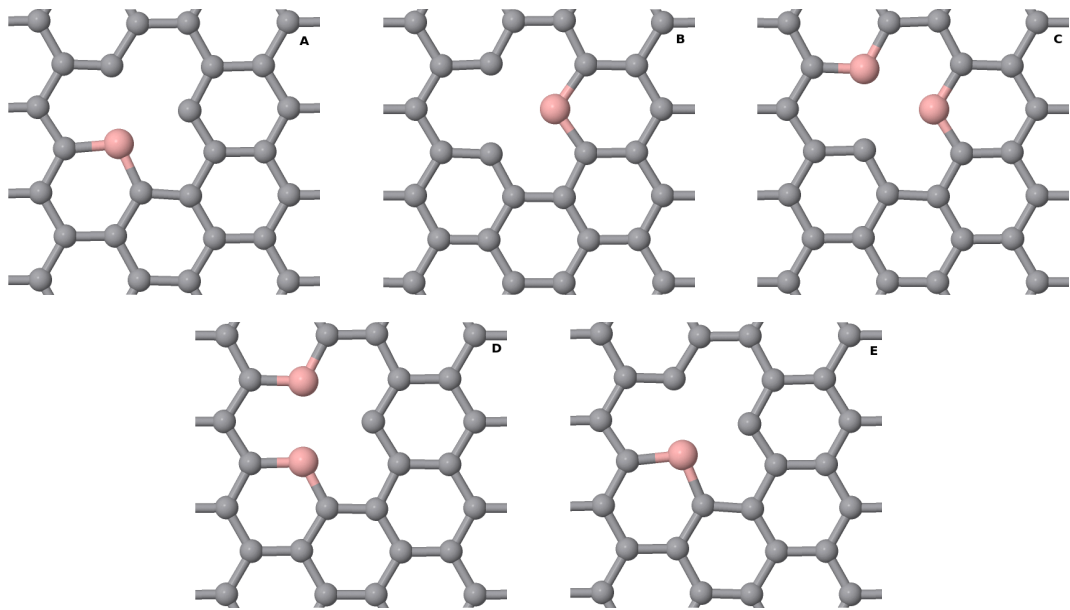


Figure 4.5: The optimized configurations of BVG.

During calculations, an initial spin-polarization is applied to C in different optimization calculations where the starting magnetization is set to $0.2 \mu_B$. After geometry optimization, for the configuration utilized in Section 4.2.1, the resulting magnetization is calculated to be $0.94 \mu_B$ per cell confirming our previous results obtained in Section 4.2.1.

Additionally, we study B introduced as an adatom close to the defect where B is placed 1.5 Å away from VG surface. The initial and the optimized geometries are displayed in Figure 4.6. After optimization, B atoms become nearly coplanar and forms three C-B bonds resulting in a configuration of B doped pristine graphene with 1.49 Å C-B bond length while the resulting magnetization is calculated to be 0 μ_B .

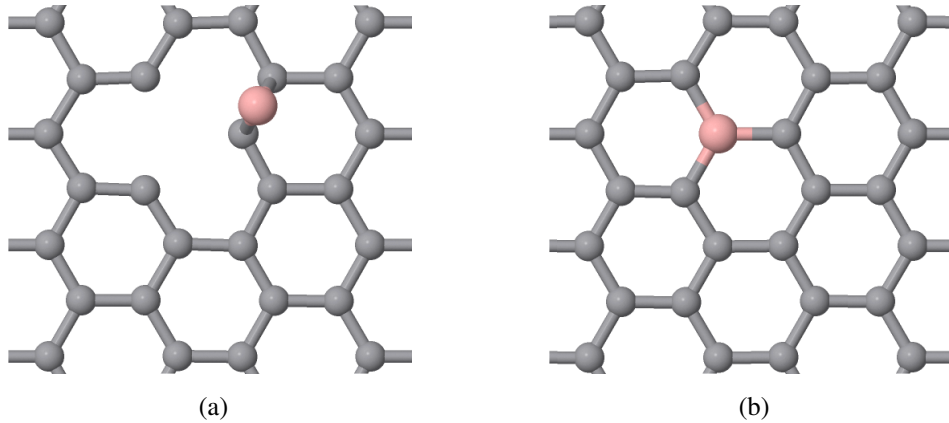


Figure 4.6: The initial and the optimized configurations of BVG where B is doped as an adatom.

For the configurations shown in Figure 4.5 and 4.6, the magnetization values of BVG are tabulated in Table 4.1 with the initial and the optimized displacement (in z position) of B atoms. As observed from Table 4.1, resulting magnetization is 0 μ_B per cell for two B introduced configurations while it is 0.94 μ_B per cell when one B is placed planarly. Furthermore, for B atom displaced by 0.02 Å initially, even if it becomes nearly planar at the end of optimization, magnetization is 0.75 μ_B per cell different from the initially planar B doped configurations. For B as an adatom, since the resulting configuration is B doped pristine graphene, magnetization is 0.00 μ_B per cell as expected.

When compared with the band structure of bare VG presented in Figure 4.7, VG with B impurity is positively doped which is reflected in the band structure as an upward shift. For the band structure, red lines in Figure 4.7 represent the majority spin while blue lines represent the minority spin. The band gap opening increases with increased concentration of B and for B doping as an adatom, the band structure is similar with the band structure of bare PG with Fermi level being shifted downwards. Addition-

Table 4.1: The displacement of B atoms and total magnetization (μ_B per cell) of optimized BVG. The configurations of BVG are displayed in Figure 4.5 and 4.6.

Label	initial z-position of B (\AA)	optimized z-position of B (\AA)	μ_B per cell
A	0.00	0.00	0.94
B	0.00	0.00	0.94
C	0.00, 0.00	0.00, 0.00	0.00
D	0.00, 0.00	0.00, 0.00	0.00
E	0.20	0.02	0.75
adatom	1.50	0.07	0.00

ally, B doping has very small contribution on total states of BVG around the Fermi level and in the conduction band as presented in the PDOS plots (see Figure 4.8).

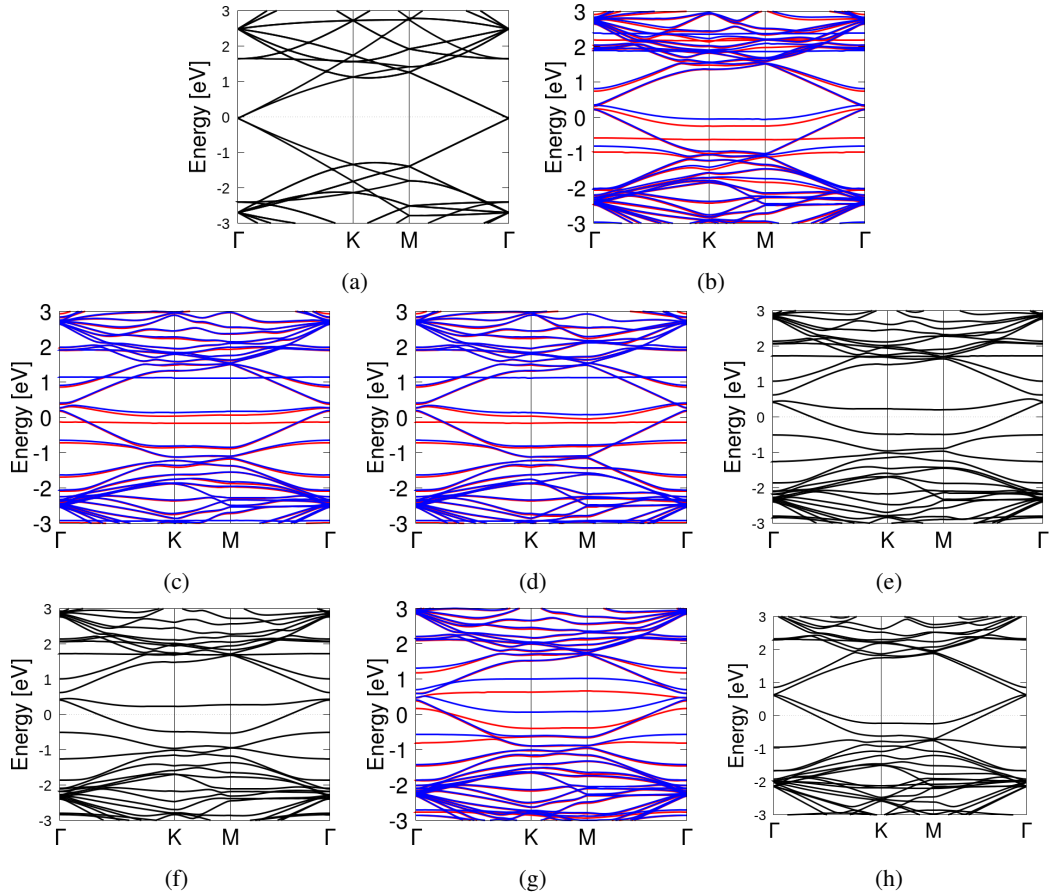


Figure 4.7: Band structure of PG (a), spin-polarized VG (b), BVG with configuration labeled as A (c), B (d), C (e), D (f), E (g) and adatom (h).

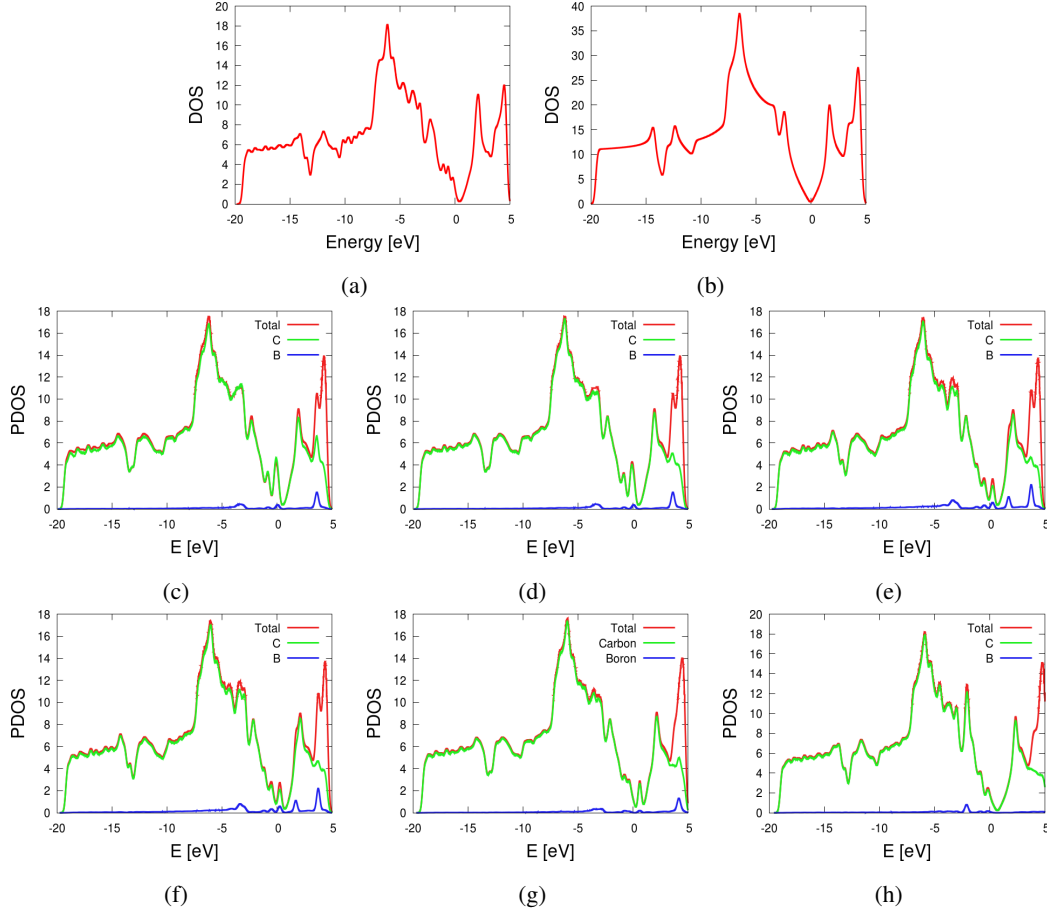


Figure 4.8: PDOS plot of PG (a), spin-polarized VG (b), BVG with configuration labeled as A (c), B (d), C (e), D (f), E (g) and adatom (h).

4.3.2 Boron Doped Divacancy-Defected Graphene

Similarly to the procedure explained in Section 4.3.1, the initial configurations are divided into two groups involving the replacement of one B atom with one C atom and two B atoms with two C atoms with the optimized geometry of DG taken as the starting point. Furthermore, an additional configuration (labeled as G) with out of plane introducing of B by 0.2 \AA is examined. Finally, we study one more configuration where we place B at the center of the defect in two configurations at the same level as the graphene sheet and 2.5 \AA away from the graphene sheet. In order to see the effect of B position, optimization calculations have been performed for these several configurations and optimized configurations are shown in Figure 4.9.

Upon B doping, the atoms of DG remain coplanar, while those B atoms placed with an initial out-of-plane displacement result in distortion of the planar graphene sheet, and

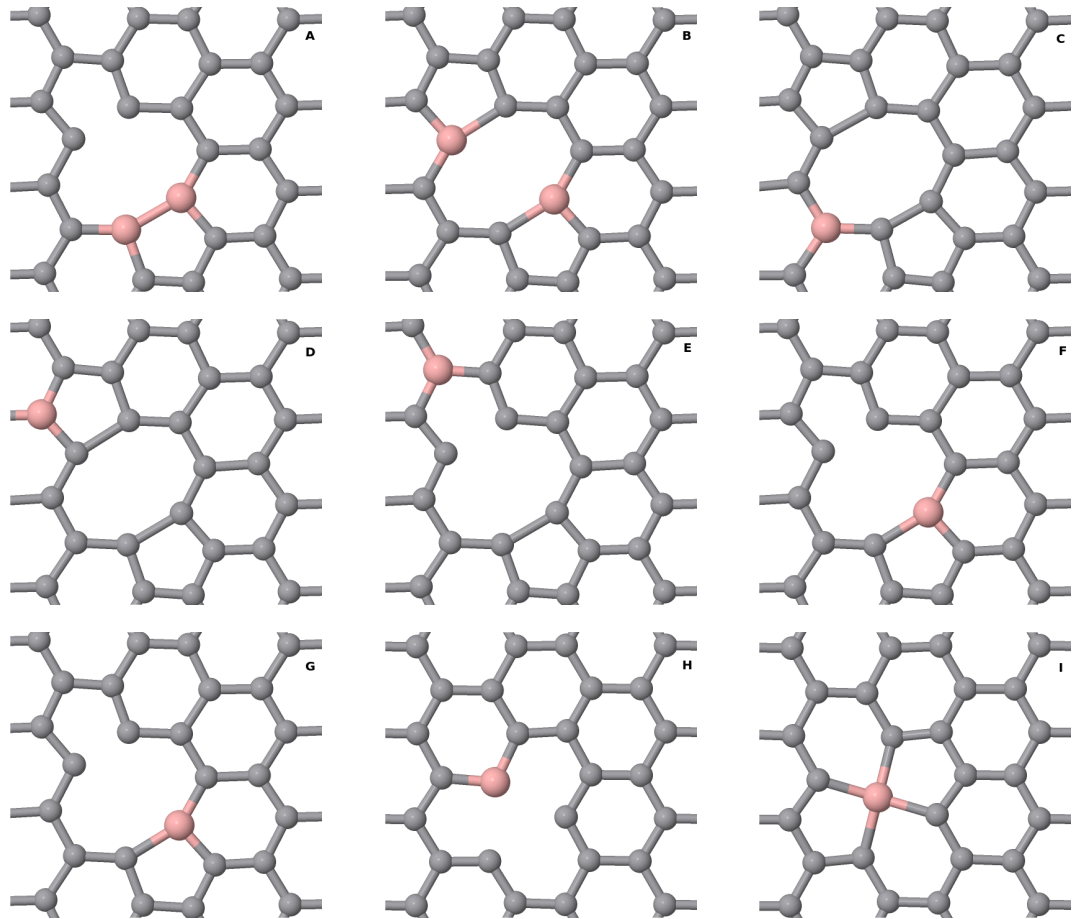


Figure 4.9: The optimized configurations of BDG.

B settles approximately at the same level as C atoms. When B is placed at the center of the defect, the resulting configuration is BVG with coplanar B while B remains at the center of distorted DG and 2.5 \AA out of plane displacement reduces to zero.

A further optimization calculation is performed for the two B atoms doping case by applying positive starting magnetization to one of the B atoms while negative starting magnetization to the other B atom in order to explore the possibility of an antiferromagnetic ground state. As a result of calculations, the magnetization is found to be $0 \mu_B$ which is in good agreement with the results presented in Section 4.2.2.

Similar to the B doping as an adatom to VG, B atoms become almost coplanar with a distance of only about 0.2 \AA away from the surface while the C atoms around B are slightly distorted from the planar surface by 0.5 \AA . Three C-B bonds are formed resulting in a configuration of VG with a C-B bond lengths of 1.51 , 1.58 and 1.61 \AA

in addition to small changes in C-C bond lengths and positions of C around the defect (see Figure 4.10).

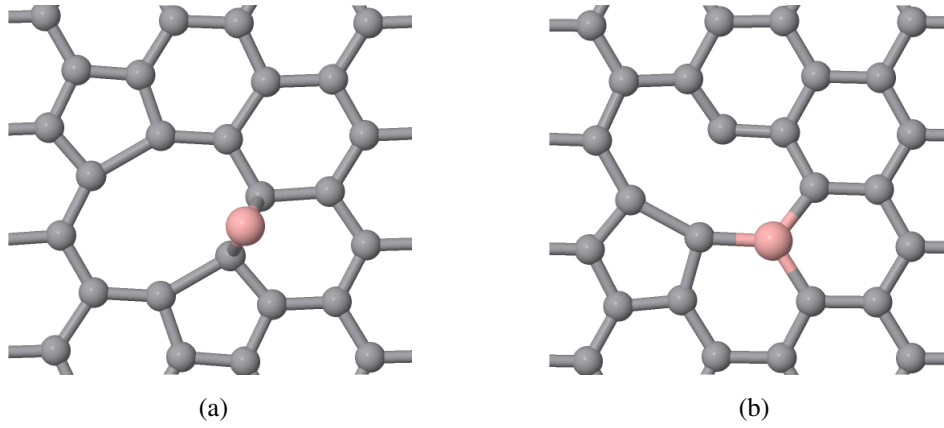


Figure 4.10: The initial and the optimized configurations of BDG where B is doped as an adatom.

For B doped as an adatom, we conduct a series geometry optimizations with fixed magnetization. The energy as a function of the magnetization state is shown in Figure 4.11 with the magnetization of BVG shown in Figure 4.2. For magnetization greater than $1 \mu_B$ per cell, state of the BVG-adatom changes and show similar trend with BVG.

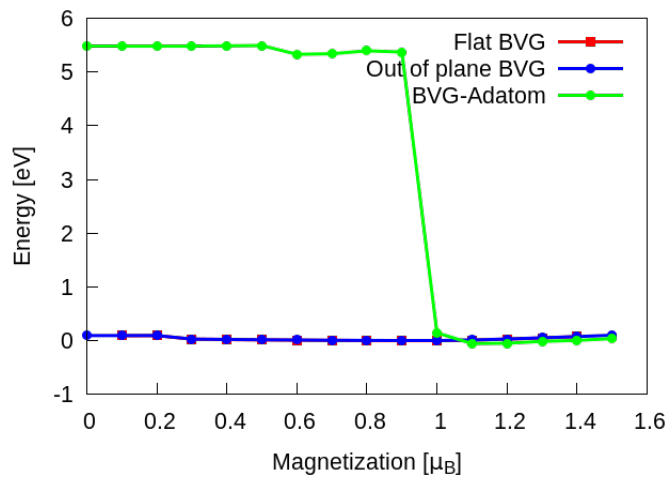


Figure 4.11: Total energy (in eV) vs. total magnetization (in μ_B) for where B is doped as an adatom. The energy values are referenced to the minimum energy.

For the configurations displayed in Figure 4.9 and Figure 4.10, the magnetization values of BDG are tabulated in Table 4.2 with the initial and the optimized displacement (in z position) of B atoms. For both BVG and BDG, charge transfer takes place from B to C.

Table 4.2: The displacement of B atoms and total magnetization (μ_B per cell) of optimized BDG. The configurations of BDG are displayed in Figure 4.9 and 4.10.

Label	initial z-position of B (\AA)	optimized z-position of B (\AA)	μ_B per cell
A	0.00	0.00, 0.00	0.00
B	0.00	0.00, 0.00	0.00
C	0.00	0.00	0.00
D	0.00	0.00	0.00
E	0.00	0.00	0.00
F	0.00	0.00	0.00
G	0.20	0.02	0.00
H	0.00	0.00	0.00
I	2.50	0.01	0.00
adatom	1.50	0.20	0.00

After optimization calculations, the band structure and PDOS calculations are performed. When compared with the band structure of bare DG presented in Figure 4.12, BDG has a band structure with an upward shift. The band gap opening increases with the increased concentration of B and for B doping as an adatom, the band structure is similar with the band structure of bare VG while the Dirac point moves below the Fermi level. Additionally, similar with BVG, B doping has very small contribution on total states of BDG as presented in the PDOS plots (see Figure 4.13).

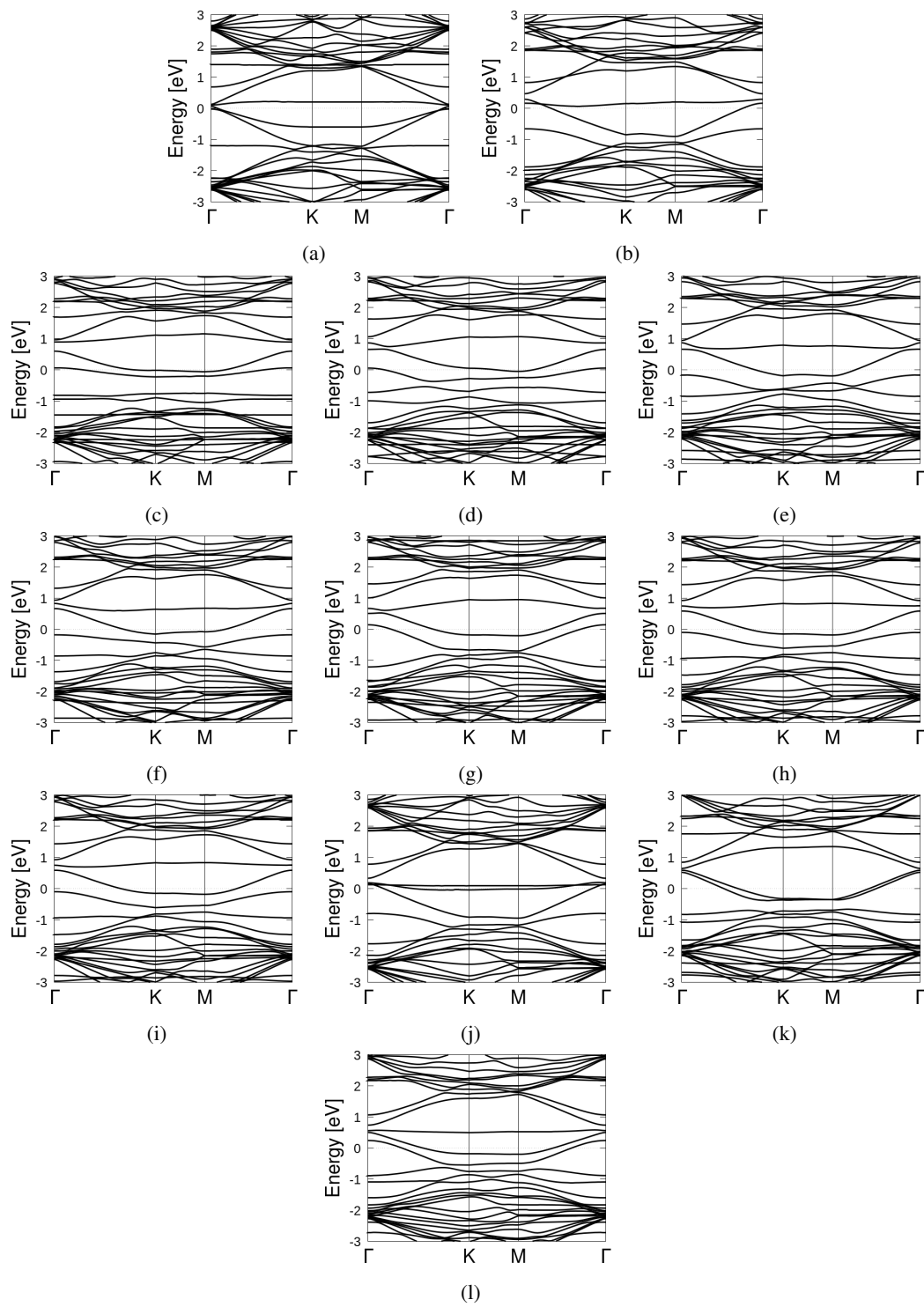


Figure 4.12: Band structure of spin-unpolarized VG (a), DG (b) and BVG with configuration labeled as A (c), B (d), C (e), D (f), E (g), F (h), G (i), H (j), I (k) and adatom (l).

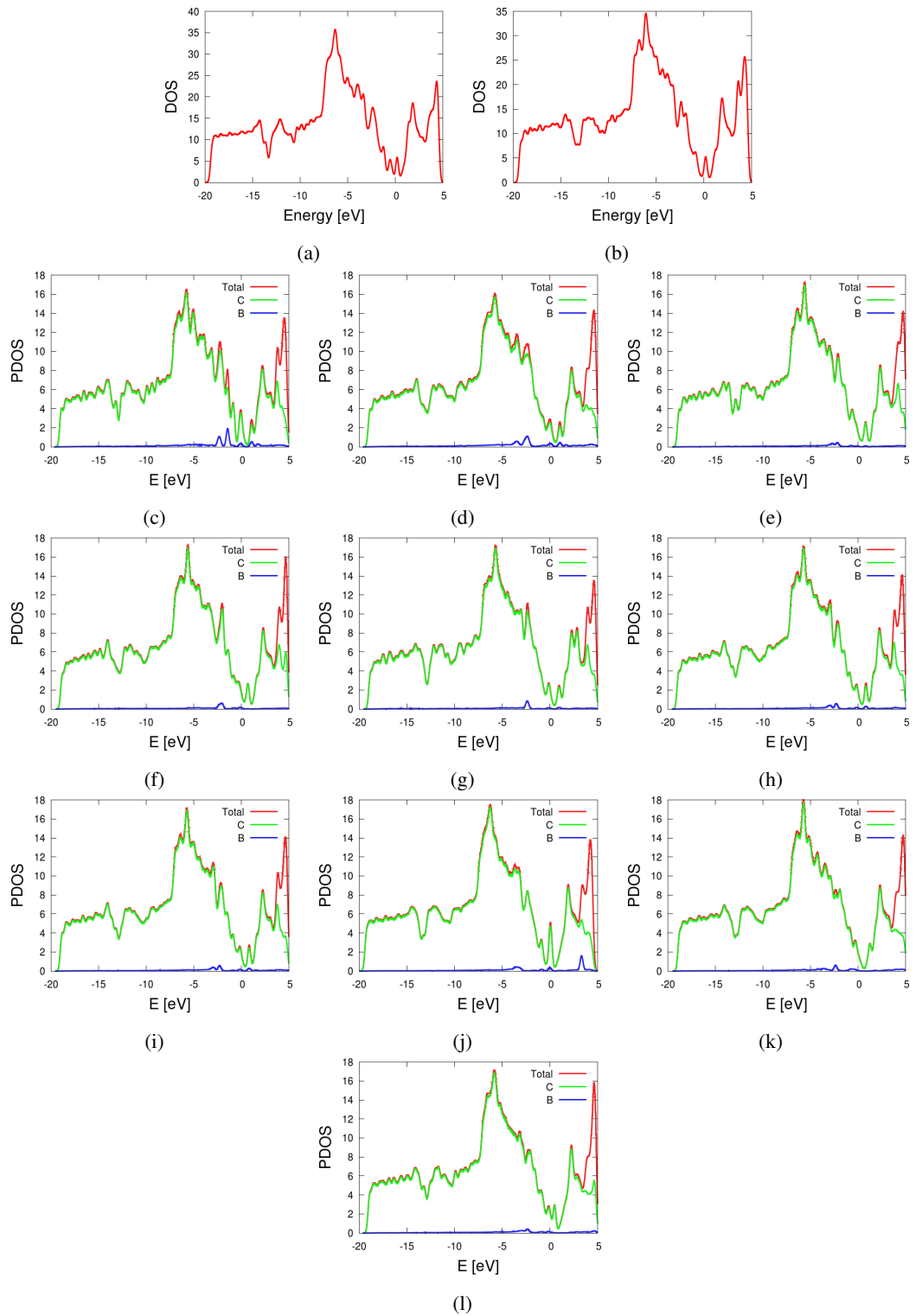


Figure 4.13: PDOS plot of spin-unpolarized VG (a), DG (b) and BVG with configuration labeled as A (c), B (d), C (e), D (f), E (g), F (h), G (i), H (j), I (k) and adatom (l).

CHAPTER 5

GRAPHENE FUNCTIONALIZATION WITH BENZENE DERIVATIVES

In this chapter, as a means of extending the degree of control over functionalization, we focus on organic adsorbates for additional control of the electronic properties of the boron (B) doped vacancy-defected graphene sheets. For this purpose, we study the geometry and electronic structure of benzene derivatives as organic adsorbates. In order to probe a wide range of electronic properties, we sample molecules from different subgroups such as hydrocarbon (toluene), halogen-containing (fluorobenzene), nitrogen-containing (benzotrile) and oxygen-containing (benzoic acid) derivatives. VdW dispersion forces with vdW-DF2-C09 are included in order to treat molecule-graphene interaction. Spin polarization is included in all calculations.

5.1 Previous Work

Graphene functionalization attracted considerable interest with halogen containing molecules such as hydrofluoric acid (HF) [241], hydrogen cyanide (HCN) [242], hydrogen chloride (HCl) [243] and nitrobenzene ($C_6H_5NO_2$) [244, 245] for their potential applications [8, 246]. They were also well described by theoretical calculations [247]. Moreover, introducing metal atom dopants such as nickel (Ni), copper (Cu), aluminum (Al) and iron (Fe) has been reported to enhance the molecule-graphene interaction, which is highly important for sensing devices [178, 179, 248].

Leenaerts et al. [70, 249] studied the charge transfer mechanisms of small molecules adsorbed on graphene, such as ammonia (NH_3) and nitrogen dioxide (NO_2). It

was reported that when molecules adsorb on graphene, charge transfer occurs. In particular, polycyclic aromatic hydrocarbons (PAH) [250] are rather well studied [251]. Corno et al. [252] studied the effective potential energy surfaces for the interaction of C_6H_6 , naphthalene ($C_{10}H_8$), coronene ($C_{24}H_{12}$), and ovalene ($C_{32}H_{14}$), with graphene. Caciuc et al. [195] studied the bonding mechanism of C_6H_6 , triazine ($C_3N_3H_3$) and borazine ($B_3N_3H_6$) adsorbed on graphene and a single boron nitride (BN) sheet reaching the conclusion that there is no charge transfer between the molecules and graphene sheets while the strength of the molecule–surface interaction corresponds to a strong physisorption. In another study, the local dipole moments in PAHs were found to have a strong effect on the surface charges of graphene. As an example, $B_3N_3H_6$ was found to induce a band gap of 62.9 meV [253]. Ganji et al. [244] studied the adsorption of three benzene derivatives namely aniline ($C_6H_5NH_2$), nitrobenzene ($C_6H_5NO_2$), and toluene (C_7H_8) on carbon nanotubes (CNT) and observed that benzene (C_6H_6) binds more strongly to the sidewall of the CNTs when compared with the other H-capped molecules. On the subject of benzene derivatives, studies have been widened to phenol (C_6H_6O), fluorobenzene (C_6H_5F) and benzonitrile (C_7H_5N) [254]. Despite all such work for graphene functionalization, study of chemical doping on defective graphene sheets are rarely observed. Furthermore, study for additional doping on the B-doped defective graphene sheets is still missing.

5.2 Molecules

Molecular structures of benzene derivatives studied in this Chapter are given in Figure 5.1. Additionally, two parameters that are important for determining the dispersion portion of the vdW interactions, namely the isotropic polarizabilities (1/3 of the trace of the polarizability tensor) and dipole moments of the gas phase molecules are calculated in the DFT framework using the GAUSSIAN (G09) software [255] and collected in Table 5.1.

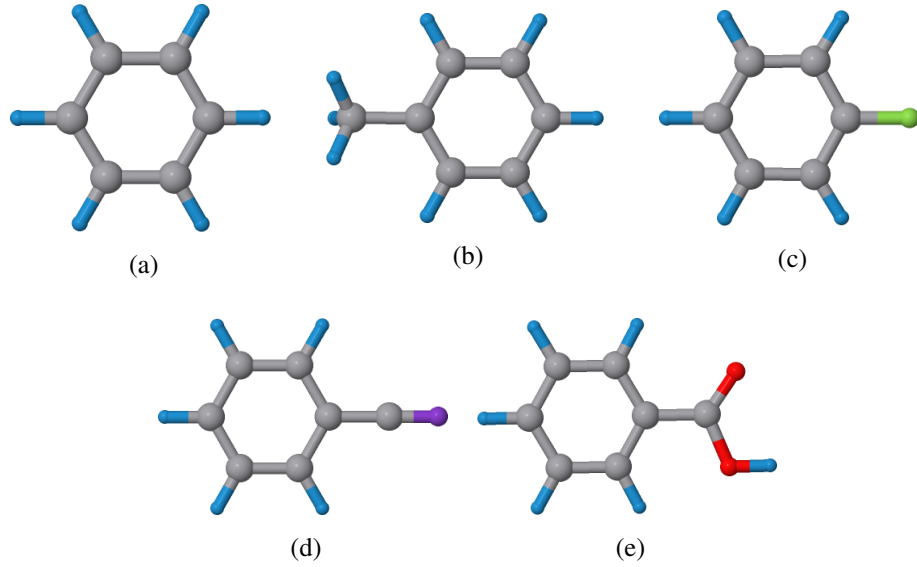


Figure 5.1: Geometries of benzene (C₆H₆) (a), toluene (C₇H₈) (b), fluorobenzene (C₆H₅F) (c), benzonitrile (C₇H₅N) (d) and benzoic acid (C₇H₆O₂)(e). C: gray, H: blue, F: green, N: purple, and O: red.

Table 5.1: Isotropic polarizabilities (α), and dipole moments (μ) of the gas phase molecules.

	α (Å ³)	μ (Debye)
C₆H₆	10.28	0.00
C₇H₈	12.30	0.41
C₆H₅F	10.29	1.56
C₇H₅N	12.89	4.71
C₇H₆O₂	13.40	2.15

5.3 Molecular Doping to B Doped Defective Graphene

As a preliminary study, C₆H₆ and C₇H₈ are adsorbed on B-doped vacancy-defected graphene (BVG) in order to observe the effect of B doping on the adsorption energy and electronic structure. Adsorption geometries with the highest adsorption energies presented in Section 3.2.2 are employed and their top view and side view of optimized geometries are presented in Figure 5.2 and Figure 5.3 for C₆H₆ and C₇H₈ with spin-polarized and spin-unpolarized conditions, respectively.

In the spin-polarized calculations, magnetization is found to be 0 μ_B per cell and

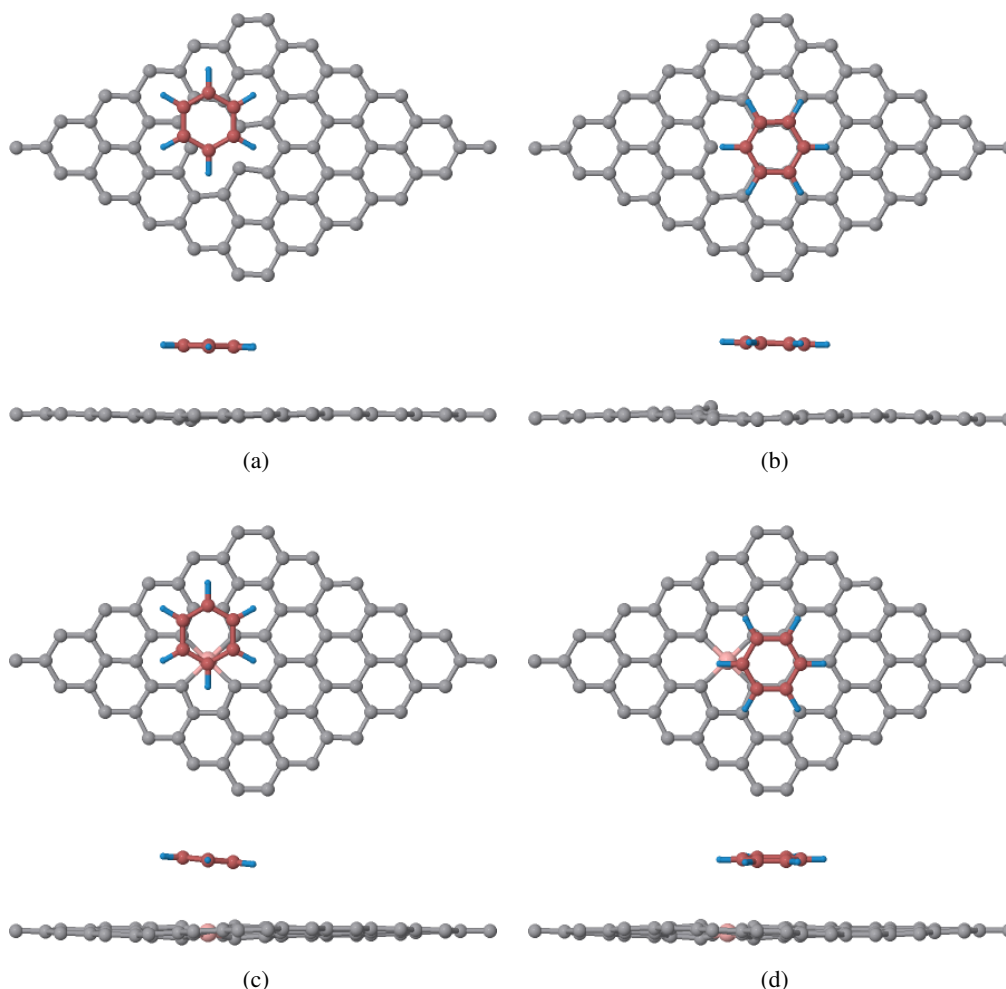


Figure 5.2: Top view and side view of C_6H_6 on VG with spin-polarized vdW-DF2-C09 (a), and spin-unpolarized vdW-DF2-C09 (b), C_6H_6 on BVG with spin-polarized vdW-DF2-C09 (c), and spin-unpolarized vdW-DF2-C09 (d).

it can therefore be concluded that there is no effect of magnetization for C_6H_6 and C_7H_8 adsorption on BVG. In the optimized structure, C_6H_6 has an adsorption energy of 776 meV while C_7H_8 has an adsorption energy of 819 meV. These values are 391 meV and 425 meV for adsorption of C_6H_6 and C_7H_8 on vacancy-defected graphene (VG), respectively (see Table 3.2). In Figure 5.2 and Figure 5.3, B is at the center of the defect in the optimized structure where B causes increased adsorption energy by the additional organic molecule–B interaction (an increase of 380–390 meV) with respect to bare VG. Furthermore, B doping on VG results in decreased curvature effect. For the band structure of spin-polarization VG, red lines in Figure 5.4 and Figure 5.5 represent the majority spin while blue lines represent the minority spin. The band structure of BVG/molecule system does not deviate significantly from the

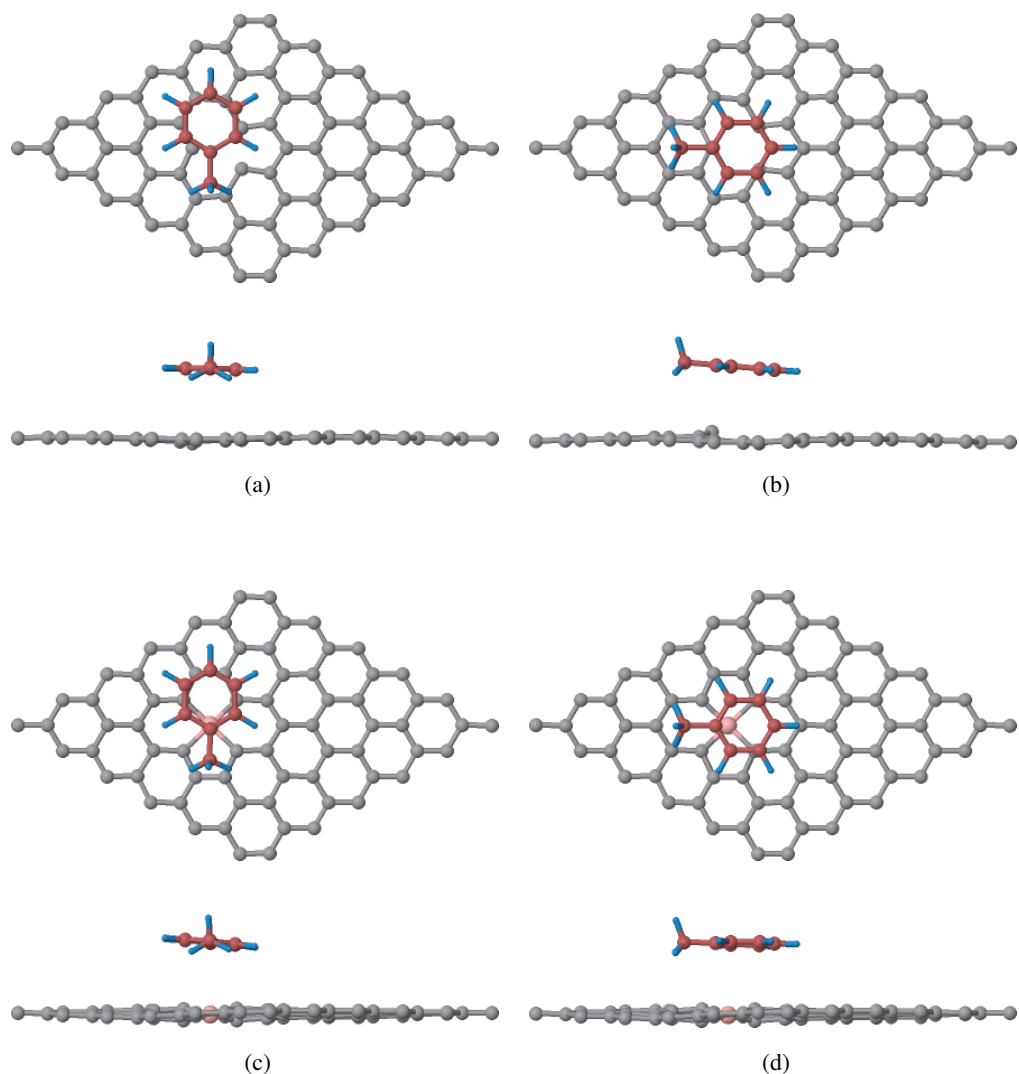


Figure 5.3: Top view and side view of C_7H_8 on VG with spin-polarized vdW-DF2-C09 (a), and spin-unpolarized vdW-DF2-C09 (b), C_7H_8 on BVG with spin-polarized vdW-DF2-C09 (c), and spin-unpolarized vdW-DF2-C09 (d).

case of VG.

As seen in the PDOS plots shown in Figure 5.6 and Figure 5.7, additional states from the molecules only fall on the conduction and valence bands similarly to the PG cases investigated previously. In the charge density difference plots, red color represents regions with charge depletion while blue color represents those with charge accumulation. In this case, the portions of the molecule closer to the elevated atom lose some electrons to both its own π orbitals and the lone atom resulting in asymmetric charge transfer. For the spin-unpolarized case, from the Bader charge analysis, the charge transfer between BVG and the molecule is calculated to be negligibly small for the

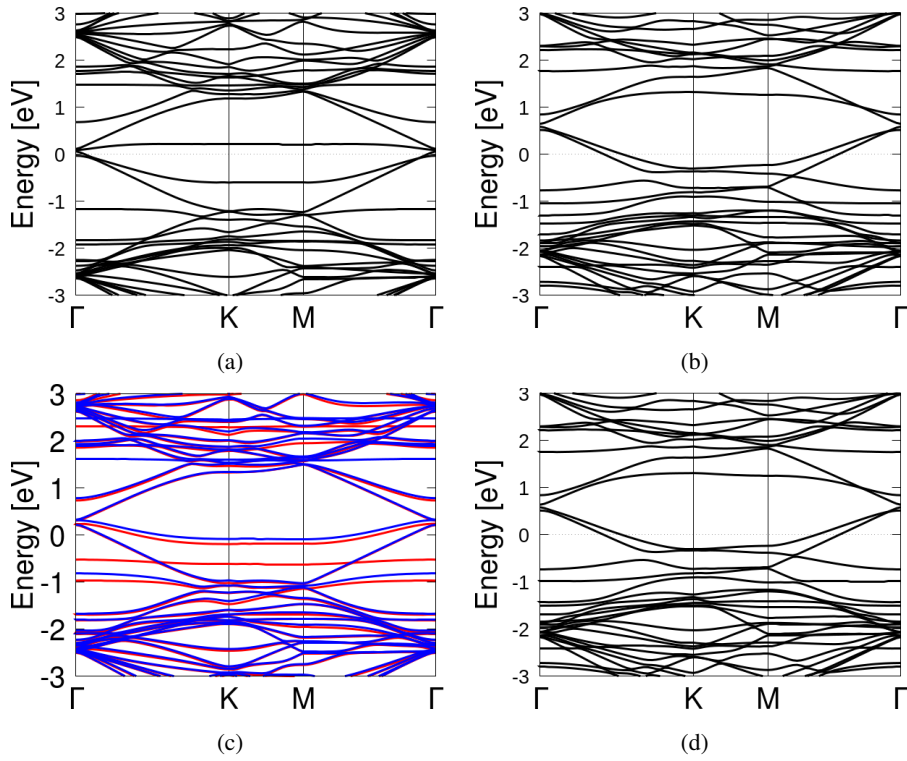


Figure 5.4: Band structure of C_6H_6 adsorption on spin-unpolarized VG (a), spin-unpolarized BVG (b), spin-polarized VG (c), and spin-polarized BVG (d).

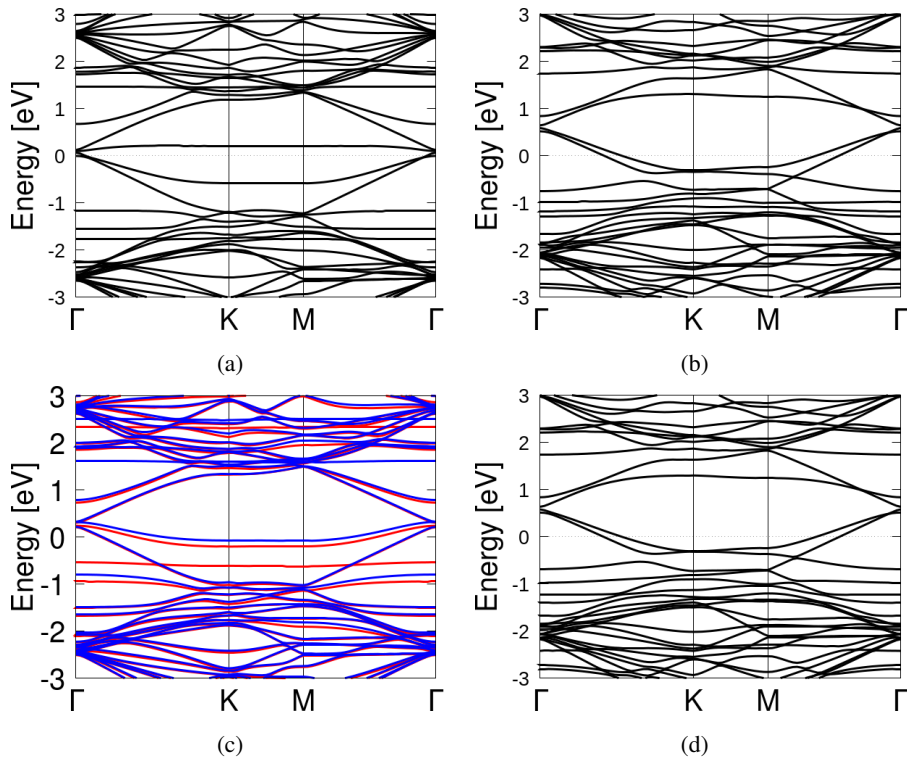


Figure 5.5: Band structure of C_7H_8 adsorption on spin-unpolarized VG (a), spin-unpolarized BVG (b), spin-polarized VG (c), and spin-polarized BVG (d).

physisorbed species where C_6H_6 donates a charge of 0.001 e to BVG while donation is 0.007 e for C_7H_8 when vdW-DF2-C09 is employed.

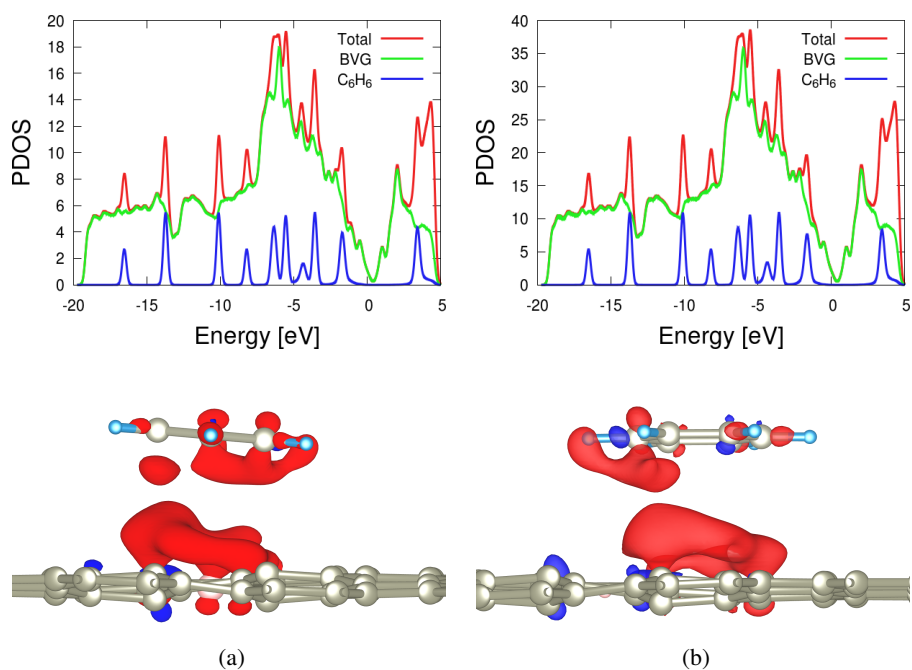


Figure 5.6: PDOS and charge density plots of C_6H_6 on spin-polarized BVG (a), and spin-unpolarized BVG (b). The isovalue is set to $\pm 0.0003 \text{ \AA}^{-3}$.

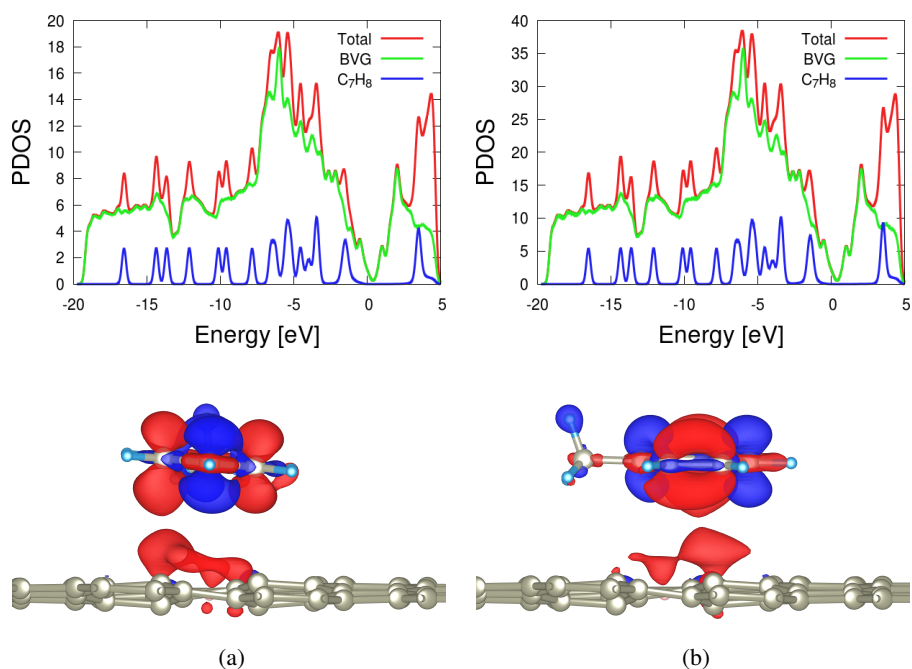


Figure 5.7: PDOS and charge density plots of C_7H_8 on spin-polarized BVG (a), and spin-unpolarized BVG (b). The isovalue is set to $\pm 0.00045 \text{ \AA}^{-3}$.

5.3.1 Fluorine Containing Benzene Derivative

As a prototype for halogen-containing benzene derivatives, we focus on the interaction of fluorobenzene (C_6H_5F) with BVG. We explore several possibilities whose initial and optimized geometries are presented in Figure 5.8.

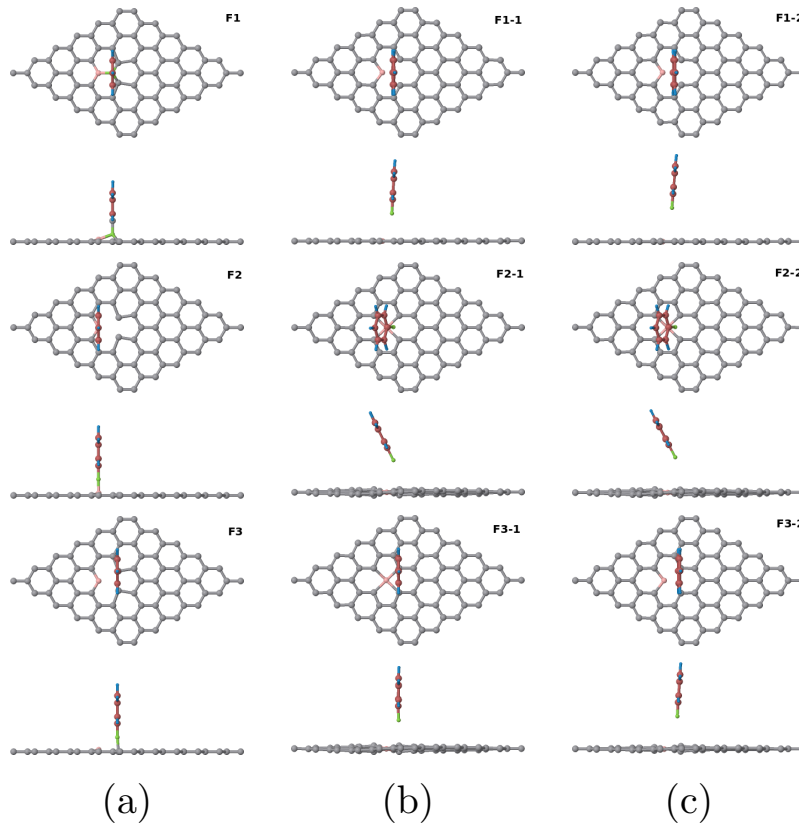


Figure 5.8: Initial (a), and optimized configurations of C_6H_5F doped BVG with vdW-DF2-C09 (b), and without vdW-DF2-C09 (c).

To probe the possibility of functionalization of graphene through covalent bonds, we generate initial configurations that could encourage covalent bonding. As seen from Figure 5.8, F-B and F-C covalent bonds are broken at the end of structure optimization calculations and C_6H_5F is non-covalently adsorbed on the BVG sheet. Furthermore, it is observed that C_6H_5F induces small degrees of curvatures on the BVG sheet resulting in a distorted structure where the distortion is more observable when vdW-DF2-C09 is used.

The adsorption heights are taken as the vertical separation of the average value in the z-direction of C coordinates in the BVG sheet and the F atom of the organic

molecule. The adsorption distances are between 2.66 Å and 3.32 Å, with adsorption energies consistent with an interaction somewhat stronger than vdW forces for a typical, perpendicularly adsorbed species but weaker than the energy of a covalent bond. This result indicates that covalent bonding for this molecule is unlikely although some level of ionic interaction is plausible. We further study a single parallel configuration where C_6H_5F is placed on BVG with the distance between F and B atoms is set to 2.70 Å. Initial and optimized geometries of parallel adsorption is presented in Figure 5.9 where the F-B distance increases to 3.30 Å with the calculations including vdW dispersion forces while it is 4.01 Å within the conventional PBE approximation. Calculated adsorption heights, adsorption energies with the magnetization values of the optimized configurations and charge transfer values are tabulated in Table 5.2. Interestingly, and in support of the ionic character of the bond in the perpendicular calculations, the adsorption energy for the parallel case is similar to some of the perpendicular cases. No tilting of the molecular plane is observed in the case of parallel configurations.

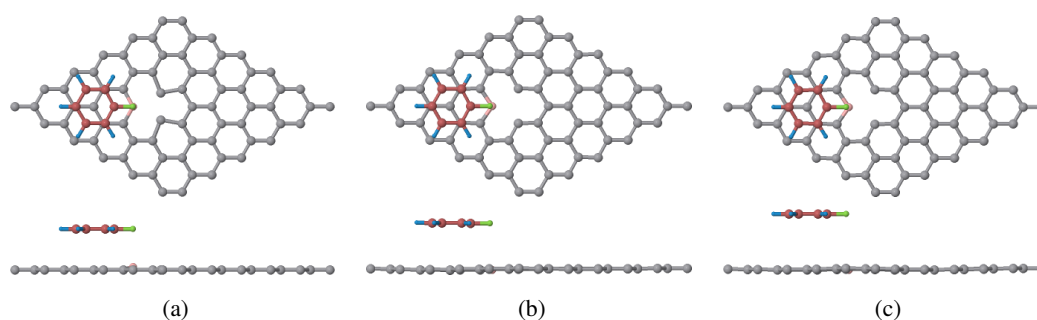


Figure 5.9: Initial (a), and optimized configuration of parallel adsorption of C_6H_5F on BVG with vdW-DF2-C09 (b), and without vdW-DF2-C09 (c).

Table 5.2: Adsorption distances, energies, magnetization (μ_B per cell) and charge transfer values of C_6H_5F on BVG.

Label	Configuration	d [Å]	E [meV]	μ_B /cell	charge transfer per molecule (e)
F1	F1-1 hollow, with vdW	2.66	197	1.18	+0.468
	F1-2 hollow, without vdW	3.25	8	0.00	+0.467
F2	F2-1 on top B, with vdW	2.87	461	0.00	+0.461
	F2-2 on top B, without vdW	3.24	346	0.00	+0.466
F3	F3-1 on top C, with vdW	2.77	481	0.00	+0.461
	F3-2 on top C, without vdW	3.32	308	0.68	+0.467
par	parallel, with vdW	3.29	355	0.00	+0.424
	parallel, without vdW	3.98	23	0.03	+0.452
adatom	with vdW	3.65	106	1.00	+0.404
	without vdW	4.98	14	0.94	+0.418

We finally explore C_6H_5F on top of B where B is positioned as an adatom close to the defect placed 1.5 \AA away from VG surface. Initial and optimized geometries are given in Figure 5.10. The resultant magnetization is $1.00 \mu_B$ per cell when vdW dispersion forces are included while it is $0.94 \mu_B$ per cell when they are excluded. After optimization, the B atom forms three C-B bonds and approaches the VG surface with distances of 0.80 \AA and 0.60 \AA for calculations including and excluding vdW interactions, respectively. During optimization, the B atom migrates downwards, into the graphene vacancy, while at the same time, the F atoms dissociates to form an B-F bond. This leaves behind a phenyl group (C_6H_5) whose adsorption energy is calculated to be 106 meV . This adsorption energy is reduced all the way down to 14 meV when vdW dispersion forces are excluded which results in a conclusion that 92 meV adsorption energy is related with vdW dispersion forces while the rest is due to the ionic interactions confirmed with the charge density difference analysis tabulated in Table 5.2

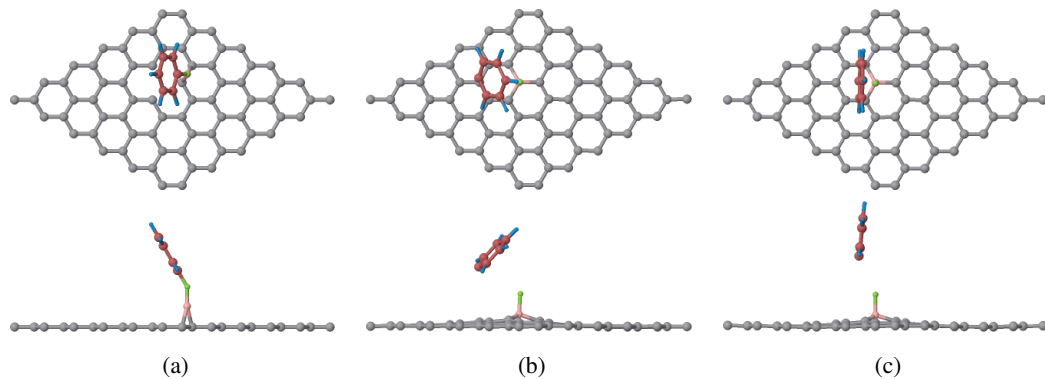


Figure 5.10: Initial (a), and optimized configuration of C_6H_5F on BVG with vdW-DF2-C09 (b), and without vdW-DF2-C09 (c) where B is doped as an adatom.

As tabulated in Table 5.2, the molecule loses electron and becomes a cation while the band gap opening shows similar characteristics with the band structure of BVG (see Figure 4.7). Additionally, the PDOS plots shown in Figure 5.11 are similar to the PDOS plot of BVG (see Figure 4.8). From the PDOS plot of adatom, it is observed that the contribution of F states to total DOS is negligible while C_6H_5 group has considerable effect.

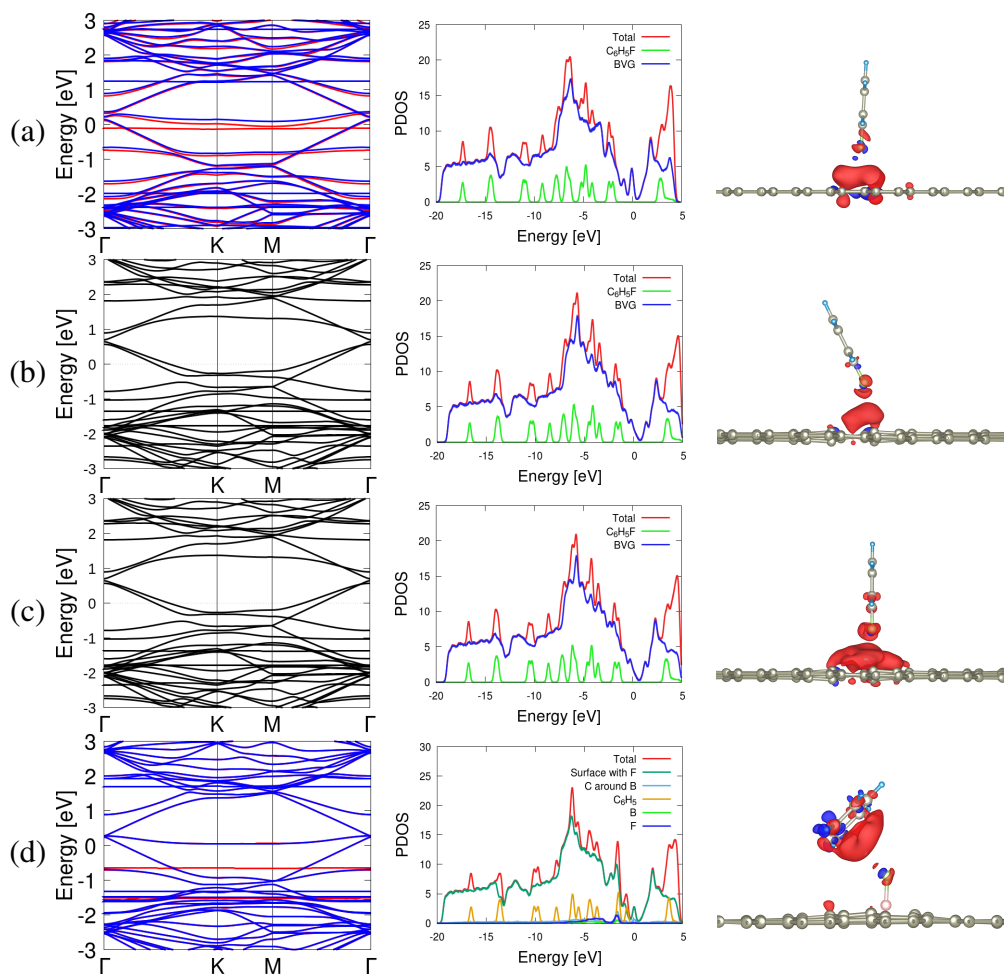


Figure 5.11: Band structure, PDOS and charge density plots of C_6H_5F on BVG with different configurations labeled as F1-1 (a), F2-1 (b), F3-1 (c), and adatom (d) where vdW dispersion forces are included. The isovalue is set to $\pm 0.0003 \text{ \AA}^{-3}$.

5.3.2 Nitrogen Containing Benzene Derivative

For nitrogen (N) containing benzene derivatives, benzonitrile (C_7H_5N) is the chosen molecule as a prototype and the interaction of the molecules with BVG is discussed in this Section. Initial and optimized geometries of C_7H_5N doped BVG are presented in Figure 5.13.

As seen from Figure 5.13, contrary to C_6H_5F on BVG, covalent N-B and N-C bonds are formed with bond distances of 1.64 \AA and 1.43 \AA , respectively. The adsorption energy is calculated to be 3.6 eV indicating the strength of covalent bonds. For the hollow site (label:N1), C_7H_5N induces distortion of sheet towards itself while the

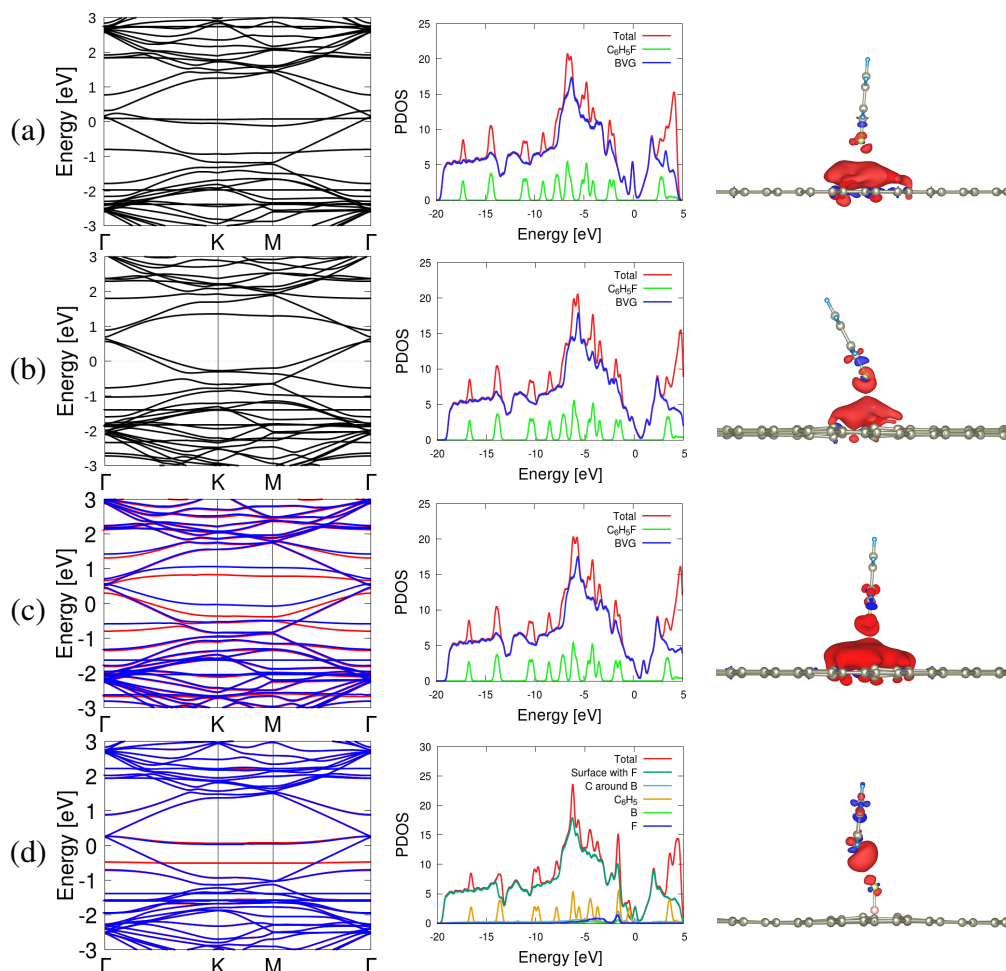


Figure 5.12: Band structure, PDOS and charge density plots of C_6H_5F on BVG with different configurations labeled as F1-2 (a), F2-2 (b), F3-2 (c), and adatom (d) where vdW dispersion forces are excluded. The isovalue is set to $\pm 0.0004 \text{ \AA}^{-3}$.

molecule approaches the substrate and tilts.

On the other hand, C_7H_5N adsorption on top of B (label:N2) resulting in out-of-plane displacement of the B atom without any broken bond in addition to the tilting of the molecule towards the plane. Calculated adsorption heights with respect to the distance between N and the surface, adsorption energies with the magnetization values of the optimized configurations are tabulated in Table 5.3.

Finally, we once again consider the adsorption of the molecule on adatom B placed 1.5 \AA away from VG surface. Initial and optimized geometries are displayed in Figure 5.14. During optimization, B atom becomes coplanar and forms three C-B bonds resulting in a configuration of B doped pristine graphene with 1.49 \AA C-B bond length

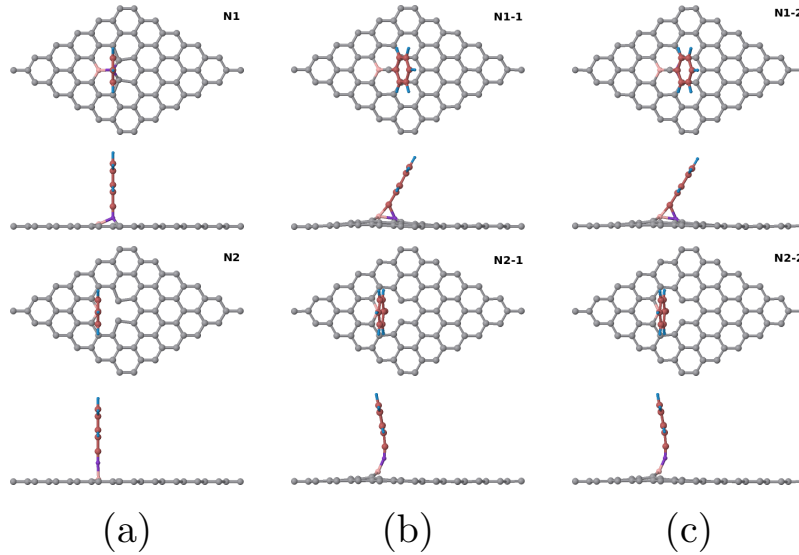


Figure 5.13: Initial (a), and optimized configurations of C₇H₅N doped BVG with vdW-DF2-C09 (b), and without vdW-DF2-C09 (c).

Table 5.3: Adsorption distances, energies and magnetization (μ_B per cell) of C₇H₅N on BVG.

Label	Configuration	d [Å]	E [meV]	μ_B /cell
N1	N1-1 hollow, with vdW	0.34	3585	0.98
	N1-2 hollow, without vdW	0.42	3220	0.98
N2	N2-1 on top B, with vdW	2.19	882	0.69
	N2-2 on top B, without vdW	2.23	99	-0.01
adatom	with vdW	3.22	82	0.00
	without vdW	3.43	5	0.00

and non-covalently adsorbed C₇H₅N while the resulting magnetization is calculated to be 0 μ_B . The adsorption heights are calculated to be 3.22 Å with 82 meV adsorption energy and 3.43 Å with 5 meV for with and without vdW dispersion forces, respectively. Furthermore, with Löwdin charge analysis, it is calculated that 0.556 e donation occurs from C₇H₅N to surface when vdW dispersion forces are included while the magnitude of charge transfer is 0.565 e for vdW excluded case. The band structure (see Figure 5.15e and 5.15f) is similar to band structure of B doped pristine graphene displayed in Figure 4.7 while in the PDOS plot, the peak around the Fermi level indicates the presence of pristine graphene structure.

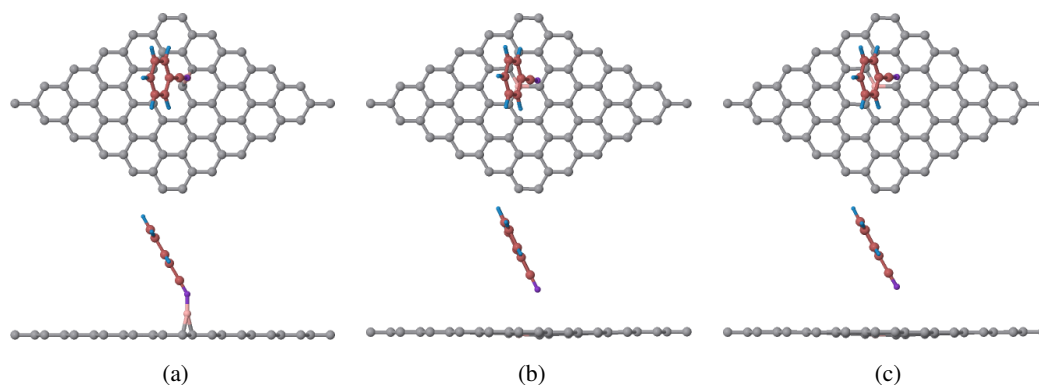


Figure 5.14: Initial (a), and optimized configuration of C_7H_5N on BVG with vdW-DF2-C09 (b), and without vdW-DF2-C09 (c) where B is doped as an adatom.

Different from previous plots, red lines in Figure 5.15d represent the minority spin while blue lines represent the majority spin since the resulting magnetization is negative as tabulated in Table 5.3. The band structure of system does not deviate significantly from the case of VG. Additionally, the isosurfaces display the characteristics of covalent bonding in the charge density difference plots displayed in Figure 5.15.

5.3.3 Oxygen Containing Benzene Derivative

Finally, benzoic acid ($C_7H_6O_2$) is chosen as a representative of oxygen (O) containing benzene derivatives. We study three configurations presented in Figure 5.16.

As seen from Figure 5.16, in the case of adsorption on the hollow site (label:O1), the O atom of $C_7H_6O_2$ detaches from the molecule, forming a bond with B and C resulting in a graphene sheet co-doped with B and O while small degrees of curvature is observed on the BVG sheet resulting in a distorted structure where the distortion is more pronounced for the vdW-DF2-C09 calculation. The benzaldehyde (C_7H_6O) fragment is left behind at an adsorption height of 2.84 Å with an adsorption energy of 579 meV in the presence of vdW forces. When vdW forces are ignored, the distance is 3.05 Å with an adsorption energy of 216 meV.

For $C_7H_6O_2$ adsorption on top of B (label:O2), the O-H bond is broken at the end of optimization and H forms a bond with the C atom of the BVG sheet with an out-of-plane displacement. VdW dispersion forces effect the direction of this displacement as H causes positive value for displacement and becomes closer to the organic dopant

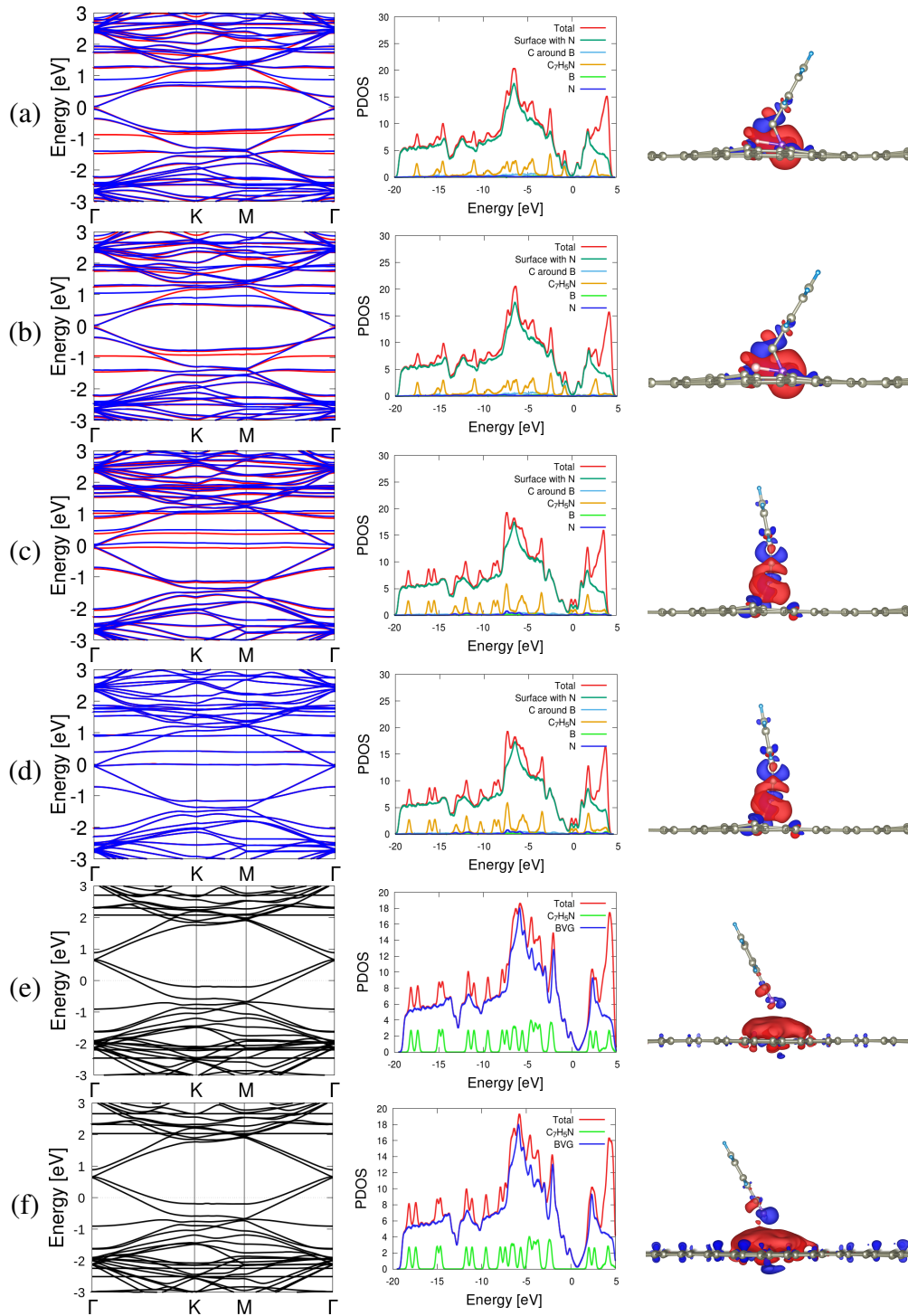


Figure 5.15: Band structure, PDOS and charge density plots of C_7H_5N on BVG with different configurations labeled as N1-1 (a), N1-2 (b), N2-1 (c), N2-2 (d), adatom (e), and adatom w/o vdW (f). The isovalue is set to $\pm 0.00015 \text{ \AA}^{-3}$.

when vdW is included while it gets far from the dopant when vdW is excluded.

Furthermore, the O-C bond is broken when $C_7H_6O_2$ is placed on top of C (label:O3)

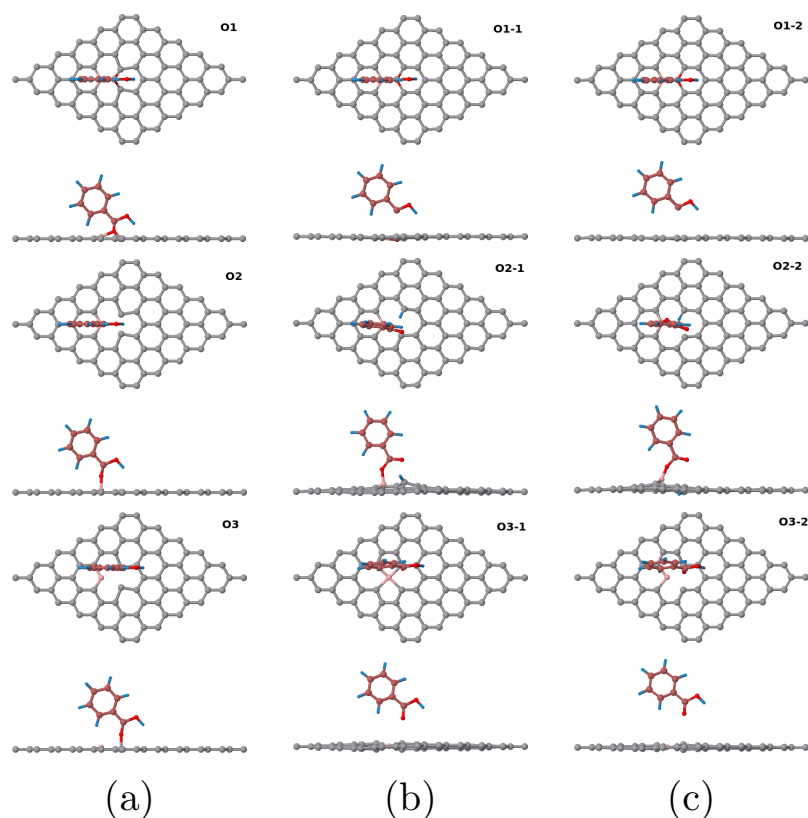


Figure 5.16: Initial (a), and optimized configurations of $C_7H_6O_2$ doped BVG with vdW-DF2-C09 (b), and without vdW-DF2-C09 (c).

and it is non-covalently adsorbed on the BVG sheet by inducing small degrees of curvatures on BVG sheet where the distortion is more apparent for vdW-DF2-C09 included geometries. The adsorption height is calculated for O1 and O3 configurations by taking vertical separation of the average value in the z-direction of C atoms in the BVG sheet and the C atom bonded to O atom of the organic molecule. Calculated adsorption distances by calculating the vertical distance between single O (not having O-H bond) and the surface (for hollow site, it is taken as the distance of broken C-O bond), adsorption energies with the magnetization values of the optimized configurations and charge transfer values are tabulated in Table 5.4. The surprisingly large difference in the spin polarization is possibly due to the existence of nearby energy minima, which increase in number when vdW interactions are introduced.

Table 5.4: Adsorption distances, energies, magnetization (μ_B per cell) and charge transfer values of $C_7H_6O_2$ on BVG.

Label	Configuration	d [Å]	E [meV]	μ_B /cell	charge transfer per molecule (e)
O1	O1-1 hollow, with vdW	2.96	579	0.00	+0.635
	O1-2 hollow, without vdW	3.14	216	0.00	+0.621
O2	O2-1 on top B, with vdW	2.09	3494	0.00	+0.616
	O2-2 on top B, without vdW	2.34	2138	1.01	+0.613
O3	O3-1 on top C, with vdW	2.66	531	0.00	+0.613
	O3-2 on top C, without vdW	3.34	310	0.68	+0.619
adatom	with vdW	2.94	155	0.00	+0.609
	without vdW	3.31	16	0.68	+0.624

Similar with the previous sections, we investigate the adsorption of $C_7H_6O_2$ on top of B. Initial and optimized geometries are given in Figure 5.17. During optimization, B atom becomes coplanar and forms three C-B bonds resulting in a configuration of B doped pristine graphene with 1.49 Å C-B bond length and non-covalently adsorbed $C_7H_6O_2$ while the resulting magnetization is calculated to be $0 \mu_B$. By calculating the vertical separation of the average value in the z-direction of C atoms in BVG sheet and the O atom closest to the BVG sheet, the adsorption height is calculated to be 2.92 Å with 16 meV adsorption energy and 3.31 Å with 155 meV when vdW dispersion forces are included and excluded, respectively.

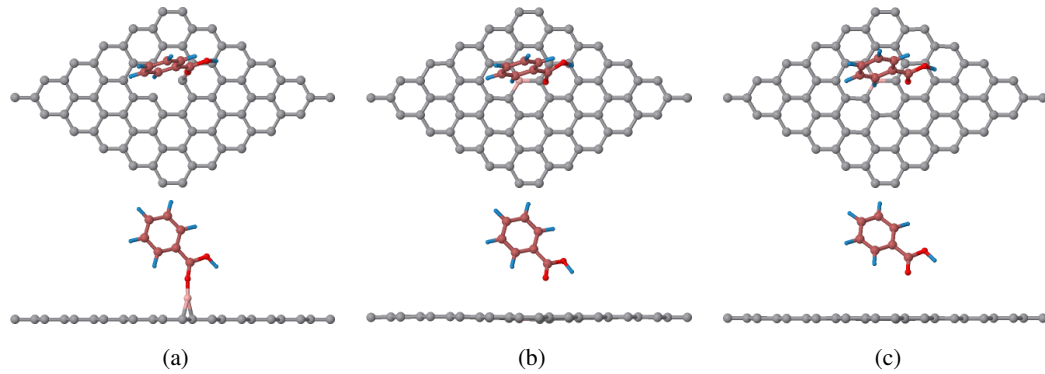


Figure 5.17: Initial (a), and optimized configuration of $C_7H_6O_2$ on BVG with vdW-DF2-C09 (b), and without vdW-DF2-C09 (c) where B is doped as an adatom.

The band structure of the system given in Figure 5.18 and Figure 5.19 does not deviate significantly from the case of VG. From the PDOS plot of hollow site, it is observed that the contribution of O being in the BVG network after the geometry optimization to total DOS is negligible while C_7H_6O has considerable effect.

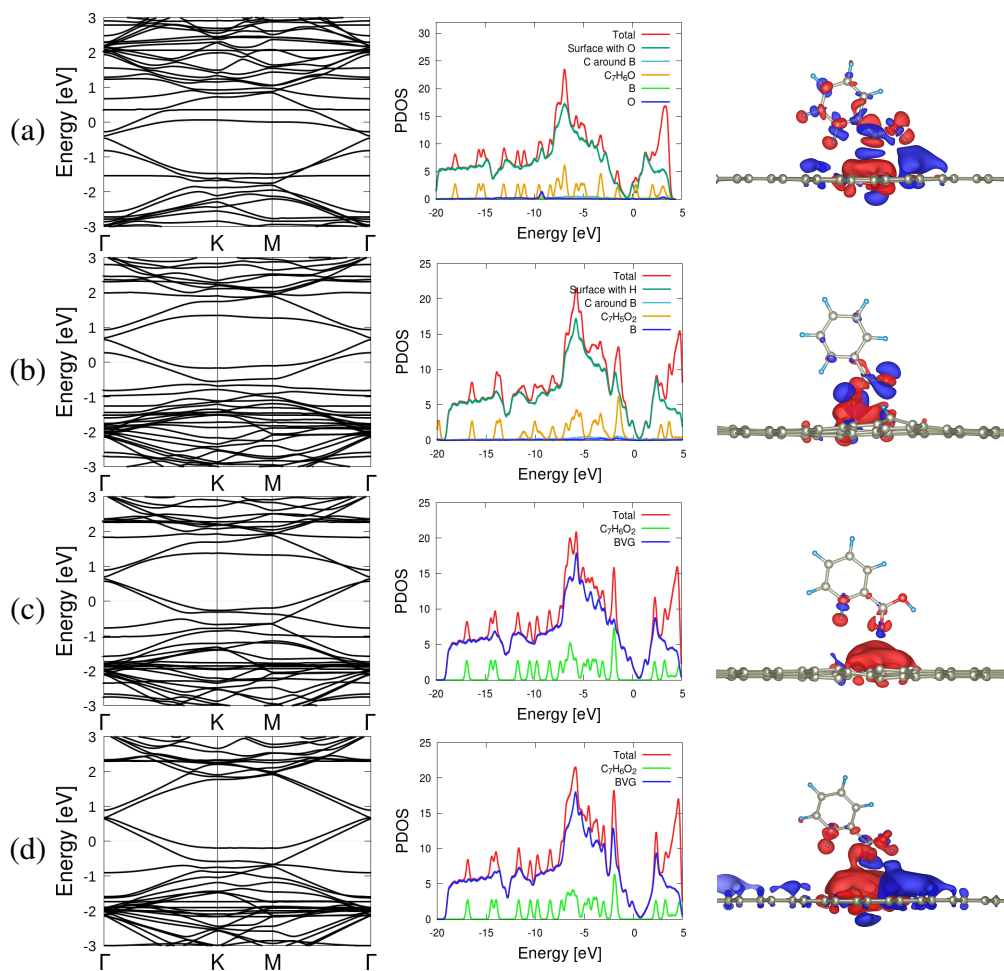


Figure 5.18: Band structure, PDOS and charge density plots of $C_7H_6O_2$ on BVG with different configurations labeled as O1-1 (a), O2-1 (b), O3-1 (c), and adatom (d) where vdW dispersion forces are included. The isovalue is set to $\pm 0.00025 \text{ \AA}^{-3}$.

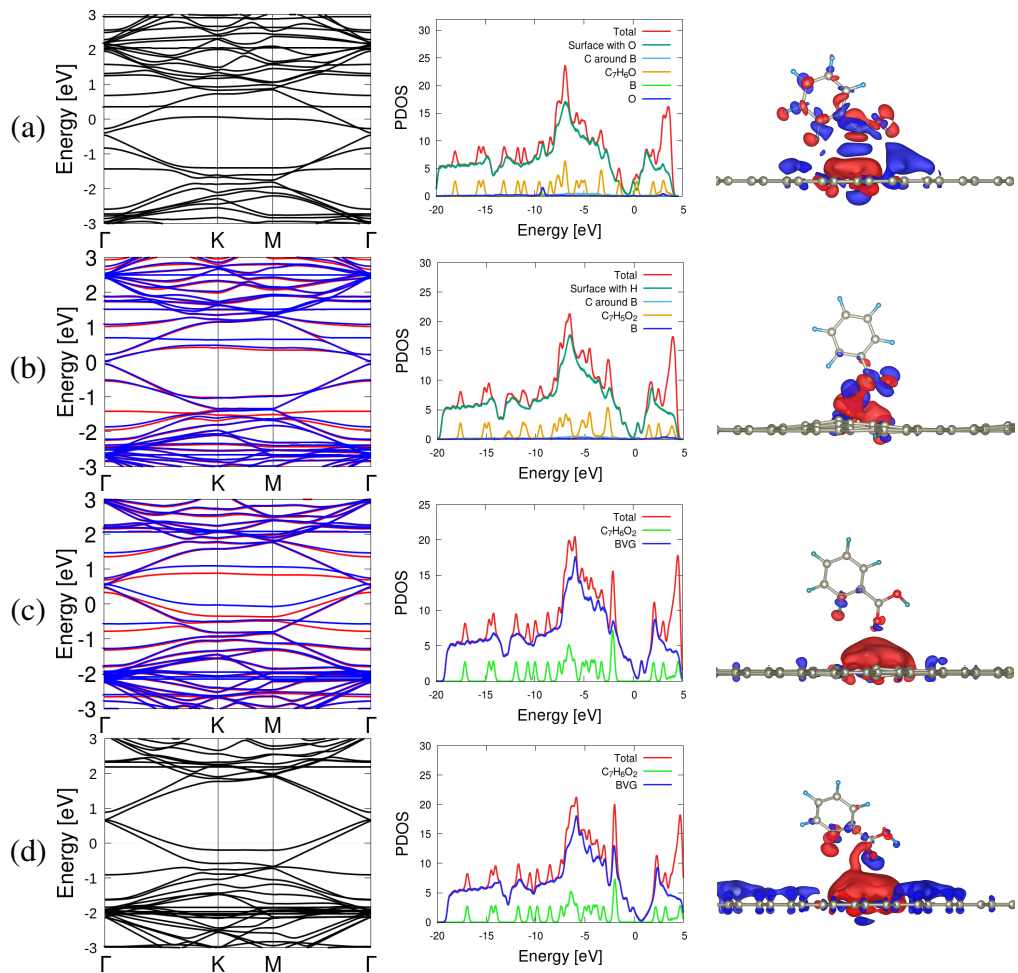


Figure 5.19: Band structure, PDOS and charge density plots of $C_7H_6O_2$ on BVG with different configurations labeled as O1-2 (a), O2-2 (b), O3-2 (c), and adatom (d) where vdW dispersion forces are excluded. The isovalue is set to $\pm 0.00012 \text{ \AA}^{-3}$.

CHAPTER 6

CONCLUSION

In this thesis, we present a density functional theory investigation of graphene functionalization by means of doping, introduction of defects and adsorbates. We explore the complex interplay between defects, dopants and adsorption of organic molecules. To test our calculation parameters, we perform a series of benchmark calculations where we examine the structural and electronic properties of graphene. For pristine graphene (PG), the bond length is calculated to be 1.4215 Å with very little variation between different exchange-correlation functionals. For vacancy-defected graphene (VG), one of the C atoms surrounding the vacancy undergoes an out of plane displacement of about 0.7 Å resulting in a distorted structure while the remaining two atoms surrounding the vacancy are at a distance of 2.1 Å. The Fermi point appears at the Γ point due to zone folding of PG and for VG, spin polarization lifts the degeneracies while the Fermi level is depressed below the original location similarly with divacancy-defected graphene (DG).

In the first chapter, the adsorption characteristics of benzene (C_6H_6) and toluene (C_7H_8) on PG, VG and DG are explored. In order to see the effect of different vdW corrections and functionals on adsorption geometry, adsorption energy and band structure, two different vdW functionals are used, namely vdW-DF, vdW-DF2-C09 and one vdW correction is used, namely Grimme-D2. Several configurations are explored to determine the most stable sites and after optimization it is observed that the preferred geometry of C_6H_6 and C_7H_8 molecule on graphene is a parallel configuration for all exchange-correlation functionals. In its optimized structure, C_6H_6 is located at a distance of 3.30 Å away from PG and the adsorption energy is 441 meV

while C_7H_8 is located at a distance of 2.93 Å and the adsorption energy is 498 meV within vdW-DF2-C09. The results indicate that vdW-DF2-C09 exchange-correlation protocol for the vdW interactions produces the closest agreement with literature.

In preliminary calculations, resulting magnetization of VG is calculated to be 1.43 μ_B per cell where the unsaturated atom is 0.07 Å above the graphene plane when vdW dispersion forces are excluded. For DG, it is observed that total magnetization is equal to 0.00 μ_B per cell concluding that there is no effect of magnetization for divacancy in graphene sheet. For the VG/ C_6H_6 system, total magnetization is equal to 0.69 μ_B , 1.27 μ_B and 1.40 μ_B per cell for spin-polarized vdW-DF, vdW-DF2-C09 and Grimme-D2, respectively while total magnetization of C_7H_8 /VG is equal to 0.68 μ_B , 1.31 μ_B and 1.45 μ_B per cell for spin polarized vdW-DF, vdW-DF2-C09 and Grimme-D2, respectively.

The band structure for the non-covalent interaction of molecule with substrate reveals no deviation around the K-point from the substrate's band structure. From the Bader charge analysis, the charge transfer between the substrate and the molecule is calculated to be negligibly small for the physisorbed species while substrate acts as an electron acceptor.

Using vdW-DF, vdW-DF2-C09 and Grimme-D2, C_6H_6 and C_7H_8 are adsorbed on bilayer graphene separately in order to investigate the effects of number of layers on adsorption characteristics. While band structure, PDOS and charge density difference plots show similar characteristics to those of the single layer, this study reveals an interesting fact that the presence of the second layer increases the adsorption energy by approximately 70 meV for both molecules when vdW-DF2-C09 is used.

In the second chapter, one or two B atoms are combined with a single and divacancy configurations in a 6x6 graphene unit cell for extending the degree of control over functionalization. For B-doped vacancy-defected graphene (BVG), the resulting magnetization is about 0.9 μ_B per cell and the B atom is only 0.01 Å elevated with respect to the surface while it is 0 μ_B for B-doped divacancy-defected graphene (BDG). Furthermore, formation energies of BVG and BDG are calculated to be -2.99 eV and -2.25 eV with gaseous B and graphene are taken as reference systems. With the introduction of B, VG and DG becomes positively doped and band structure has an

upward shift while the band gap opening increases with increased concentration of B. and for B doping as an adatom, the band structure is similar to the band structure of bare PG with Fermi level being shifted downwards.

For B introduced as an adatom, the resultant geometry is BVG with three different C-B bond lengths of 1.51, 1.58 and 1.61 Å in addition to small shanges in C-C bond lengths and positions of C around the defect. Furthermore, from the magnetic property analysis, it is observed that state of the BVG-adatom changes and shows a similar trend to BVG for magnetization greater than 1 μ_B per cell, state of the BVG-adatom changes and show similar trend with BVG.

Finally, to further enhance our understanding of functionalization C_6H_6 , C_7H_8 , fluoro benzene (C_6H_5F), benzonitrile (C_7H_5N), and benzoic acid ($C_7H_6O_2$) on the B-doped defected sheets. C_6H_6 and C_7H_8 are adsorbed on BVG in order to serve as a comparison to the adsorption taking place on VG. The adsorption energy of C_6H_6 is calculated to be 776 meV on BVG while it is 391 meV on VG. For C_7H_8 , these energy values are 819 meV and 425 meV on BVG and VG, respectively. These findings gives conclusion as B causes increased adsorption energy by the additional organic molecule–B interaction (an increase of 380-390 meV) with respect to bare VG. Furthermore, B doping on VG results in decreased curvature effect.

Other molecules are investigated on the hollow site, on top of a B atom and on top of a C atom. In case of C_6H_5F , F-B and F-C covalent bonds are broken at the end of structure optimization calculations and C_6H_5F is non-covalently adsorbed on the BVG sheet with weak vdW interactions. When C_6H_5F on top of B where B is positioned as an adatom, the resultant magnetization is 1.00 μ_B per cell when vdW dispersion forces are included and the B atom forms three C-B bonds approaching the VG surface with distances of 0.80 Å. The optimization leaves behind a phenyl group (C_6H_5) whose adsorption energy is calculated to be 106 meV. This value is 14 meV when vdW dispersion forces are excluded which results in a conclusion that 92 meV adsorption energy is related with vdW dispersion forces while the rest is due to the ionic interactions confirmed with the charge density difference analysis as 0.404 e donation occurs from the molecule to the surface.

C_7H_5N molecules are observed to form strong covalent bonds with an adsorption

energy of 3.6 eV for the hollow site when vdW dispersion forces are included. When the molecule is adsorbed on an B adatom, B atom becomes coplanar and forms three C-B bonds resulting in a configuration of B doped pristine graphene with 1.49 Å C-B bond length and non-covalently adsorbed C_7H_5N cation with 82 meV adsorption energy while in the PDOS plot, the peak around the Fermi level indicates the presence of pristine graphene structure. The resulting magnetization is calculated to be $0 \mu_B$.

Finally, $C_7H_6O_2$ is adsorbed on BVG and after optimization, it is found to adsorb through weak vdW interactions. In the case of adsorption on the hollow site, benzaldehyde (C_7H_6O) fragment is formed with an adsorption energy of 579 meV in the presence of vdW forces with the detachment of O atom and surface becomes graphene sheet co-doped with B and O. For $C_7H_6O_2$ adsorption on top of B, O-H bond is broken at the end of optimization and H forms a bond with the C atom of the BVG sheet with an out-of-plane displacement. VdW dispersion forces effect the direction of this displacement as H causes positive value for displacement and becomes closer to the organic dopant when vdW is included while it gets far from the dopant when vdW is excluded. For all molecules being adsorbed on BVG, the band structure of system does not deviate significantly from the case of VG.

The systematic investigation presented in this thesis that combines different functionalization methods that may enhance or reduce the effects of one another thereby creating the possibility of finer control of the band structure. The immense variety of dopants, defects and adsorbates can be combined to produce endless possibilities for various applications relying on band gap engineering. As evidenced in the sections on bilayer and B-doped defective graphene, the electronic and structural properties of the substrate change the physics of the problem quite remarkably. This fact can motivate the extension of the substrates investigated here to different systems such as nanotubes and other two-dimensional materials.

REFERENCES

- [1] Zhuang Liu, Joshua T. Robinson, Scott M. Tabakman, Kai Yang, and Hongjie Dai. Carbon materials for drug delivery & cancer therapy. *Materials Today*, 14(7-8):316–323, 2011.
- [2] Gaurav Singh, Anshul Choudhary, D. Haranath, Amish G. Joshi, Nahar Singh, Sukhvir Singh, and Renu Pasricha. ZnO decorated luminescent graphene as a potential gas sensor at room temperature. *Carbon*, 50(2):385–394, 2012.
- [3] Chen-Chia Huang, Nen-Wen Pu, Chung-An Wang, Jhin-Cin Huang, Yuh Sung, and Ming-Der Ger. Hydrogen storage in graphene decorated with pd and pt nano-particles using an electroless deposition technique. *Separation and Purification Technology*, 82:210 – 215, 2011.
- [4] A. Sigal, M.I. Rojas, and E.P.M. Leiva. Interferents for hydrogen storage on a graphene sheet decorated with nickel: A {DFT} study. *International Journal of Hydrogen Energy*, 36(5):3537 – 3546, 2011.
- [5] Virendra Singh, Daeha Joung, Lei Zhai, Soumen Das, Saiful I. Khondaker, and Sudipta Seal. Graphene based materials: Past, present and future. *Progress in Materials Science*, 56(8):1178–1271, 2011.
- [6] Valeria Verdinelli, Estefanía Germán, Carla R. Luna, Jorge M. Marchetti, María a. Volpe, and Alfredo Juan. Theoretical study of hydrogen adsorption on Ru-decorated (8,0) single-walled carbon nanotube. *The Journal of Physical Chemistry C*, 118(48):27672–27680, 2014.
- [7] Karri Saloriotta. Electron transport in graphene nanostructures. (*Doctoral dissertation, Aalto University, Department of Applied Physics.*), 2009.
- [8] Vasilios Georgakilas, Michal Otyepka, Athanasios B. Bourlinos, Vimlesh Chandra, Namdong Kim, K. Christian Kemp, Pavel Hobza, Radek Zboril, and Kwang S. Kim. Functionalization of graphene: covalent and non-covalent approaches, derivatives and applications. *Chemical Reviews*, 112(11):6156–6214, 2012.
- [9] L A Ponomarenko, F Schedin, M I Katsnelson, R Yang, E W Hill, K S Novoselov, and a K Geim. Chaotic Dirac billiard in graphene quantum dots. *Science*, 320(5874):356–358, 2008.

- [10] Melinda Y. Han, Barbaros Ozyilmaz, Yuanbo Zhang, and Philip Kim. Energy band-gap engineering of graphene nanoribbons. *Physical Review Letters*, 98(20):1–4, 2007.
- [11] Eric Pop, Vikas Varshney, and Ajit K. Roy. Thermal properties of graphene: Fundamentals and applications. *MRS Bulletin*, 37(12):1273–1281, 2012.
- [12] Young Woo Son, Marvin L. Cohen, and Steven G. Louie. Energy gaps in graphene nanoribbons. *Physical Review Letters*, 97(21):1–4, 2006.
- [13] J. Fernandez-Rossier and J. J. Palacios. Magnetism in graphene nanoislands. *Physical Review Letters*, 99(17):1–5, 2007.
- [14] Mikhail G. Brik Veera Krasnenko, Jaak Kikas. Modification of the structural and electronic properties of graphene by the benzene molecule adsorption. *Physica B: Condensed Matter*, 407(23):1–4, 2012.
- [15] K. S. Novoselov, A. K. Geim, S.V. Morozov, D. Jiang, Y. Zhang, S. V. Dubonos, I. V. Grigorieva, and A. A. Firsov. Electric Field Effect in Atomically Thin Carbon Films. *Science*, 306(5696):666–669, 2004.
- [16] Ya-nan Guo, Xiong Lu, Jie Weng, and Yang Leng. Density functional theory study of the interaction of arginine-glycine-aspartic acid with graphene, defective graphene, and graphene oxide. *J. Phys. Chem. C*, 117(11):5708–5717, 2013.
- [17] H. Shioyama. Cleavage of graphite to graphene. *Journal of Materials Science Letters*, 20(6):499–500, 2001.
- [18] L D Landau and E M Lifshitz. Course of Theoretical Physics: Statistical Physics Part 2, 1980.
- [19] Guihua Li, Feng Li, Xiaopeng Wang, Mingwen Zhao, and Xiangdong Liu. Gold atom and dimer adsorbed on perfect and defective graphene and boron nitride monolayer: A first-principles study. *Physica E: Low-Dimensional Systems and Nanostructures*, 59:235–242, 2014.
- [20] Mohamed Hassan, Michael Walter, and Michael Moseler. Interactions of polymers with reduced graphene oxide: van der Waals binding energies of benzene on graphene with defects. *Physical chemistry chemical physics : PCCP*, 16(1):33–7, 2014.
- [21] P. R. Wallace. The band theory of graphite. *Phys. Rev.*, 71:622–634, May 1947.
- [22] Liping Chen, Linjun Wang, Zhigang Shuai, and David Beljonne. Energy Level Alignment and Charge Carrier Mobility in Noncovalently Functionalized Graphene. *The Journal of Physical Chemistry Letters*, 2013.

- [23] Y. G. Zhang, H. Y. He, and B. C. Pan. Structural features and electronic properties of MgO nanosheets and nanobelts. *Journal of Physical Chemistry C*, 116(43):23130–23135, 2012.
- [24] Ping Wu, Min Huang, Wenjing Cheng, and Fuling Tang. First-principles study of B, C, N and F doped graphene-like MgO monolayer. *Physica E: Low-Dimensional Systems and Nanostructures*, 81:7–13, 2016.
- [25] Paulo T. Araujo, Mauricio Terrones, and Mildred S. Dresselhaus. Defects and impurities in graphene-like materials. *Materials Today*, 15(3):98–109, 2012.
- [26] K.I. Bolotin, K.J. Sikes, Z. Jiang, M. Klima, G. Fudenberg, J. Hone, P. Kim, and H.L. Stormer. Ultrahigh electron mobility in suspended graphene. *Solid State Communications*, 146(9–10):351 – 355, 2008.
- [27] Denis Kochan, Martin Gmitra, and Jaroslav Fabian. Spin relaxation mechanism in graphene: Resonant scattering by magnetic impurities. *Phys. Rev. Lett.*, 112:116602, Mar 2014.
- [28] T. O. Wehling, S. Yuan, A. I. Lichtenstein, A. K. Geim, and M. I. Katsnelson. Resonant scattering by realistic impurities in graphene. *Phys. Rev. Lett.*, 105:056802, Jul 2010.
- [29] S.V. Morozov, K.S. Novoselov, M.I. Katsnelson, F. Schedin, D.C. Elias, J.A. Jaszczak, and A.K. Geim. Giant intrinsic carrier mobilities in graphene and its bilayer. *Physical Review Letters*, 100(1):016602, 2008.
- [30] Cheng-Cheng Liu, Wanxiang Feng, and Yugui Yao. Quantum spin hall effect in silicene and two-dimensional germanium. *Phys. Rev. Lett.*, 107:076802, Aug 2011.
- [31] Y. B. Zhang, Y. W. Tan, Horst L Stormer, and Philip Kim. Experimental observation of the quantum Hall effect and Berry’s phase in graphene. *Nature*, 438(7065):201–204, 2005.
- [32] J Scott Bunch, Yuval Yaish, Markus Brink, Kirill Bolotin, and Paul L Mceuen. Coulomb oscillations and Hall effect in quasi-2d graphite quantum dots. *Nano Lett.*, 5(2):287, 2005.
- [33] DW Boukhvalov and MI Katsnelson. Chemical functionalization of graphene. *Journal of Physics: Condensed Matter*, 21(34):344205, 2009.
- [34] A. H. Castro Neto, F. Guinea, N. M R Peres, K. S. Novoselov, and A. K. Geim. The electronic properties of graphene. *Reviews of Modern Physics*, 81(1):109–162, 2009.
- [35] N. M R Peres. The electronic properties of graphene and its bilayer. *Vacuum*, 83(10):1248–1252, 2009.

- [36] E R Mucciolo and C H Lewenkopf. Disorder and electronic transport in graphene. *Journal of Physics. Condensed matter : an Institute of Physics Journal*, 22(27):273201, 2010.
- [37] F Schedin, A Geim, S V Morozov, E W Hill, P Blake, M I Katsnelson, and K S Novoselov. Detection of individual gas molecules adsorbed on graphene. *Nature materials*, 6(9):652–5, 2007.
- [38] J.-H. Chen, C. Jang, S. Adam, M. S. Fuhrer, E. D. Williams, and M. Ishigami. Charged-impurity scattering in graphene. *Nature Physics*, 4(5):377–381, 2008.
- [39] Xinran Wang, Scott M. Tabakman, and Hongjie Dai. Atomic layer deposition of metal oxides on pristine and functionalized graphene. *Journal of the American Chemical Society*, 130(26):8152–8153, 2008.
- [40] Changgu Lee, Xiaoding Wei, Jeffrey W Kysar, and James Hone. Measurement of the elastic properties and intrinsic strength of monolayer graphene. *Science (New York, N.Y.)*, 321(5887):385–388, 2008.
- [41] Alexander A. Balandin, Suchismita Ghosh, Wenzhong Bao, Irene Calizo, Desalegne Teweldebrhan, Feng Miao, and Chun Ning Lau. Superior thermal conductivity of single-layer graphene. *Nano Letters*, 8(3):902–907, 2008. PMID: 18284217.
- [42] S. Ansari and E. P. Giannelis. Functionalized graphene sheet—poly(vinylidene fluoride) conductive nanocomposites. *Journal of Polymer Science Part B: Polymer physics*, 45(April):1390–1398, 2009.
- [43] A. Elsagh. Enhanced electrical conductivity properties of graphene oxide nanocomposites functionalized with polyvinyl alcohol. *International Journal of Nano Dimension*, 5(5):447–451, 2014.
- [44] D. Jiang Novoselov, K. S. E. McCann, S. V. Morozov, V. I. Falko, M. I. Katsnelson, A. K. Geim, F. Schedin. Unconventional quantum hall effect and Berry’s phase of 2π in bilayer graphene. *Nature Physics*, 2(3):177–180, 2006.
- [45] Kaoru Kanayama and Kosuke Nagashio. Gap state analysis in electric-field-induced band gap for bilayer graphene. *Nature Publishing Group*, pages 1–9, 2015.
- [46] Ian K Snook and Amanda S Barnard. Theory , Experiment and Applications of Graphene Nano-Flakes. *Nanotechnology and Nanomaterials : "Physics and Applications of Graphene - Theory"*, 2011.
- [47] D.S.L. Abergel, V. Apalkov, J. Berashevich, K. Ziegler, and Tapash Chakraborty. Properties of graphene: a theoretical perspective. *Advances in Physics*, 59(4):261–482, 2010.

- [48] Y Zhang, T T Tang, C Girit, Z Hao, M C Martin, A Zettl, M F Crommie, Y R Shen, and F Wang. Direct observation of a widely tunable bandgap in bilayer graphene. *Nature*, 459(7248):820–823, 2009.
- [49] Miguel M. Ugeda, Iván Brihuega, Fanny Hiebel, Pierre Mallet, Jean Yves Veuillen, José M. Gómez-Rodríguez, and Félix Ynduráin. Electronic and structural characterization of divacancies in irradiated graphene. *Physical Review B - Condensed Matter and Materials Physics*, 85(12):2–6, 2012.
- [50] V J Surya, K Iyakutti, H Mizuseki, and Y Kawazoe. Tuning Electronic Structure of Graphene : A First-principle Study. *IEEE Transactions on Nanotechnology*, 11(3):534–541, 2012.
- [51] Ovidiu Cretu, Arkady V. Krasheninnikov, Julio A. Rodríguez-Manzo, Litao Sun, Risto M. Nieminen, and Florian Banhart. Migration and localization of metal atoms on strained graphene. *Physical Review Letters*, 105(19), 2010.
- [52] Oleg V. Yazyev and Lothar Helm. Defect-induced magnetism in graphene. *Phys. Rev. B*, 75:125408, Mar 2007.
- [53] Yuchen Ma, P O Lehtinen, A S Foster, and R M Nieminen. Magnetic properties of vacancies in graphene and single-walled carbon nanotubes. *New Journal of Physics*, 6(1):68, 2004.
- [54] Biplab Sanyal, Olle Eriksson, Ulf Jansson, and Helena Grennberg. Molecular adsorption in graphene with divacancy defects. *Phys. Rev. B*, 79:113409, Mar 2009.
- [55] Xianqi Dai, Yanhui Li, Maohai Xie, Gongchen Hu, Jianhua Zhao, and Bao Zhao. Structural stability and electronic, magnetic properties of ge adsorption on defected graphene: a first-principles study. *Physica E: Low-dimensional Systems and Nanostructures*, 43(8):1461 – 1464, 2011.
- [56] Qingxiao Zhou, Zhibing Fu, Yongjian Tang, Hong Zhang, and Chaoyang Wang. First-principle study of the transition-metal adatoms on B-doped vacancy-defected graphene. *Physica E: Low-Dimensional Systems and Nanostructures*, 60:133–138, 2014.
- [57] L. S. Panchakarla, K. S. Subrahmanyam, S. K. Saha, Achutharao Govindaraj, H. R. Krishnamurthy, U. V. Waghmare, and C. N R Rao. Synthesis, structure, and properties of boron- and nitrogen-doped graphene. *Advanced Materials*, 21(46):4726–4730, 2009.
- [58] Z S Wu, W Ren, L Xu, F Li, and H M Cheng. Doped graphene sheets as anode materials with superhigh rate and large capacity for lithium ion batteries. *Acc Nano*, 5(7):5463–5471, 2011.

- [59] A Hussain, S Ullah, and MA Farhan. Fine tuning of band-gap of graphene by atomic and molecular doping: A density functional theory study. *RSC Advances*, 6:55990–56003, 2016.
- [60] X Wang, G Sun, P Routh, D H Kim, W Huang, and P Chen. Heteroatom-doped graphene materials: syntheses, properties and applications. *Chem Soc Rev*, 43(20):7067–7098, 2014.
- [61] D C Wei, Y Q Liu, Y Wang, H L Zhang, L P Huang, and G Yu. Synthesis of N-Doped Graphene by Chemical Vapor Deposition and Its Electrical Properties. *Nano Lett.*, 9:1752, 2009.
- [62] Palash Nath, Suman Chowdhury, D. Sanyal, and Debnarayan Jana. Ab-initio calculation of electronic and optical properties of nitrogen and boron doped graphene nanosheet. *Carbon*, 73:275–282, 2014.
- [63] Jiahua Zhu, Minjiao Chen, Qingliang He, Lu Shao, Suying Wei, and Zhanhu Guo. An overview of the engineered graphene nanostructures and nanocomposites. *RSC Advances*, 3(45):22790, 2013.
- [64] Yong-Hui Zhang, Li-Feng Han, Yuan-Hua Xiao, Dian-Zeng Jia, Zhan-Hu Guo, and Feng Li. Understanding dopant and defect effect on {H₂S} sensing performances of graphene: A first-principles study. *Computational Materials Science*, 69:222 – 228, 2013.
- [65] D. W. Boukhvalov. DFT modeling of the covalent functionalization of graphene: from ideal to realistic models. *RSC Advances*, 3(20):7150, 2013.
- [66] D. W. Boukhvalov. Tuneable molecular doping of corrugated graphene. *Surface Science*, 604(23-24):2190–2193, 2010.
- [67] Jin-Ho Choi, Zhancheng Li, Ping Cui, Xiaodong Fan, Hui Zhang, Changgan Zeng, and Zhenyu Zhang. Drastic reduction in the growth temperature of graphene on copper via enhanced London dispersion force. *Scientific reports*, 3:1925, 2013.
- [68] Yuliang Mao, G. Malcolm Stocks, and Jianxin Zhong. First-principles study of the doping effects in bilayer graphene. *New Journal of Physics*, 12, 2010.
- [69] Lingmei Kong, Axel Enders, Talat S Rahman, and Peter a Dowben. Molecular adsorption on graphene. *Journal of physics. Condensed matter : an Institute of Physics journal*, 26(44):443001, 2014.
- [70] O. Leenaerts, B. Partoens, and F. M. Peeters. Adsorption of h₂O, Nh₃, co, No₂, and no on graphene: A first-principles study. *Phys. Rev. B*, 77:125416, Mar 2008.

- [71] Tapas Kuila, Saswata Bose, Ananta Kumar Mishra, Partha Khanra, Nam Hoon Kim, and Joong Hee Lee. Chemical functionalization of graphene and its applications. *Progress in Materials Science*, 57(7):1061–1105, 2012.
- [72] H Pinto, R Jones, J P Goss, and P R Briddon. p-type doping of graphene with f4-tcnq. *Journal of Physics: Condensed Matter*, 21(40):402001, 2009.
- [73] X. Q. Tian, J. B. Xu, and X. M. Wang. Self-assembly of ptcda ultrathin films on graphene: Structural phase transition and charge transfer saturation. *The Journal of Physical Chemistry C*, 114(49):20917–20924, 2010.
- [74] C. Coletti, C. Riedl, D. S. Lee, B. Krauss, L. Patthey, K. von Klitzing, J. H. Smet, and U. Starke. Charge neutrality and band-gap tuning of epitaxial graphene on sic by molecular doping. *Phys. Rev. B*, 81:235401, Jun 2010.
- [75] Mingsheng Xu, Daisuke Fujita, and Nobutaka Hanagata. Perspectives and challenges of emerging single-molecule dna sequencing technologies. *Small*, 5(23):2638–2649, 2009.
- [76] Henk W. Ch. Postma. Rapid sequencing of individual dna molecules in graphene nanogaps. *Nano Letters*, 10(2):420–425, 2010. PMID: 20044842.
- [77] Grégory F. Schneider, Stefan W. Kowalczyk, Victor E. Calado, Grégory Pandraud, Henny W. Zandbergen, Lieven M. K. Vandersypen, and Cees Dekker. Dna translocation through graphene nanopores. *Nano Letters*, 10(8):3163–3167, 2010. PMID: 20608744.
- [78] Christopher A. Merchant, Ken Healy, Meni Wanunu, Vishva Ray, Neil Pterman, John Bartel, Michael D. Fischbein, Kimberly Venta, Zhengtang Luo, A. T. Charlie Johnson, and Marija Drndić. Dna translocation through graphene nanopores. *Nano Letters*, 10(8):2915–2921, 2010. PMID: 20698604.
- [79] S Garaj, W Hubbard, a Reina, J Kong, D Branton, and J a Golovchenko. Graphene as a subnanometre trans-electrode membrane. *Nature*, 467(7312):190–193, 2010.
- [80] Duy Le, Abdelkader Kara, Elsebeth Schröder, Per Hyldgaard, and Talat S Rahman. Physisorption of nucleobases on graphene: a comparative van der waals study. *Journal of Physics: Condensed Matter*, 24(42):424210, 2012.
- [81] Yeonchoo Cho, Seung Kyu Min, Jeonghun Yun, Woo Youn Kim, Alexandre Tkatchenko, and Kwang S. Kim. Noncovalent interactions of dna bases with naphthalene and graphene. *Journal of Chemical Theory and Computation*, 9(4):2090–2096, 2013. PMID: 26583555.
- [82] S. Gowtham, Ralph H. Scheicher, Rajeev Ahuja, Ravindra Pandey, and Shashi P. Karna. Physisorption of nucleobases on graphene: Density-functional calculations. *Phys. Rev. B*, 76:033401, Jul 2007.

- [83] Jun-Ho Lee, Yun-Ki Choi, Hyun-Jung Kim, Ralph H. Scheicher, and Jun-Hyung Cho. Physisorption of dna nucleobases on h-bn and graphene: vdw-corrected dft calculations. *The Journal of Physical Chemistry C*, 117(26):13435–13441, 2013.
- [84] T. S. Sreeprasad and Vikas Berry. How do the electrical properties of graphene change with its functionalization? *Small*, 9(3):341–350, 2013.
- [85] Robert A Distasio, Vivekanand V Gobre, and Alexandre Tkatchenko. Many-body van der Waals interactions in molecules and condensed matter. *Journal of physics. Condensed matter : an Institute of Physics journal*, 26(21):213202, 2014.
- [86] Mojtaba Bagherzadeh and Anahita Farahbakhsh. Surface functionalization of graphene. *Graphene Materials*, pages 25–65, 2015.
- [87] Zongyu Huang, Guolin Hao, Chaoyu He, Hong Yang, Lin Xue, Xiang Qi, Xiangyang Peng, and Jianxin Zhong. Density functional theory study of Fe adatoms adsorbed monolayer and bilayer MoS₂ sheets. *Journal of Applied Physics*, 114(8), 2013.
- [88] Tapas Kuila, Saswata Bose, Chang Eui Hong, Md Elias Uddin, Partha Khanra, Nam Hoon Kim, and Joong Hee Lee. Preparation of functionalized graphene/linear low density polyethylene composites by a solution mixing method. *Carbon*, 49(3):1033–1037, 2011.
- [89] Jianfeng Shen, Min Shi, Hongwei Ma, Bo Yan, Na Li, Yizhe Hu, and Mingxin Ye. Synthesis of hydrophilic and organophilic chemically modified graphene oxide sheets. *Journal of Colloid and Interface Science*, 352(2):366 – 370, 2010.
- [90] Y Y Sun, Yong-Hyun Kim, Kyuho Lee, and S B Zhang. Accurate and efficient calculation of van der Waals interactions within density functional theory by local atomic potential approach. *The Journal of chemical physics*, 129:154102, 2008.
- [91] L. Q. Xu, W. J. Yang, K.-G. Neoh, E.-T. Kang, and G. D. Fu. Dopamine-Induced Reduction and Functionalization of Graphene Oxide Nanosheets. *Macromolecules*, 43:8336–8339, October 2010.
- [92] Tuan Anh Pham, Nanjundan Ashok Kumar, and Yeon Tae Jeong. Covalent functionalization of graphene oxide with polyglycerol and their use as templates for anchoring magnetic nanoparticles. *Synthetic Metals*, 160(17-18):2028–2036, 9 2010.
- [93] Yongchao Si and Edward T. Samulski. Synthesis of water soluble graphene. *Nano Letters*, 8(6):1679–1682, 2008. PMID: 18498200.

- [94] Ming Fang, Kaigang Wang, Hongbin Lu, Yuliang Yang, and Steven Nutt. Covalent polymer functionalization of graphene nanosheets and mechanical properties of composites. *Journal of Materials Chemistry*, 19(38):7098, 2009.
- [95] Jianfeng Shen, Bo Yan, Min Shi, Hongwei Ma, Na Li, and Mingxin Ye. Synthesis of graphene oxide-based biocomposites through diimide-activated amidation. *Journal of Colloid and Interface Science*, 356(2):543 – 549, 2011.
- [96] Xiujuan Xu, Qingying Luo, Wei Lv, Yongqiang Dong, Yi Lin, Quanhong Yang, Aiguo Shen, Daiwen Pang, Jiming Hu, Jingui Qin, and Zhen Li. Functionalization of graphene sheets by polyacetylene: Convenient synthesis and enhanced emission. *Macromolecular Chemistry and Physics*, 212(8):768–773, 2011.
- [97] Xing Zhong, Jun Jin, Shuwen Li, Zhiyong Niu, Wuquan Hu, Rong Li, and Jiantai Ma. Aryne cycloaddition: highly efficient chemical modification of graphene. *Chem. Commun.*, 46:7340–7342, 2010.
- [98] Sajini Vadukumpully, Jhinuk Gupta, Yongping Zhang, Guo Qin Xu, and Suresh Valiyaveetil. Functionalization of surfactant wrapped graphene nanosheets with alkylazides for enhanced dispersibility. *Nanoscale*, 3(1):303–308, 2011.
- [99] C. Nethravathi and M. Rajamathi. Chemically modified graphene sheets produced by the solvothermal reduction of colloidal dispersions of graphite oxide. *Carbon*, 46(14):1994–1998, 2008.
- [100] Anton Lerf, Heyong He, Michael Forster, and Jacek Klinowski. Structure of Graphite Oxide Revisited. *Journal of Physical Chemistry B*, 102(23):4477–4482, 1998.
- [101] W Gao, L B Alemany, L Ci, and P M Ajayan. New insights into the structure and reduction of graphite oxide . *Nature chemistry*, 1(5):403–408, 2009.
- [102] Zhuang Liu, Joshua T. Robinson, Xiaoming Sun, and Hongjie Dai. Pegylated nanographene oxide for delivery of water-insoluble cancer drugs. *Journal of the American Chemical Society*, 130(33):10876–10877, 2008. PMID: 18661992.
- [103] Sungjin Park and Rodney S. Ruoff. Chemical methods for the production of graphenes. *Nat Nano*, 4(4):217–224, 2009.
- [104] Daniel R. Dreyer, Sungjin Park, Christopher W. Bielawski, and Rodney S. Ruoff. The chemistry of graphene oxide. *Chem. Soc. Rev.*, 39:228–240, 2010.
- [105] Sasha Stankovich, Dmitriy A. Dikin, Richard D. Piner, Kevin A. Kohlhaas, Alfred Kleinhammes, Yuanyuan Jia, Yue Wu, Son Binh T Nguyen, and Rodney S. Ruoff. Synthesis of graphene-based nanosheets via chemical reduction of exfoliated graphite oxide. *Carbon*, 45(7):1558–1565, 2007.

- [106] M. Dion, H. Rydberg, E. Schröder, D. C. Langreth, and B. I. Lundqvist. Van der Waals density functional for general geometries. *Physical Review Letters*, 92(24):246401–1, 2004.
- [107] Valentino R. Cooper. Van der waals density functional: An appropriate exchange functional. *Phys. Rev. B*, 81:161104, Apr 2010.
- [108] Kyuho Lee, Éamonn D. Murray, Lingzhu Kong, Bengt I. Lundqvist, and David C. Langreth. Higher-accuracy van der waals density functional. *Phys. Rev. B*, 82:081101, Aug 2010.
- [109] Judith Harl, Laurids Schimka, and Georg Kresse. Assessing the quality of the random phase approximation for lattice constants and atomization energies of solids. *Phys. Rev. B*, 81:115126, Mar 2010.
- [110] E. Schrödinger. An undulatory theory of the mechanics of atoms and molecules. *Phys. Rev.*, 28:1049–1070, Dec 1926.
- [111] Attila Szabo and Neil S Ostlund. *Modern quantum chemistry : introduction to advanced electronic structure theory*. Mineola, N.Y. : Dover Publications, 1996. Previously published: 1st ed., rev. New York : McGraw-Hill, c1989.
- [112] L. H. Thomas. The calculation of atomic fields. *Mathematical Proceedings of the Cambridge Philosophical Society*, 23(5):542–548, 1927.
- [113] E. Fermi. Un metodo statistice per la determinazione di alcune proprieta dell’atomo. *Rend. Accad. Nazl. Lincei*, 6:602–607, 1927.
- [114] P. Hohenberg and W. Kohn. Inhomogeneous electron gas. *Phys. Rev.*, 136:B864–B871, Nov 1964.
- [115] W. Kohn and L. J. Sham. Self-consistent equations including exchange and correlation effects. *Phys. Rev.*, 140:A1133–A1138, Nov 1965.
- [116] R.M. Martin. *Electronic Structure: Basic Theory and Practical Methods*. Cambridge University Press, 2004.
- [117] Eugen Merzbacher, John Wiley, and Stuart Johnson. *Quantum Mechanics*. John Wiley Sons, Inc., 1970.
- [118] M. Born and R. Oppenheimer. Zur quantentheorie der molekeln. *Annalen der Physik*, 389(20):457–484, 1927.
- [119] J. K. Labanowski and J. W. Andzelm. *Density Functional Methods in Chemistry*. Springer-Verlag, 1991.
- [120] Robert G. Parr, Kenichi Fukui, and Bernard Pullman. *Density Functional Theory of Atoms and Molecules*, pages 5–15. Springer Netherlands, Dordrecht, 1980.

- [121] D. M. Ceperley and B. J. Alder. Ground state of the electron gas by a stochastic method. *Phys. Rev. Lett.*, 45:566–569, Aug 1980.
- [122] Jie Ma and Lin-Wang Wang. Using Wannier functions to improve solid band gap predictions in density functional theory. *Scientific Reports*, 6(1):24924, 2016.
- [123] Srgio Filipe Sousa, Pedro Alexandrino Fernandes, and Maria Joo Ramos. General Performance of Density Functionals General Performance of Density Functionals. *Journal of Physical Chemistry A*, 111:10439–10452, 2007.
- [124] Stefan Grimme. Semiempirical GGA-type density functional constructed with a long-range dispersion correction. *Journal of computational chemistry*, 27(15):1787–1799, 2006.
- [125] Sándor Kristyán and Péter Pulay. Can (semi)local density functional theory account for the london dispersion forces? *Chemical Physics Letters*, 229(3):175 – 180, 1994.
- [126] Mark J. Allen and David J. Tozer. Helium dimer dispersion forces and correlation potentials in density functional theory. *Journal of Chemical Physics*, 117(24):11113–11120, 2002.
- [127] Kevin E. Riley, Michal Pitonak, Petr Jurecka, and Pavel Hobza. Stabilization and structure calculations for noncovalent interactions in extended molecular systems based on wave function and density functional theories. *Chemical Reviews*, 110(9):5023–5063, 2010.
- [128] Alexandre Tkatchenko, Lorenz Romaner, Oliver T. Hofmann, Egbert Zojer, Claudia Ambrosch-Draxl, and Matthias Scheffler. Van der waals interactions between organic adsorbates and at organic/inorganic interfaces. *MRS Bulletin*, 35(6):435–442, 2010.
- [129] Jiří Klimeš and Angelos Michaelides. Perspective: Advances and challenges in treating van der Waals dispersion forces in density functional theory. *Journal of Chemical Physics*, 137(12), 2012.
- [130] Stefan Grimme. Accurate description of van der Waals complexes by density functional theory including empirical corrections. *Journal of Computational Chemistry*, 25(12):1463–1473, 2004.
- [131] John P. Perdew, Adrienn Ruzsinszky, Jianmin Tao, Viktor N. Staroverov, Gustavo E. Scuseria, and Gábor I. Csonka. Prescription for the design and selection of density functional approximations: More constraint satisfaction with fewer fits. *Journal of Chemical Physics*, 123(6), 2005.

- [132] O Anatole Von Lilienfeld, Ivano Tavernelli, Ursula Rothlisberger, and Daniel Sebastiani. Optimization of effective atom centered potentials for london dispersion forces in density functional theory. *Physical review letters*, 93(15):153004, 2004.
- [133] Éamonn D. Murray, Kyuho Lee, and David C. Langreth. Investigation of exchange energy density functional accuracy for interacting molecules. *Journal of Chemical Theory and Computation*, 5(10):2754–2762, 2009. PMID: 26631788.
- [134] Kyuho Lee, Éamonn D. Murray, Lingzhu Kong, Bengt I. Lundqvist, and David C. Langreth. Higher-accuracy van der waals density functional. *Phys. Rev. B*, 82:081101, Aug 2010.
- [135] Oleg A. Vydrov and Troy Van Voorhis. Dispersion interactions from a local polarizability model. *Phys. Rev. A*, 81:062708, Jun 2010.
- [136] D C Langreth, B I Lundqvist, S D Chakarova-Käck, V R Cooper, M Dion, P Hyldgaard, a Kelkkanen, J Kleis, Lingzhu Kong, Shen Li, P G Moses, E Murray, a Puzder, H Rydberg, E Schröder, and T Thonhauser. A density functional for sparse matter. *Journal of physics. Condensed matter : an Institute of Physics journal*, 21(8):084203, 2009.
- [137] Dong Hwa Seo, Hyun You Kim, Ji Hoon Ryu, and Hyuck Mo Lee. Molecular dynamics simulation of the diffusion of au and pt nanoclusters on carbon nanotubes. *The Journal of Physical Chemistry C*, 113(24):10416–10421, 2009.
- [138] James C. Phillips. Energy-Band Interpolation Scheme Based on a Pseudopotential. *Phys. Rev.*, 112:685–695, 1958.
- [139] Marvin L. Cohen and T. K. Bergstresser. Band structures and pseudopotential form factors for fourteen semiconductors of the diamond and zinc-blende structures. *Phys. Rev.*, 141:789–796, Jan 1966.
- [140] M. T. Yin and Marvin L. Cohen. Theory of ab initio pseudopotential calculations. *Phys. Rev. B*, 25:7403–7412, Jun 1982.
- [141] D. R. Hamann, M. Schlüter, and C. Chiang. Norm-conserving pseudopotentials. *Phys. Rev. Lett.*, 43:1494–1497, Nov 1979.
- [142] David Vanderbilt. Soft self-consistent pseudopotentials in a generalized eigenvalue formalism. *Phys. Rev. B*, 41:7892–7895, Apr 1990.
- [143] Paolo Giannozzi, Stefano Baroni, Nicola Bonini, Matteo Calandra, Roberto Car, Carlo Cavazzoni, Davide Ceresoli, Guido L. Chiarotti, Matteo Cococcioni, Ismaila Dabo, Andrea Dal Corso, Stefano De Gironcoli, Stefano Fabris, Guido Fratesi, Ralph Gebauer, Uwe Gerstmann, Christos Gougoussis, Anton Kokalj, Michele Lazzeri, Layla Martin-Samos, Nicola Marzari, Francesco

- Mauri, Riccardo Mazzarello, Stefano Paolini, Alfredo Pasquarello, Lorenzo Paulatto, Carlo Sbraccia, Sandro Scandolo, Gabriele Sclauzero, Ari P. Seitsonen, Alexander Smogunov, Paolo Umari, and Renata M. Wentzcovitch. Quantum espresso: A modular and open-source software project for quantum simulations of materials. *Journal of physics. Condensed matter : an Institute of Physics journal*, 21(39), 2009.
- [144] F. Giustino. *Materials Modelling Using Density Functional Theory: Properties and Predictions*. Oxford University Press, 2014.
- [145] Hendrik J. Monkhorst and James D. Pack. Special points for brillouin-zone integrations. *Phys. Rev. B*, 13:5188–5192, Jun 1976.
- [146] John P. Perdew, Kieron Burke, and Matthias Ernzerhof. Generalized Gradient Approximation Made Simple. *Physical Review Letters*, 77(18):3865–3868, 1996.
- [147] Joachim Paier, Robin Hirschl, Martijn Marsman, and Georg Kresse. The Perdew-Burke-Ernzerhof exchange-correlation functional applied to the G2-1 test set using a plane-wave basis set. *Journal of Chemical Physics*, 122(23), 2005.
- [148] Xiaowei Zhang, Oleg V. Yazyev, Juanjuan Feng, Liming Xie, Chenggang Tao, Yen Chia Chen, Liying Jiao, Zahra Pedramrazi, Alex Zettl, Steven G. Louie, Hongjie Dai, and Michael F. Crommie. Experimentally engineering the edge termination of graphene nanoribbons. *ACS Nano*, 7(1):198–202, 2013.
- [149] Paolo Restuccia and M. C. Righi. Tribochemistry of graphene on iron and its possible role in lubrication of steel. *Carbon*, 106:118–124, 2016.
- [150] Ana S. Dobrota, Igor A. Pašti, Slavko V. Mentus, and Natalia V. Skorodumova. A general view on the reactivity of the oxygen-functionalized graphene basal plane. *Phys. Chem. Chem. Phys.*, 18(9):6580–6586, 2016.
- [151] Bhagawan Sahu, Hongki Min, A. H. MacDonald, and Sanjay K. Banerjee. Energy gaps, magnetism, and electric-field effects in bilayer graphene nanoribbons. *Physical Review B - Condensed Matter and Materials Physics*, 78(4):1–8, 2008.
- [152] Anton Kokalj. Xcrysden—a new program for displaying crystalline structures and electron densities. *Journal of Molecular Graphics and Modelling*, 17(3–4):176 – 179, 1999.
- [153] Jmol: an open-source Java viewer for chemical structures in 3D with features for chemicals, crystals, materials and biomolecules. 2009.
- [154] Koichi Momma and Fujio Izumi. VESTA3 for three-dimensional visualization of crystal, volumetric and morphology data. *Journal of Applied Crystallography*, 44(6):1272–1276, Dec 2011.

- [155] Graeme Henkelman, Andri Arnaldsson, and Hannes Jónsson. A fast and robust algorithm for bader decomposition of charge density. *Computational Materials Science*, 36(3):354 – 360, 2006.
- [156] PerOlov Löwdin. On the nonorthogonality problem connected with the use of atomic wave functions in the theory of molecules and crystals. *The Journal of Chemical Physics*, 18(3):365–375, 1950.
- [157] Johan M. Carlsson and Matthias Scheffler. Structural, electronic, and chemical properties of nanoporous carbon. *Phys. Rev. Lett.*, 96:046806, Feb 2006.
- [158] R. Saito. *Physical Properties of Carbon Nanotubes Hardcover*. World Scientific Publishing Company, 1st edition edition, 1998.
- [159] Ikutaro Hamada and Minoru Otani. Comparative van der waals density-functional study of graphene on metal surfaces. *Phys. Rev. B*, 82:153412, Oct 2010.
- [160] NIST Computational Chemistry Comparison and Benchmark Database. *NIST Standard Reference Database Number 101*. <http://cccbdb.nist.gov/>, release 16a edition, 2013.
- [161] R. Kahn, R. Fourme, D. André, and M. Renaud. Crystal structure of cyclohexane I and II. *Acta Crystallographica Section B*, 29(1):131–138, Jan 1973.
- [162] Wendel S. Paz, Wanderlã L. Scopel, and Jair C.C. Freitas. On the connection between structural distortion and magnetism in graphene with a single vacancy. *Solid State Communications*, 175-176(Complete):71–75, 2013.
- [163] B. R K Nanda, M. Sherafati, Z. S. Popović, and S. Satpathy. Electronic structure of the substitutional vacancy in graphene: Density-functional and green’s function studiesauth. *New Journal of Physics*, 14, 2012.
- [164] Bin Wang and Sokrates T. Pantelides. Magnetic moment of a single vacancy in graphene and semiconducting nanoribbons. *Phys. Rev. B*, 86:165438, Oct 2012.
- [165] Yajun Zhang, MPK Sahoo, and Jie Wang. Strain controlled ferromagnetic–ferrimagnetic transition and vacancy formation energy of defective graphene. *Nanotechnology*, 27(43):435206, 2016.
- [166] A. A. El-Barbary, R. H. Telling, C. P. Ewels, M. I. Heggie, and P. R. Briddon. Structure and energetics of the vacancy in graphite. *Phys. Rev. B*, 68:144107, Oct 2003.
- [167] P. A. Thrower and R. M. Mayer. Point defects and self-diffusion in graphite. *physica status solidi (a)*, 47(1):11–37, 1978.

- [168] S.T. Skowron, I.V. Lebedeva, A.M. Popov, and E. Bichoutskaia. Energetics of atomic scale structure changes in graphene. *Chemical Society Reviews*, 44(10):3143–76, 2015.
- [169] A. V. Krasheninnikov, P. O. Lehtinen, A. S. Foster, and R. M. Nieminen. Bending the rules: Contrasting vacancy energetics and migration in graphite and carbon nanotubes. *Chemical Physics Letters*, 418(1-3):132–136, 2006.
- [170] Gun-Do Lee, C. Z. Wang, Euijoon Yoon, Nong-Moon Hwang, Doh-Yeon Kim, and K. M. Ho. Diffusion, coalescence, and reconstruction of vacancy defects in graphene layers. *Phys. Rev. Lett.*, 95:205501, Nov 2005.
- [171] J. Kotakoski, A.V. Krasheninnikov, and K. Nordlund. Energetics, structure, and long-range interaction of vacancy-type defects in carbon nanotubes: Atomistic simulations. *Physical Review B - Condensed Matter and Materials Physics*, 74(24), 2006. cited By 121.
- [172] R.G. Amorim, A. Fazzio, A. Antonelli, F.D. Novaes, and A.J.R. Da Silva. Divacancies in graphene and carbon nanotubes. *Nano Letters*, 7(8):2459–2462, 2007. cited By 94.
- [173] L. Liu, J. Gao, X. Zhang, T. Yan, and F. Ding. Vacancy inter-layer migration in multi-layered graphene. *Nanoscale*, 6(11):5729–5734, 2014. cited By 7.
- [174] Lili Liu and Shimou Chen. Geometries and Electronic States of Divacancy Defect in Finite-Size Hexagonal Graphene Flakes. *Journal of Chemistry*, 2017, 2017.
- [175] Mohammad T Baei, Masoumeh Moghimi, and Adel Shojaei. Benzene Adsorption on C 24 Fullerene. *Biosciences Biotechnology Research Asia*, 12(August):1363–1366, 2015.
- [176] Silvia Letašiová, Alžbeta Medved'ová, Andrea Šovčíková, Mária Dušinská, Katarína Volkovová, Claudia Mosoiu, and Alena Bartonová. Bladder cancer, a review of the environmental risk factors. *Environmental Health*, 11(1):S11, 2012.
- [177] S. Milham. Most cancer in firefighters is due to radio-frequency radiation exposure not inhaled carcinogens. *Medical Hypotheses*, 73, 2009.
- [178] Yong-Hui Zhang, Ya-Bin Chen, Kai-Ge Zhou, Cai-Hong Liu, Jing Zeng, Hao-Li Zhang, and Yong Peng. Improving gas sensing properties of graphene by introducing dopants and defects: a first-principles study. *Nanotechnology*, 20(18):185504, 2009.
- [179] Dana Krepel and Oded Hod. Lithium Mediated Benzene Adsorption on Graphene and Graphene Nanoribbons. *The Journal of Physical Chemistry C*, page 130820163936007, 2013.

- [180] P. Giannozzi, R. Car, and G. Scoles. Oxygen adsorption on graphite and nanotubes. *The Journal of Chemical Physics*, 118(3):1003–1006, 2003.
- [181] Elizabeth J. Duplock, Matthias Scheffler, and Philip J. D. Lindan. Hallmark of perfect graphene. *Phys. Rev. Lett.*, 92:225502, Jun 2004.
- [182] Tim O. Wehling, Alexander I. Lichtenstein, and Mikhail I. Katsnelson. First-principles studies of water adsorption on graphene: The role of the substrate. *Applied Physics Letters*, 93(20):202110, 2008.
- [183] Jun Ito, Jun Nakamura, and Akiko Natori. Semiconducting nature of the oxygen-adsorbed graphene sheet. *Journal of Applied Physics*, 103(11):113712, 2008.
- [184] Y. H. Lu, W. Chen, Y. P. Feng, and P. M. He. Tuning the electronic structure of graphene by an organic molecule. *The Journal of Physical Chemistry B*, 113(1):2–5, 2009. PMID: 19072320.
- [185] Ashish Chakradhar, Nilushni Sivapragasam, Mindika T. Nayakasinghe, and Uwe Burghaus. Adsorption kinetics of benzene on graphene: An ultrahigh vacuum study. *Journal of Vacuum Science & Technology A: Vacuum, Surfaces, and Films*, 34(2):021402, 2016.
- [186] A. Chakradhar, N. Sivapragasam, M. T. Nayakasinghe, and U. Burghaus. Support effects in the adsorption of water on cvd graphene: an ultra-high vacuum adsorption study. *Chem. Commun.*, 51:11463–11466, 2015.
- [187] A. Chakradhar, K. Trettel, and U. Burghaus. Benzene adsorption on Ru(0001) and graphene/Ru(0001) - How to synthesize epitaxial graphene without STM or LEED? *Chemical Physics Letters*, 590:146–152, 2013.
- [188] Svetla D. Chakarova-Käck, Elsebeth Schröder, Bengt I. Lundqvist, and David C. Langreth. Application of van der Waals density functional to an extended system: Adsorption of benzene and naphthalene on graphite. *Physical Review Letters*, 96(14):1–4, 2006.
- [189] Vagner a. Rigo, Cigdem O. Metin, Quoc P. Nguyen, and Caetano R. Miranda. Hydrocarbon adsorption on carbonate mineral surfaces: A first-principles study with van der Waals interactions. *Journal of Physical Chemistry C*, 116(46):24538–24548, 2012.
- [190] Renju Zacharia, Hendrik Ulbricht, and Tobias Hertel. Interlayer cohesive energy of graphite from thermal desorption of polyaromatic hydrocarbons. *Phys. Rev. B*, 69:155406, Apr 2004.
- [191] Conway Pierce. Localized adsorption on graphite and absolute surface areas. *The Journal of Physical Chemistry*, 73(4):813–817, 1969.

- [192] Sergey M. Kozlov, Francesc Viñes, and Andreas Görling. On the interaction of polycyclic aromatic compounds with graphene. *Carbon*, 50(7):2482–2492, 2012.
- [193] Ali Zain Alzahrani. Structural and electronic properties of graphene upon molecular adsorption: Dft comparative analysis. *Graphene Simulation*, 2011.
- [194] Lingmei Kong, Axel Enders, Talat S Rahman, and Peter a Dowben. Molecular adsorption on graphene. *Journal of physics. Condensed matter : an Institute of Physics journal*, 26(44):443001, 2014.
- [195] Vasile Caciuc, Nicolae Atodiresei, Martin Callsen, Predrag Lazić, and Stefan Blügel. Ab initio and semi-empirical van der Waals study of graphene–boron nitride interaction from a molecular point of view. *Journal of Physics: Condensed Matter*, 24(42):424214, 2012.
- [196] Y. Matsuo, T. Tabata, T. Fukunaga, T. Fukutsuka, and Y. Sugie. Preparation and characterization of silylated graphite oxide. *Carbon*, 43(14):2875 – 2882, 2005.
- [197] Pooja Rani and V. K. Jindal. Designing band gap of graphene by b and n dopant atoms. *RSC Adv.*, 3:802–812, 2013.
- [198] Lara Ferrighi, Mario Italo Trioni, and Cristiana Di Valentin. Boron-doped, nitrogen-doped, and codoped graphene on Cu(111): A DFT + vdW study. *Journal of Physical Chemistry C*, 119(11):6056–6064, 2015.
- [199] Cecilia Mattevi, Hokwon Kim, and Manish Chhowalla. A review of chemical vapour deposition of graphene on copper. *J. Mater. Chem.*, 21(10):3324–3334, 2011.
- [200] E. Mostaani, N. D. Drummond, and V. I. Fal’Ko. Quantum Monte Carlo Calculation of the Binding Energy of Bilayer Graphene. *Physical Review Letters*, 115(11):1–5, 2015.
- [201] Kristian Berland and Per Hyldgaard. Analysis of van der Waals density functional components: Binding and corrugation of benzene and C60 on boron nitride and graphene. *Physical Review B - Condensed Matter and Materials Physics*, 87(20):1–15, 2013.
- [202] K. Gopalakrishnan, A. Govindaraj, and C. N. R. Rao. Extraordinary supercapacitor performance of heavily nitrogenated graphene oxide obtained by microwave synthesis. *J. Mater. Chem. A*, 1:7563–7565, 2013.
- [203] Wei Ding, Zidong Wei, Siguo Chen, Xueqiang Qi, Tao Yang, Jinsong Hu, Dong Wang, Li-Jun Wan, Shahnaz Fatima Alvi, and Li Li. Space-confinement-induced synthesis of pyridinic- and pyrrolic-nitrogen-doped graphene for the

- catalysis of oxygen reduction. *Angewandte Chemie International Edition*, 52(45):11755–11759, 2013.
- [204] Urmimala Maitra, Uttam Gupta, Mrinmoy De, Ranjan Datta, A. Govindaraj, and C. N. R. Rao. Highly effective visible-light-induced h₂ generation by single-layer 1t-mos₂ and a nanocomposite of few-layer 2h-mos₂ with heavily nitrogenated graphene. *Angewandte Chemie International Edition*, 52(49):13057–13061, 2013.
- [205] C.N.R. Rao, K. Gopalakrishnan, and A. Govindaraj. Synthesis, properties and applications of graphene doped with boron, nitrogen and other elements. *Nano Today*, 9(3):324 – 343, 2014.
- [206] Chengzhou Zhu and Shaojun Dong. Recent progress in graphene-based nanomaterials as advanced electrocatalysts towards oxygen reduction reaction. *Nanoscale*, 5:1753–1767, 2013.
- [207] J.-C. Charlier, M. Terrones, M. Baxendale, V. Meunier, T. Zacharia, N. L. Rupesinghe, W. K. Hsu, N. Grobert, H. Terrones, and G. A. J. Amaratunga. Enhanced electron field emission in b-doped carbon nanotubes. *Nano Letters*, 2(11):1191–1195, 2002.
- [208] Lifeng Wang, Frances H. Yang, and Ralph T. Yang. Hydrogen storage properties of b- and n-doped microporous carbon. *AIChE Journal*, 55(7):1823–1833, 2009.
- [209] Da-Wei Wang, Feng Li, Zhi-Gang Chen, Gao Qing Lu, and Hui-Ming Cheng. Synthesis and electrochemical property of boron-doped mesoporous carbon in supercapacitor. *Chemistry of Materials*, 20(22):7195–7200, 2008.
- [210] S. Shiraishi, M. Kibe, T. Yokoyama, H. Kurihara, N. Patel, A. Oya, Y. Kaburagi, and Y. Hishiyama. Electric double layer capacitance of multi-walled carbon nanotubes and b-doping effect. *Applied Physics A*, 82(4):585–591, 2006.
- [211] Madhumita Sahoo, K.P. Sreena, B.P. Vinayan, and S. Ramaprabhu. Green synthesis of boron doped graphene and its application as high performance anode material in li ion battery. *Materials Research Bulletin*, 61:383 – 390, 2015.
- [212] V. Thirumal, A. Pandurangan, R. Jayavel, and R. Ilangovan. Synthesis and characterization of boron doped graphene nanosheets for supercapacitor applications. *Synthetic Metals*, 220:524 – 532, 2016.
- [213] Pablo A. Denis. Band gap opening of monolayer and bilayer graphene doped with aluminium, silicon, phosphorus, and sulfur. *Chemical Physics Letters*, 492(4–6):251 – 257, 2010.

- [214] Ji-Cheng Zhao, Douglas A. Knight, Gilbert M. Brown, Chul Kim, Son-Jong Hwang, Joseph W. Reiter, Robert C. Bowman, Jason A. Zan, and James G. Kulleck. Study of aluminoborane compound alb4h11 for hydrogen storage. *The Journal of Physical Chemistry C*, 113(1):2–11, 2009.
- [215] J. M. García-Lastra. Strong dependence of band-gap opening at the dirac point of graphene upon hydrogen adsorption periodicity. *Phys. Rev. B*, 82:235418, Dec 2010.
- [216] Aurélien Lherbier, X. Blase, Yann-Michel Niquet, Fran çois Triozon, and Stephan Roche. Charge transport in chemically doped 2d graphene. *Phys. Rev. Lett.*, 101:036808, Jul 2008.
- [217] Nabil Al-Aqtash, Khaldoun M. Al-Tarawneh, Tarek Tawalbeh, and Igor Vasiliev. Ab initio study of the interactions between boron and nitrogen dopants in graphene. *Journal of Applied Physics*, 112(3):034304, 2012.
- [218] Hongtao Liu, Yunqi Liu, and Daoben Zhu. Chemical doping of graphene. *J. Mater. Chem.*, 21:3335–3345, 2011.
- [219] M Wu, C Cao, and J Z Jiang. Light non-metallic atom (b, n, o and f)-doped graphene: a first-principles study. *Nanotechnology*, 21(50):505202, 2010.
- [220] X. Deng, Y. Wu, J. Dai, D. Kang, and D. Zhang. Electronic structure tuning and band gap opening of graphene by hole/electron codoping. *Physics Letters A*, 375:3890–3894, October 2011.
- [221] Jiayu Dai, Jianmin Yuan, and Paolo Giannozzi. Gas adsorption on graphene doped with b, n, al, and s: A theoretical study. *Applied Physics Letters*, 95(23):232105, 2009.
- [222] Blanca Biel, X. Blase, Fran çois Triozon, and Stephan Roche. Anomalous doping effects on charge transport in graphene nanoribbons. *Phys. Rev. Lett.*, 102:096803, Mar 2009.
- [223] Humberto Terrones, Ruitao Lv, Mauricio Terrones, and Mildred S Dresselhaus. The role of defects and doping in 2d graphene sheets and 1d nanoribbons. *Reports on Progress in Physics*, 75(6):062501, 2012.
- [224] Mingyang Xing, Wenzhang Fang, Xiaolong Yang, Baozhu Tian, and Jinlong Zhang. Highly-dispersed boron-doped graphene nanoribbons with enhanced conductivity and photocatalysis. *Chem. Commun.*, 50:6637–6640, 2014.
- [225] Zhong-Shuai Wu, Wencai Ren, Li Xu, Feng Li, and Hui-Ming Cheng. Doped graphene sheets as anode materials with superhigh rate and large capacity for lithium ion batteries. *ACS Nano*, 5(7):5463–5471, 2011. PMID: 21696205.

- [226] Shigeki Kawai, Shohei Saito, Shinichiro Osumi, Shigehiro Yamaguchi, Adam S Foster, Peter Spijker, and Ernst Meyer. Atomically controlled substitutional boron-doping of graphene nanoribbons. *Nature communications*, 6:8098, 2015.
- [227] L. S. Panchakarla, a. Govindaraj, and C. N R Rao. Boron- and nitrogen-doped carbon nanotubes and graphene. *Inorganica Chimica Acta*, 363(15):4163–4174, 2010.
- [228] Liuyan Zhao, Mark Levendorf, Scott Goncher, Theanne Schiros, Lucia Pálová, Amir Zabet-Khosousi, Kwang Taeg Rim, Christopher Gutiérrez, Dennis Nordlund, Chernojaye, Mark Hybertsen, David Reichman, George W. Flynn, Jiwoong Park, and Abhay N. Pasupathy. Local atomic and electronic structure of boron chemical doping in monolayer graphene. *Nano Letters*, 13(10):4659–4665, 2013. PMID: 24032458.
- [229] Huan Wang, Yu Zhou, Di Wu, Lei Liao, Shuli Zhao, Hailin Peng, and Zhongfan Liu. Synthesis of boron-doped graphene monolayers using the sole solid feedstock by chemical vapor deposition. *Small*, 9(8):1316–1320, 2013.
- [230] Yong-Bing Tang, Li-Chang Yin, Yang Yang, Xiang-Hui Bo, Yu-Lin Cao, Hong-En Wang, Wen-Jun Zhang, Igor Bello, Shuit-Tong Lee, Hui-Ming Cheng, and Chun-Sing Lee. Tunable band gaps and p-type transport properties of boron-doped graphenes by controllable ion doping using reactive microwave plasma. *ACS Nano*, 6(3):1970–1978, 2012. PMID: 22352710.
- [231] Tianquan Lin, Fuqiang Huang, Jun Liang, and Yingxia Wang. A facile preparation route for boron-doped graphene, and its cdte solar cell application. *Energy Environ. Sci.*, 4:862–865, 2011.
- [232] Ricardo Faccio, Luciana Fernández-Werner, Helena Pardo, Cecilia Goyenola, Oscar N. Ventura, and Ailvaro W. Mombrú. Electronic and structural distortions in graphene induced by carbon vacancies and boron doping. *Journal of Physical Chemistry C*, 114(44):18961–18971, 2010.
- [233] Barbara Albert and Harald Hillebrecht. Boron: Elementary challenge for experimenters and theoreticians. *Angewandte Chemie International Edition*, 48(46):8640–8668, 2009.
- [234] Gleb Parakhonskiy, Natalia Dubrovinskaia, Elena Bykova, Richard Wirth, and Leonid Dubrovinsky. Experimental pressure-temperature phase diagram of boron: resolving the long-standing enigma. *Scientific Reports*, 1(1):96, 2011.
- [235] B. F. Decker and J. S. Kasper. The crystal structure of a simple rhombohedral form of boron. *Acta Crystallographica*, 12(7):503–506, Jul 1959.

- [236] Rahul P Hardikar, Deya Das, Sang Soo Han, Kwang-Ryeol Lee, and Abhishek K Singh. Boron doped defective graphene as a potential anode material for Li-ion batteries. *Physical chemistry chemical physics : PCCP*, 16(31):16502–8, 2014.
- [237] Hiroto Tachikawa. Diffusion dynamics of the li ion on a direct molecular orbital molecular dynamics study. *The Journal of Physical Chemistry C*, 111(35):13087–13091, 2007.
- [238] Kian Ping Loh, Qiaoliang L Bao, Goki Eda, and Manish Chhowalla. Graphene oxide as a chemically tunable platform for optical applications. *Nature Chemistry*, 2(12):1015–1024, 2010.
- [239] G.L. Luque, M.I. Rojas, G.A. Rivas, and E.P.M. Leiva. The origin of the catalysis of hydrogen peroxide reduction by functionalized graphene surfaces: A density functional theory study. *Electrochimica Acta*, 56(1):523 – 530, 2010.
- [240] Z. Maaghoul, F. Fazileh, and J. Kakemam. A DFT study of formaldehyde adsorption on functionalized graphene nanoribbons. *Physica E Low-Dimensional Systems and Nanostructures*, 66:176–180, February 2015.
- [241] N. a. Nebogatikova, I. V. Antonova, V. a. Volodin, and V. Ya Prinz. Functionalization of graphene and few-layer graphene with aqueous solution of hydrofluoric acid. *Physica E: Low-Dimensional Systems and Nanostructures*, 52:106–111, 2013.
- [242] Javad Beheshtian, Ali Ahmadi Peyghan, Zargham Bagheri, and Mohammad Bigdeli Tabar. Density-functional calculations of HCN adsorption on the pristine and Si-doped graphynes. *Structural Chemistry*, 25(1):1–7, 2014.
- [243] Yuriy Hizhnyi, Sergii G. Nedilko, Viktor Borysiuk, and Viktor a. Gubanov. Computational studies of boron- and nitrogen-doped single-walled carbon nanotubes as potential sensor materials of hydrogen halide molecules HX (F, Cl, Br). *International Journal of Quantum Chemistry*, 115(20):1475–1482, 2015.
- [244] Masoud Darvish Ganji, Maryam Mohseni, and Anahita Bakhshandeh. Simple benzene derivatives adsorption on defective single-walled carbon nanotubes: A first-principles van der Waals density functional study. *Journal of Molecular Modeling*, 19(3):1059–1067, 2013.
- [245] Hantarto Widjaja, Zhong-Tao Jiang, Mohammednoor Altarawneh, Chun-Yang Yin, Bee-Min Goh, Nicholas Mondinos, and Bogdan Z. Dlugogorski. Towards a better understanding of the geometrical and orientational aspects of the electronic structure of halogens (F–I) adsorption on graphene. *Applied Surface Science*, 356:370–377, 2015.

- [246] James E. Johns and Mark C. Hersam. Atomic covalent functionalization of graphene. *Accounts of Chemical Research*, 46(1):77–86, 2013. PMID: 23030800.
- [247] Yong-Hui Zhang, Kai-Ge Zhou, Ke-Feng Xie, Jing Zeng, Hao-Li Zhang, and Yong Peng. Tuning the electronic structure and transport properties of graphene by noncovalent functionalization: effects of organic donor, acceptor and metal atoms. *Nanotechnology*, 21(6):065201, 2010.
- [248] Z.M. Ao, J. Yang, S. Li, and Q. Jiang. Enhancement of {CO} detection in al doped graphene. *Chemical Physics Letters*, 461(4–6):276 – 279, 2008.
- [249] O. Leenaerts, B. Partoens, and F. M. Peeters. Adsorption of small molecules on graphene. *Microelectron. J.*, 40(4-5):860–862, April 2009.
- [250] Jishan Wu, Wojciech Pisula, and Klaus Müllen. Graphenes as potential material for electronics. *Chemical Reviews*, 107(3):718–747, 2007. PMID: 17291049.
- [251] Kenneth N. Campbell and Barbara K. Campbell. The addition of hydrogen to multiple carbon-carbon bonds. *Chemical Reviews*, 31(1):77–175, 1942.
- [252] Marta Corno, Albert Rimola, Vera Bolis, and Piero Ugliengo. Study of polycyclic aromatic hydrocarbons adsorbed on graphene using density functional theory with empirical dispersion correction. *Physical chemistry chemical physics : PCCP*, 12(24):6309–6329, 2010.
- [253] Chung Huai Chang, Xiaofeng Fan, Lain Jong Li, and Jer Lai Kuo. Band gap tuning of graphene by adsorption of aromatic molecules. *Journal of Physical Chemistry C*, 116(25):13788–13794, 2012.
- [254] Valentino R. Cooper, T. Thonhauser, and David C. Langreth. An application of the van der waals density functional: Hydrogen bonding and stacking interactions between nucleobases. *The Journal of Chemical Physics*, 128(20):204102, 2008.
- [255] M. J. Frisch, G. W. Trucks, H. B. Schlegel, G. E. Scuseria, M. A. Robb, J. R. Cheeseman, G. Scalmani, V. Barone, G. A. Petersson, H. Nakatsuji, X. Li, M. Caricato, A. V. Marenich, J. Bloino, B. G. Janesko, R. Gomperts, B. Mennucci, H. P. Hratchian, J. V. Ortiz, A. F. Izmaylov, J. L. Sonnenberg, D. Williams-Young, F. Ding, F. Lipparini, F. Egidi, J. Goings, B. Peng, A. Petrone, T. Henderson, D. Ranasinghe, V. G. Zakrzewski, J. Gao, N. Rega, G. Zheng, W. Liang, M. Hada, M. Ehara, K. Toyota, R. Fukuda, J. Hasegawa, M. Ishida, T. Nakajima, Y. Honda, O. Kitao, H. Nakai, T. Vreven, K. Throssell, J. A. Montgomery, Jr., J. E. Peralta, F. Ogliaro, M. J. Bearpark, J. J. Heyd, E. N. Brothers, K. N. Kudin, V. N. Staroverov, T. A. Keith, R. Kobayashi, J. Normand, K. Raghavachari, A. P. Rendell, J. C. Burant, S. S. Iyengar, J. Tomasi,

M. Cossi, J. M. Millam, M. Klene, C. Adamo, R. Cammi, J. W. Ochterski, R. L. Martin, K. Morokuma, O. Farkas, J. B. Foresman, and D. J. Fox. Gaussian~09 Revision A.02, 2016. Gaussian Inc. Wallingford CT 2016.

CURRICULUM VITAE

PERSONAL INFORMATION

Surname, Name: Akay, Tuğçe İrfan

Nationality: Turkish (TC)

Date and Place of Birth: 28.02.1986, Ankara

Phone: +90 312-468 53 00/3526

Fax: +90 312-428 09 33

e-mail: tugce.ersoz@tubitak.gov.tr, tirfanakay@gmail.com

EDUCATION

Degree	Institution	Year of Graduation
Ph.D.	METU, Micro and Nanotechnology Dept.	2017
M.Sc.	METU, Chemical Engineering Dept.	2009
B.S.	METU, Chemical Engineering Dept.	2006
High School	TED Ankara College	2002

PROFESSIONAL EXPERIENCE

Year	Place	Enrollment
May 2011-present	TUBITAK	Scientific Programmes Expert
September 2007-May 2011	TUBITAK	Scientific Programmes Assistant Expert

LANGUAGES

- Turkish - Native Language
- English - Advanced
- German - Basic Level

COMPUTER SKILLS

- Linux
- LaTeX
- Quantum Espresso
- Visualization tools like XCrysDen, Jmol, VMD and Vesta
- Octave
- Mathcad
- Matlab, Simulink
- Cadkey
- Chemcad
- Java
- Microsoft Office (i.e. MS Word, MS Excel, MS PowerPoint)

AWARDS

- Graduate Courses Performance Award, METU, Chemical Engineering Dept., 2008.
- Dean's High Honor Roll, METU, Chemical Engineering Dept., 2005–2006 (Fall and Spring).
- Dean's Honor Roll, METU, Chemical Engineering Dept., 2002–2003 (Fall and Spring), 2003–2004 (Fall and Spring), 2004–2005 (Fall and Spring).

PUBLICATIONS

A. Thesis

Tuğçe İrfan ERSÖZ, MSc. Thesis, Application of Thin Semi Conductor Films Over Glass/Ceramic Surfaces and Their Low Temperature Photocatalytic Activity, METU, Chemical Engineering Department, February 2009.

B. Conference and Meeting Presentations

- Karakaş G., Ersöz T.İ., “Application of Semiconductor Films over Glass Substrates and Their Low Temperature Photocatalytic Activity”, NCC-3, April 28-May 1, 2010, Zonguldak, Turkey (poster presentation).
- Karakaş G., Ersöz T.İ., “Application of Semiconductor Films over Glass Surfaces and Their Photocatalytic Activity”, EMCC-6, March 7-12, 2010, Antalya, Turkey (poster presentation).
- Karakaş G., Ersöz T.İ., “Semi-conductor Metal Oxide Thin Film Glazes For Ceramic Tiles and Glasses with Photocatalytic Self-cleaning Activity”, NCC-2, June 19-21, 2008, Erzurum, Turkey (oral presentation).